HIGH FREQUENCY RADIO WAVE TRANSIONOSPHERIC PROPAGATION POLARIZATION STUDIES FROM THE RRI-SUPERDARN EXPERIMENT

A Thesis Submitted to the

College of Graduate and Postdoctoral Studies

in Partial Fulfillment of the Requirements

for the degree of Master of Science

in the Department of Physics and Engineering Physics

University of Saskatchewan, Saskatoon

By

Fraser Hird

PERMISSION TO USE

In presenting this thesis in partial fulfilment of the requirements for a Postgraduate degree from the University of Saskatchewan, I agree that the Libraries of this University may make it freely available for inspection. I further agree that permission for copying of this thesis in any manner, in whole or in part, for scholarly purposes may be granted by the professor or professors who supervised my thesis work or, in their absence, by the Head of the Department or the Dean of the College in which my thesis work was done. It is understood that any copying or publication or use of this thesis or parts thereof for financial gain shall not be allowed without my written permission. It is also understood that due recognition shall be given to me and to the University of Saskatchewan in any scholarly use which may be made of any material in my thesis.

Requests for permission to copy or to make other use of material in this thesis in whole or part should be addressed to:

Head of the Department of Physics and Engineering Physics
116 Science Place
University of Saskatchewan
Saskatoon, Saskatchewan
Canada
S7N 5E2

Or

Dean

College of Graduate and Postdoctoral Studies

University of Saskatchewan

116 Thorvaldson Building, 110 Science Place

Saskatoon, Saskatchewan S7N 5C9

Canada

Abstract

The enhanced Polar Outflow Probe (ePOP) launched in September 2013 is the fifth Canadian satellite designed for space science observations. One of the 8 instruments it carries is the Radio Receiver Instrument (RRI) which is a passive cross-dipole radio observation instrument. The RRI detects incoming HF (High Frequency) radio waves and measures the polarization information (such as orientation angle and ellipticity angle) of the wave. Radio waves were transmitted from the Saskatoon SuperDARN (Super Dual Auroral Radar Network) radar in conjunction with RRI flybys. There have been 88 conjunctions between RRI and SuperDARN over 4 years (2014-2018). The changing polarization state of the radar signal as it propagates through the ionosphere, transionospheric propagation, is the scientific focus of this thesis. Polarization techniques are used to study and characterize the modifications to the polarization state of the transionospheric radar signal. By characterizing polarization phenomena new details of structure in the ionosphere can be observed and further understanding of HF transionospheric radio wave propagation. Of the 88 RRI-Saskatoon SuperDARN radar conjunctions, 49 flybys recorded usable data including polarization information used to characterize phenomena observed as a radio wave propagates through the ionosphere can be achieved.

Magnetoionic theory of transionospheric radio wave propagation is used in this thesis to predict the phenomena observed in the RRI-Saskatoon SuperDARN radar conjunctions. Phenomena such as the Faraday rotation effect and the Voigt effect are extracted from the theory and demonstrated to occur in the Saskatoon flybys. Features in the orientation angle and ellipticity angle of the Saskatoon flybys are compared and contrasted to previously reported transionospheric observations. The Faraday rotation reversal signatures observed in the auroral region portion of the Saskatoon flybys were found to be more variable than the reversal signatures of sub-auroral events. Danskin et al. (2018) reported considerably more constant observations of the Faraday rotation reversal signatures in RRI flybys in conjunction with an HF transmitter located at Ottawa, Ontario.

The Voigt effect oscillations observed were found to agree with derived magnetoionic theory. They are dependent on the rate of Faraday rotation and are observed throughout an entire RRI flyby. An interpretation of Voigt effect oscillations observations had yet to be reported in transionospheric radio wave propagation experiments before this thesis. Three distinct and consistent spikes in the ellipticity angle were observed in daytime, slewing, high-altitude flybys and such behaviour was not predicted by modelling. It is postulated that the spikes in ellipticity angle demonstrate that RRI is moving between regions of focusing and defocusing of O- and X-mode rays, or “HF fades” during these RRI flybys (James et al., 2006).

Acknowledgements

I would like to thank my supervisor Dr. Glenn Hussey. For the opportunity to begin the research for this thesis. This is a unique and exciting project which I could not have pursued without his guidance every step along the way. He has demonstrated extraordinary patience and care throughout my graduate studies. His invaluable support has lead me to achieve my goals in these studies.

I would like acknowledge Drs. Gareth Perry and Rob Gillies for their work with RRI data handling and modelling. From their experience with the project, they greatly assisted in my understanding of the RRI-SuperDARN experiment and worked in cooperation with me on interpretations. A special thanks to Dr. Gareth Perry for working so closely with me on handling the RRI data and planning RRI-SuperDARN flybys.

Thanks to Drs. Jean-Pierre St.-Maurice, Adam Bourassa, Don Danskin, Sasha Koustov, Kathryn McWilliams and George Sofko for support and advice in my studies. And who all played a part in teaching what I know now and lead me to my understanding of the physics and concepts in this thesis.

Thanks to Andrew Howarth and the rest of the the University of Calgary ePOP team. Thanks to Keith Kotyk, Marci Detwiller and Kevin Krieger and the rest of the SuperDARN Canada group at the University of Saskatchewan. These two teams were integral in planning and executing all of the RRI conjunctions with the Saskatoon SuperDARN radar

I would like to thank the Department of Physics and Engineering Physics and the Institute of Space and Atmospheric Studies for financial assistance in the form of scholarships. I would also like to thank NSERC for funding this research and Dr. Andrew Yau who is the principle investigator for the ePOP satellite. Thanks also goes to the Canadian Space Agency and the European Space Agency for funding the ePOP satellite, the RRI and their continuing operations which allowed this research to take place.

And finally, thank you dearly to my parents and my brother for their love and support for me during my lengthy graduate studies.

CONTENTS

List of Tables

List of Figures

LIST OF ABBREVIATIONS

ACS	Attitude Control System
BPSK	Binary Phase Shift Keyed
CADI	Canadian Advanced Digital Ionosonde
CASSIOPE	CAScade, Smallsat, and IOnospheric Polar Explorer
CHAIN	Canadian High Arctic Ionospheric Network
CPS	Central Plasmasheet
CSA	Canadian Space Agency
CW	Continuous Wave
DTNL	Distant Tail Neutral Line
EM	Electromagnetic
ePOP	enhanced Polar Outflow Probe
ESA	European Space Agency
EUV	Extreme Ultraviolet
FAC	Field-Aligned Current
FAI	Fast Auroral Imager
HF	High Frequency
IMF	Interplanetary Magnetic Field
IRI	International Reference Ionosphere
ISIS	International Satellites for Ionospheric Studies
LEO	Low Earth Orbit
LO	Local Oscillator
LOS	Line Of Sight
QL	Quasi-Longitudinal
QT	Quasi-Transverse
RF	Radio Frequency
RRI	Radio Receiver Instrument
SDR	Software Defined Radio
SNR	Signal to Noise Ratio
STK	Systems Tool Kit
SuperDARN	Super Dual Auroral Radar Network
TEC	Total Electron Content
UT	Universal Time
VHF	Very High Frequency

Chapter 1

Introduction

1.1 Motivation for Research

The RRI-SuperDARN experiment is a unique experiment which focuses on ionospheric research through use of transionospheric radio wave propagation. In this thesis, I make use of the polarization data from the radio receiver (RRI) on the enhanced Polar Outflow Probe (ePOP) to characterize and study large scale structures in the ionosphere.

1.1.1 ePOP, RRI and SuperDARN

The enhanced Polar Outflow Probe (ePOP) is a Canadian satellite mission consisting of a collection of eight scientific instruments on-board the CAScade, Smallsat, and IOnospheric Polar Explorer (CASSIOPE) satellite (Yau et al., 2006). Launched in September 2013 by SpaceX, CASSIOPE is the fifth Canadian satellite designed for space science observations since the beginning of Canada entering into the space-age in the 1960s. My research makes use of the Radio Receiver Instrument (RRI) on-board ePOP to study incoming ground-based radio waves. In the framework of this research, the radio waves are sourced by the Super Dual Auroral Radar Network (SuperDARN) radar (Greenwald et al., 1995) in Saskatoon, Saskatchewan. Details of the experiment instruments are discussed in Chapter 2: Equipment.

1.1.2 Goal of My Research

The goal of my research is to apply polarization techniques to study transionospheric radio wave propagation. This is achieved by combining propagation theory of electromagnetic (EM) waves in a magnetized plasma medium with effects and phenomena observed in the RRI polarization data. The theory of EM wave propagation through the ionosphere begins with understanding of the Appleton-Hartree equation (Budden, 1988). From this equation we can formulate the theoretical understanding of two key polarization phenomena of propagating EM waves, Faraday rotation and the Voigt effect (Zvezdin and Kotov, 1997). These are two phenomena that are routinely observed in RRI flybys and are dependent on the conditions of the ionosphere in which the ground-based radio waves propagate. By studying phenomena, we are able to characterize new details of structure in the ionosphere and further understand transionospheric propagation of EM waves.

An overall goal of ionospheric research is to better understand the ionosphere. Photoionization, particle precipitation and convection in the ionosphere cause variation in the plasma density. In conjunction with propagation theory, the RRI measurements can be used to infer the nature of the ionospheric structures along the radio wave propagation path to the satellite. In addition, there are some studies, such as modelling the gravitational field of the Earth, where the effects of the ionosphere can alter data and should be taken into account.

1.2 Sun/Earth Environment

To begin understanding the structure and composition of the ionosphere of the Earth and its effects on EM waves, knowledge of the solar environment and activity which governs the ionosphere is first required.

1.2.1 Solar Wind

Solar wind is the continual stream of charged particles (or plasma) from the corona of the Sun. The plasma is comprised of hydrogen and helium ions with an equal number of electrons. Near the Earth, the solar wind can vary in velocities and temperatures ranging from: slow solar wind at ~ 400 km/s and $\sim 1.5 * 10^6$ K and fast solar wind at ~ 750 km/s and $\sim 8 * 10^5$ K (Kivelson and Russel, 1995). Considering that it is highly electrically conductive, the solar wind plasma is effectively "frozen-in" to the magnetic field lines of the Sun, known as the interplanetary magnetic field or IMF, as both the plasma and the field lines flow outward from the Sun, passing by every celestial body in the solar system. The IMF and the density of solar wind have substantial effects on the magnetic field of the Earth even though values are typically 6.6 nT and 8.7 protons/cm^3 near Earth (Kelley, 2009).

1.2.2 Magnetic Field of Earth

The magnetic field of the Earth, or geomagnetic field, devoid of the effects of the Sun would be a dipole field with its axis offset $\sim 11^\circ$ from the axis of rotation of the Earth. The magnetic north pole of the dipole is presently located in the southern hemisphere and similarly the magnetic south pole is in the northern hemisphere. The dipole has a magnetic field strength of $\sim 25\ \mu$T near the magnetic equator and $\sim 60\ \mu$T near the poles (Kelley, 2009). This means that, on the surface of the Earth, magnetic field lines would be pointed approximately northward, parallel to the surface of the Earth at the magnetic equator and would be close to vertically downward into the surface at the northern magnetic pole.

However, the IMF and solar wind do have substantial effect on the magnetic field of the Earth. The Earth, located within the solar wind, and the IMF carried with this plasma is analogous to a rock in a stream. The region of space where the background IMF starts interacting with and connecting with the magnetic field of the Earth (the geomagnetic field) is called the magnetosphere. The IMF causes a compression of the magnetic field of the Earth, on the sunward side, and an elongation on the anti-sunward side, creating what is called the magnetotail. The IMF greatly impacts the geomagnetic field especially when the IMF is pointed southward. This is because the southward IMF allows for connection of the magnetic field lines between the IMF and geomagnetic field. The case of a southward IMF is depicted in Figure 1.1 as seen in the noon-midnight plane. In this figure, as the IMF flows from the Sun, the oppositely oriented IMF and geomagnetic field are able to merge together and form the lobe field lines. These lobe lines are "open" and extend outward into the IMF (Kelley, 2009). Field line number 1 (IMF only) flows to the right and merges with the geomagnetic field forming the lobe line number 2 in Figure 1.1. Such lobe lines, which include numbers 3 and 4 in the figure, will continually flow away from the Sun. Newly connected lobe lines on the sunward side of the Earth get dragged anti-sunward until they reconnect at the Distant Tail Neutral Line (DTNL) about 100 $\mathrm{R_E}$ down stream in the magnetotail. These

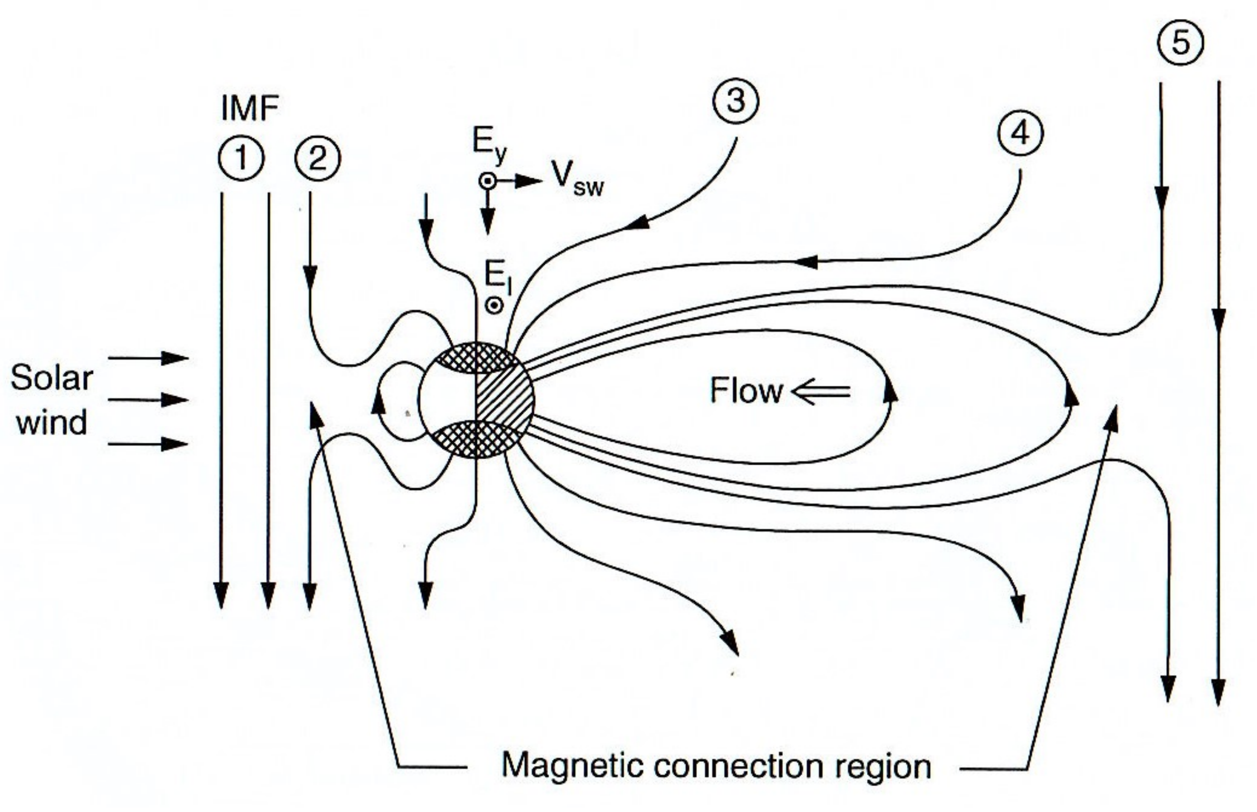

Figure 1.1: Topological diagram of connecting and reconnecting magnetic field lines between the geomagnetic field and the southward IMF as seen from the noon-midnight plane. $\boldsymbol{E}_y$ is the interplanetary electric field, and $\boldsymbol{E}_I$ is the electric field in the ionosphere caused by the magnetic field lines. (Kelley, 2009)

reconnected closed field lines in the magnetotail form the Central Plasmasheet (CPS). These field lines and the associated particles continue to flow back towards the Earth (sunward), depicted by the large "Flow" arrow in the figure, causing substorms and aurora. Eventually those field lines and particles return to the sunward side of the Earth where the process may be repeated. Magnetic field lines are excellent conductors for charged particles, so plasma from the magnetosphere can easily flow into the atmosphere of the Earth from the CPS. In the CPS, voltages are generated that cause Field-Aligned Currents (FACs) which lead to particle precipitation into the ionosphere. The latter often result in aurora. Number 5 in Figure 1.1 is then the magnetic field lines returning to IMF only orientation after the DTNL.

1.3 Upper Atmosphere and Ionosphere

The ionosphere is a region of the atmosphere where there is a significant amount of quasi-neutral plasma (this means that the number of free electrons and free ions in the plasma are approximately equal). The ionization in the atmosphere is caused by photoionization from high energy radiation, predominantly extreme ultraviolet (EUV) radiation from the Sun. These high energy photons are absorbed by the neutral atmosphere species, which will dissociate into ions and electrons attenuating the intensity of the EUV rays more at lower altitudes (Kelley, 2009). Photoionization in the ionosphere is balanced out by the recombination rate, the rate of electrons and ions colliding, becoming neutral again and reducing plasma density. At higher altitudes, the neutral density is lower so the collision frequency and therefore the recombination rate is lower. Whereas, at lower altitudes, the neutral density is much higher so the recombination rate is higher. The balance of photoionization (plasma production) and recombination rate (plasma depletion) varies with altitude in the atmosphere.

The ionosphere is layered into the D-, E- and F-regions. These regions and their plasma densities are depicted in the right half of Figure 1.2 alongside the temperature profile of neutral particles. The neutral atmosphere is divided into the regions of the troposphere, the stratosphere, the mesosphere and the thermosphere (labeled in Figure 1.2). Each region of the ionosphere has slightly different ion composition and particle interactions (Kelley, 2009). The D-region is not significant to this study of the ionosphere, but nonetheless it refers to ionized plasma which is below 90 km. Ionized particles at these low altitudes will not remain ionized for long because there is such a high neutral density that the recombination rate

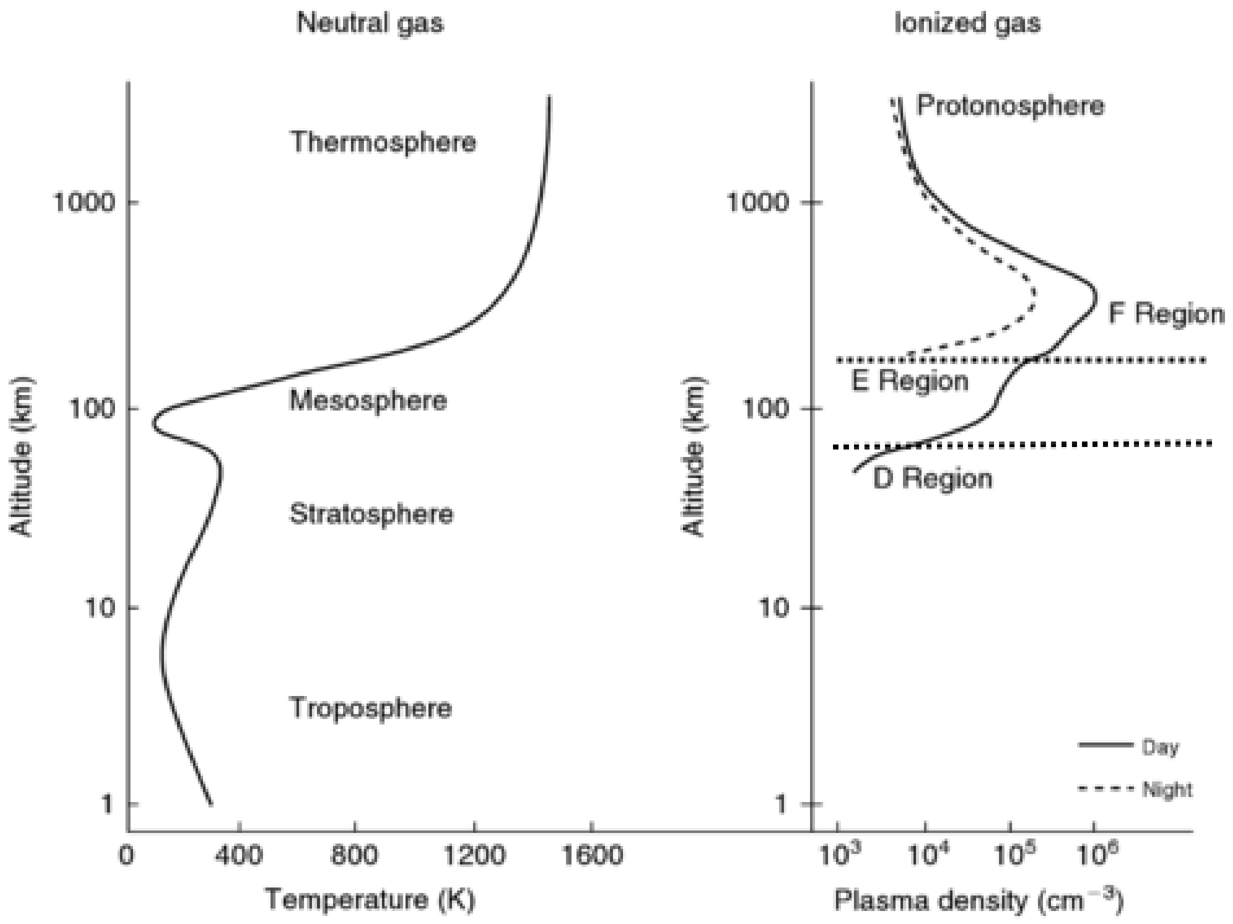

Figure 1.2: Typical profiles of neutral temperature and ionized plasma densities in the upper atmosphere. (Modified from Kelley (2009))

is very high. Plasma density in the D-region is significantly less than at higher altitudes (10^3 cm^{-3}). The collision frequency in the D-region is so high that it does have a unique ion composition as the region is dominated by what are referred to as hydrated protons ($H^+ \cdot (H_2O)_n$).

At higher altitudes, starting at about 90 km and extending to 150 km, is the E-region (Kelley, 2009) which has a plasma density that is a couple orders of magnitude larger than in the D-region. The density of the region is characterized as a combination of the neutral density decreasing and greater incident ionizing radiation. The E-region is dominated by molecular ions, namely NO^+ and ${O_2}^+$ ions, since the atmosphere of the Earth is mostly made of molecular nitrogen and oxygen (Hunsucker and Hargreaves, 2003). The E-region is typically considered to be the first significant layer of the ionosphere and was the first ionospheric region to be discovered. The E-region peak occurs at an altitude of about 100 km (Kelley, 2009) and is caused by a peak in production by ionization of the molecular gases N_2 and O_2 compared to their relative abundances. At higher altitudes, there is not enough N_2 and O_2 present for the ionizing radiation to create these molecular ions.

Relative abundance of each gas species in the upper atmosphere is dictated by its scale height, $H \propto 1/M$, where M is the mass of the species of gas. So, at increasingly higher altitudes, molecular ions are overtaken in relative abundance by monatomic oxygen ions (O^+) (Wayne, 2000). This marks the transition from the E-region to the F-region, which typically is defined at 150 km (Kelley, 2009). The F-region is the largest region of the ionosphere and extends upwards to an altitude of ∼1000 km. Note from Figure 1.2 that a peak in plasma density occurs in the F-region at an altitude of approximately 250 km. This is caused by a balance between O^+ production increasing with altitude and the density of neutral atomic oxygen decreasing with altitude. Plasma which is within 100 km altitude of the F-peak causes most of the observed effects on the polarization state of radio wave signals at the HF (High Frequency) frequencies under consideration in this thesis, since this region has such a high plasma density compared to the rest of the ionosphere (Gillies, 2010).

During nighttime, the Sun, the main source of ionization, is no longer actively producing plasma and therefore the D- and E-regions of the ionosphere become significantly weaker due to recombination. However, the F-region is typically the only significantly remaining region of the ionosphere during nighttime because at this high altitude with its low neutral density the recombination rate is so low that most ionization is able to be sustained throughout the night (Hunsucker and Hargreaves, 2003).

1.4 History of Ground-Based Ionospheric Studies

The ionosonde is one of the first instruments used to observe the ionosphere. An ionosonde is a pulsed radar pointed upwards towards the ionosphere, which sweeps over a range of frequencies. The frequencies these radars sweep are often between 1 to 20 MHz (Hunsucker and Hargreaves, 2003). When a transmitted radar frequency is equal to or less than the plasma frequency (a quantity proportional to the square root of the plasma density) the radar wave is reflected by the plasma medium. So for each radar frequency transmitted from the ionosonde, there is a point where the plasma frequency (increasing with altitude) becomes equal to the radar frequency and the wave is reflected. By measuring the time it takes for the varying frequencies to be reflected back to the radar, a profile of the plasma density over altitude can be calculated. These measurements are called ionograms and give a reliable bottom-side view of plasma density in the ionosphere. In Canada, the Canadian High Arctic Ionospheric Network (CHAIN) operate a collection of ionosondes throughout Canada called the Canadian Advanced Digital Ionosonde (CADI) network (CHAIN, 2019).

The second ground-based ionospheric radar systems critically important in this research, are coherent backscatter radars. The specific coherent backscatter radars used for my thesis research are the Super Dual Auroral Radar Network (SuperDARN) radars (Greenwald et al., 1995). SuperDARN is an international network of pulsed radars located in the mid to high latitudes in both the southern and northern hemispheres. The SuperDARN radar waves propagate into the ionosphere and are at a frequency (8–20 MHZ, but typically in the 9–15 MHz range) such that they propagate into the F-region of the ionosphere while being at a low enough frequency to undergo significant refraction. This beam bending allows for the radar wave propagation direction to reach perpendicularity with the magnetic field of the Earth. When the radar beam is perpendicular to the geomagnetic field, the signal will backscatter off geomagnetic field aligned instabilities (variation in plasma density due to plasma wave instability generation) (Ossakow and Chaturvedi, 1979). Both range and line-of-sight drift velocity of the instabilities can be determined by the time taken for the backscatter to return to the radar and by measuring the Doppler shift in the frequency of the (SuperDARN) backscattered wave. The data of multiple radars recording drift velocities simultaneously can be combined together to create a convection map of the high-latitude ionosphere. In particular, a spherical harmonic expansion model is fit to the measured velocities from all available radars to solve for electrostatic potential in the polar cap (Ruohoniemi and Baker, 1998). The convection map is more accurate with more data points, but the goal of the solution is to create reasonable estimates of voltage potential, even in regions without data coverage. The convection maps created by SuperDARN are used to advance the understanding of the solar-terrestrial environment, including both the ionosphere and magnetosphere. The details of the SuperDARN radars and the use of the SuperDARN radars in my research to study the propagation of HF waves in the ionosphere are detailed in Section 2.3.

1.5 History of Canadian Ionospheric Satellites

Canada has an early history of space exploration, especially regarding ionospheric research. Alouette 1 was launched on September 29, 1962 and marked Canadian entrance into space as the third country to ever have a satellite orbit the Earth (CSA, 2019). Its goal was to gather topside measurements of the ionosphere and its plasma density (like the ionograms from ionosondes), as well as to collect local measurements of the magnetic field of the Earth. Alouette 2 was launched on November 29, 1965 to record similar data. Both satellites remained operational for 10 years, collecting ionospheric data. The success of both satellite missions led to the series of satellites called International Satellites for Ionospheric Studies (ISIS). The first satellite in the series, ISIS I was launched on January 30, 1969 and the second satellite, ISIS II was launched on April 1, 1971 (CSA, 2019). Unlike the Alouette satellites, the ISIS missions had complex navigational equipment and a tape recorder to record experimental data when out of communications range to be later downlinked with ground stations when the satellites came over Canada again. The topside data was one of the data sets used in calculating the International Reference Ionosphere (IRI) model (Bilitza, 2012). What is most relevant to the experiment is that the ISIS satellites were able to receive HF radar transmissions from ground-based radars. Though this was not their primary goal, this ISIS experiment was the precursor for the RRI-SuperDARN experiment to study transionospheric radar signals in the ionosphere.

1.6 Outline of Thesis

Chapter 2 of the thesis covers the equipment used in this experiment including ePOP, RRI and SuperDARN. Parameters and limitations of each are detailed and how they contribute to the process of operating the experiment.

Chapter 3 outlines the magnetoionic theory used in studying the transionospheric waves. Radio wave polarization theory is discussed and how the polarization ellipse of radio wave is measured by RRI. To begin understanding the physics of transionospheric radio wave propagation, we must first define the Appleton-Hartree equation, which describes the effects a magnetized plasma medium has on propagating EM waves. The Appleton-Hartree equation was used to extract two transionospheric phenomena important to this thesis: Faraday rotation and the Voigt effect.

As more RRI-SuperDARN Saskatoon flybys were operated, the parameters of further requested flybys changed to more closely achieve the goals of the research. In Chapter 4, the planning process of RRI-SuperDARN flybys and the parameters most important to my research are discussed. Data format and the process of data analysis are presented. This includes any supplementary tools that were calculated using RRI data, such as ionograms and modelling.

Data analysis was focused on the RRI flybys performed in conjunction with a fixed 14.5 MHz transmission from the SuperDARN Saskatoon radar. In Chapter 5, these flybys are outlined, including all observed polarization phenomena in both the orientation angle and elliptically angle. Polarization phenomena observations in RRI data were compared to magnetoionic theory (discussed in Chapter 3) and prior observations of transionospheric radio wave propagation (reported in the sub-auroral Danskin et al. (2018) and James et al. (2006) papers).

Finally, Chapter 6 summarizes the conclusions from the RRI-SuperDARN Saskatoon flybys. Future work is discussed and suggestions are made for configurations to perform in future RRI-SuperDARN Saskatoon flybys.

CHAPTER 2

EQUIPMENT

The equipment discussed in this chapter constitutes the instruments used in my research. This includes the Radio Receiver Instrument (RRI) on ePOP and SuperDARN. Each instrument is described in detail of primary function and proposed scientific uses. Further information on how each instrument is used to run the experiment, including planning RRI-SuperDARN conjunctions is discussed in Chapter 4.

2.1 ePOP

CASSIOPE is a small satellite with a mass of 500 kg and dimensions of 180 cm by 125 cm. It contains two payloads: ePOP, and Cascade, a commercial communications technology demonstrator. Since ePOP is the scientific payload, the scientific community refers to the satellite as ePOP rather than CASSIOPE. As of early 2019, ePOP has a Low Earth Orbit (LEO) with apogee of about ∼1300 km, perigee of ∼330 km and inclination of 81° (N2YO.com, 2019). The orbit altitudes mean that ePOP is typically within the upper parts of the ionosphere. The high inclination indicates ground tracks that are close to a north-south direction. On board ePOP is also an Attitude Control System (ACS), which plays a significant role in a few of the instruments and will play a particular role in this research.

The ePOP mission is to monitor space storms and polar plasma outflows in the upper atmosphere (Yau et al., 2006). Figure 2.1 is an image of ePOP which labels each of the 8 instruments on board the ePOP instrument suite. This instrument suite includes: the Coherent EM Radio Tomography (CER), a beacon used for ePOP to ground transionospheric measurements; the Fast Auroral Imager (FAI), an optical imager for detailed images of the aurora; the GPS Altitude and Profiling Experiment (GAP), a high precision GPS (Global Positioning System) which measures spacecraft position and attitude; the Imaging and Rapid Scanning Ion Mass Spectrometer (IRM), measuring in situ heavy ions; the Fluxgate Magnetometer (MGF), a magnetometer used to FACs in the polar caps; the Neutral Mass Spectrometer (NMS), measuring in situ neutral gas species; the Radio Receiver Instrument (RRI), which is able to measure polarization information of incoming radio waves; and the Suprathermal Electron Imager (SEI), for measuring low-energy electrons in the atmosphere.

The onboard instrument of interest for this research is the RRI. The RRI is covered in detail in Section 2.2. This thesis is focused on the analysis of RRI observations, particularly the polarization measurement abilities of RRI. Although out of scope of this thesis, the CER and GAP radio instruments on ePOP could supplement and/or complement RRI observations. Since the RRI is only one of 8 instruments on ePOP, challenges in priorities occur when requesting specific experiment parameters, such as attitude and orientation of the spacecraft during a data collection flyby, the variance of which can adversely affect RRI observation usefulness.

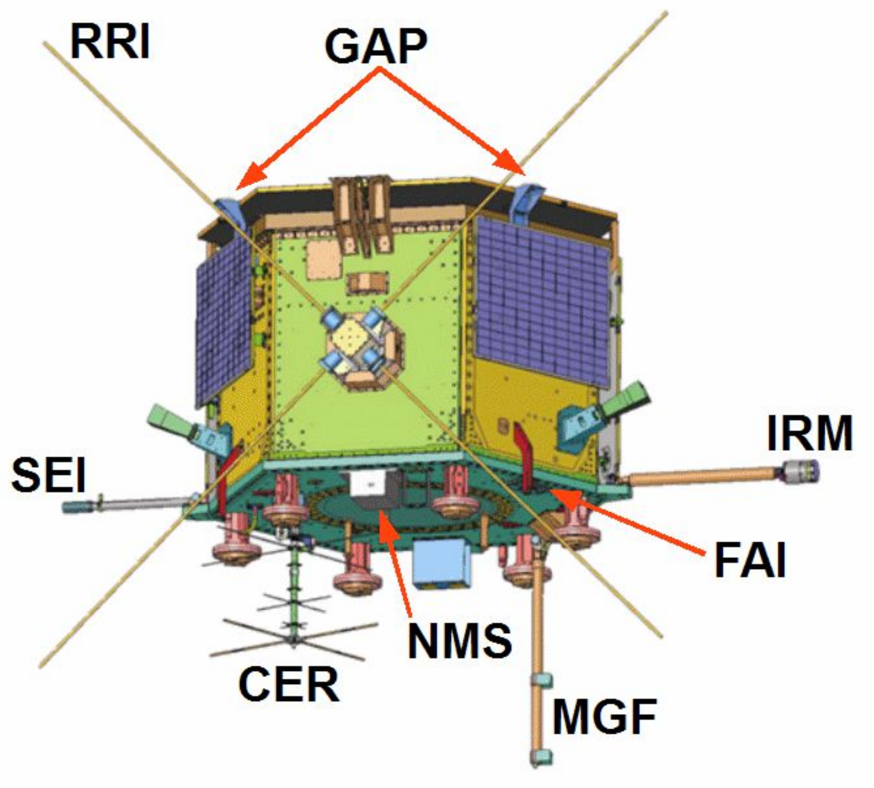

Figure 2.1: A graphical rendition of ePOP with all 8 scientific instruments labeled.

2.2 RRI

The RRI consists of four 3-meter monopoles in an orthogonal dipole configuration for observing the polarization state of incoming radio wave signals in the frequency range from 10 Hz to 18 MHz (James, 2006). The polarization state of an EM wave can be described by a 2-dimensional ellipse in the plane perpendicular to EM wave propagation vector. The plane of the RRI dipoles can most effectively measure a polarization ellipse that is in the same plane (i.e. when the normal direction of the cross dipoles is aligned with the EM wave propagation vector). The RRI was designed with two scientific purposes in mind. One was to measure spontaneous low frequency radio wave emissions from the ionosphere, with the intent to measure wave-particle interactions. This is not the focus of this research. The second

RRI objective was to measure incident high frequency (HF) radio waves from ground-based transmitters such as SuperDARN, to study transionospheric propagation and the structure in the ionosphere. This latter objective is the direct motivation for this research. As will be discussed further in Chapter 3, the interactions between EM waves and a magnetized plasma medium may be described by magnetoionic theory. By measuring the resultant transionospheric radio wave signal from a known ground source, Faraday rotation and the Voigt effect may be observed and then studied through the use of transionospheric theory. The modification of the transionospheric waves can give information on the structure of the ionosphere.

The data collection process of the RRI uses software defined radio (SDR) and direct digitization of the received radio signal. A function block diagram of the RRI channels is presented in Figure 2.2. The voltages of the orthogonal dipoles are directly digitized at a sampling rate of ~ 40 MHz (James, 2006). This signal is mixed in the down converter with a numerical local oscillator (LO) down to a baseband level determined by the incoming ground-based radar signal frequency. The radio signal is formulated into a complex representation of in-phase (I) and quadrature (Q) data. This frequency is then fed into a block labeled as “Low-pass Filter and Decimate”. This block serves two purposes: the first is to reduce unwanted high-frequency data which would cause future aliasing effects, and the second is to downsample (or decimated) the data. Through the downsampling, the data which was sampled at a rate of 40 MHz is reduced to a to a data stream of only 62.5 kHz. This downsampled 62.5 kHz data rate preserves all the information of the measured radar signal. This decimation is required reduce the amount of data that subsequent processes need to handle.

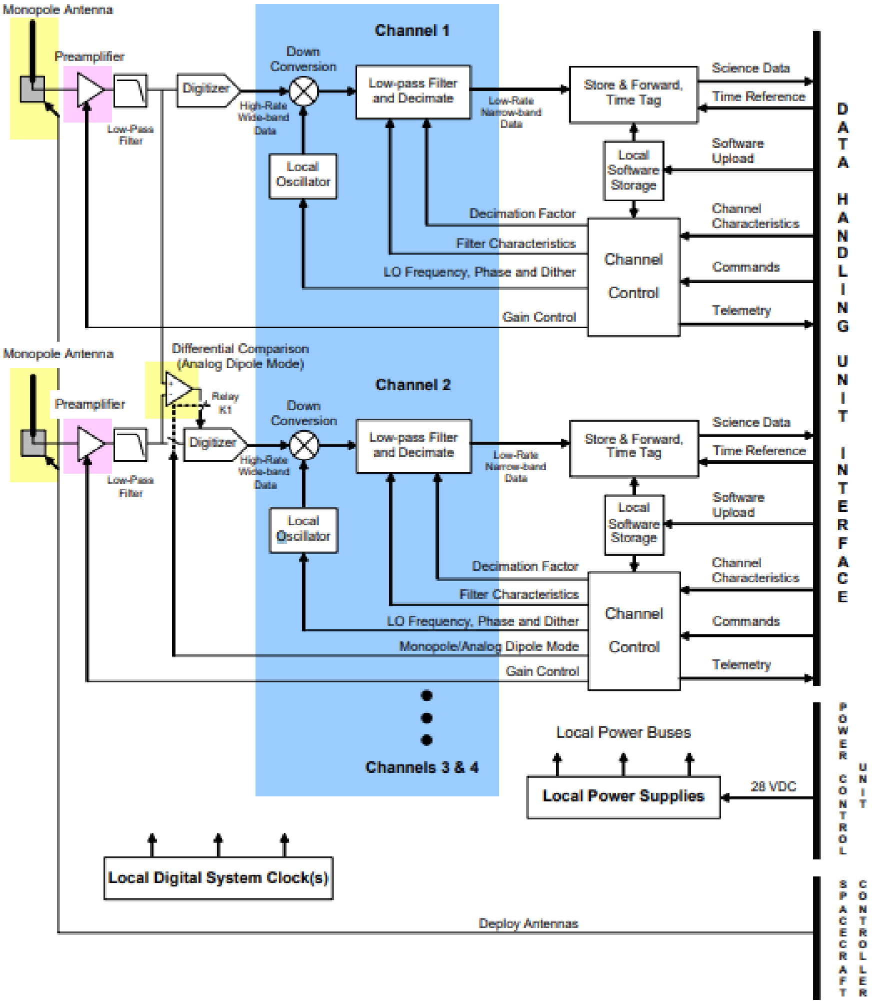

Figure 2.2: Top level function block diagram of two of the four RRI channels. (James, 2006)

RRI experiments performed in the first two and a half years of operation (2013-2015) are presented in Figure 2.3 in a "heat map" format. This presents over 100 RRI flybys, both ascending and descending, most of which are located over the U.S. and Canada. Large concentrations of these flybys are observed over the Saskatoon and Rankin Inlet SuperDARN stations, which are common sources of the ground-based radar signal in the RRI experiments. My research is focused on coordinated operation between the Saskatoon SuperDARN radar and RRI, often with a set radio wave frequency of 11.2 or 14.5 MHz.

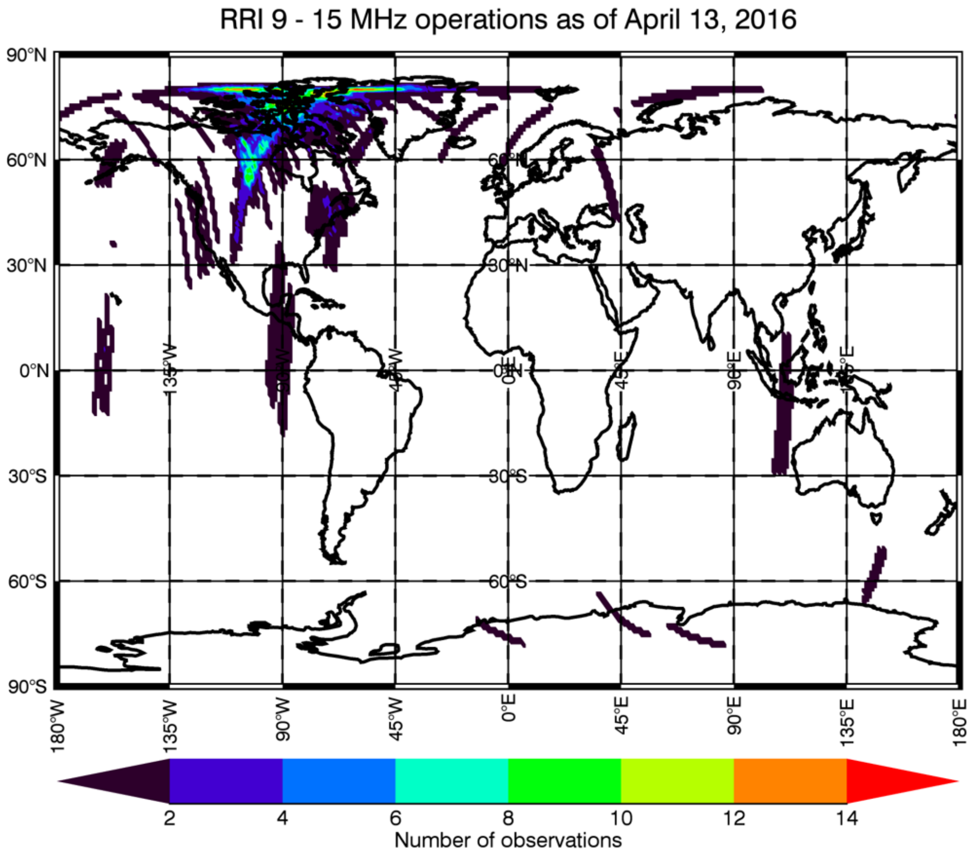

Figure 2.3: ePOP RRI operations performed up to April 13, 2016 at set frequencies between 9-15 MHz [Courtesy: Gareth Perry].

The RRI is, for the purposes of this research, measuring transionospheric polarization information from a ground-sourced radar. A polarization ellipse of an EM wave is a 2-dimensional quantity in space (see Section 3.1 for more details), aligned perpendicular to the propagation direction of the EM wave. Since the RRI is also a 2-dimensional measuring apparatus, this means that if we wanted to exactly measure the incoming EM polarization information, we would attempt to keep the plane of the RRI antennas aligned with the plane of the polarization ellipse. This is referred to as a slewing mode of operation, where the RRI normal direction is pointed parallel (or anti-parallel) to the EM wave propagation direction over the course of the full flyby. Any amount of misalignment can reduce how accurate and therefore usable RRI measurements are. However, in practice this will never remain perfectly aligned for a few reasons. Firstly, there will always be some amount of relatively unpredictable raypath bending of the EM wave as it passes through the ionosphere (up to $\sim 10^\circ$ but usually much less (Gillies, 2010)). And secondly, even though ePOP has sufficient attitude control to keep RRI pointed at SuperDARN Saskatoon over the course of a flyby, sometimes other instruments on board ePOP require their own particular attitude control which will point RRI in a non-ideal direction. A mode referred to as a "nadir flyby" is when another instrument on ePOP is point towards the Earth, which consequentially points the RRI normal direction along the ram direction (the direction of the motion of the satellite). In this orientation, polarization information is lost close to the Saskatoon SuperDARN radar, but we find that science can still be done in the more northward parts of these flybys.

2.3 SuperDARN

SuperDARN is a pulsed radar system made up of a ground-based network of 35 HF radars in the mid-latitude, auroral and polar zones of both the northern and southern hemispheres. SuperDARN transmits a linearly polarized HF radio wave that is oriented horizontally or parallel to the ground. Its pulse length is 300 μs with 7 or 8 pulse sequences every 100 ms at a transmitted power of 10 kW (Greenwald et al., 1995). Different pulse schemes are possible, but schemes of 7 or 8 pulse sequences were used for this research. SuperDARN, in its primary operation, uses pulsed HF radar signals and beamforming to observe the ionosphere in a wide field of view (switching between multiple beam directions). Returned backscatter radar waves are from field aligned F-region irregularities (shown in Figure 2.4

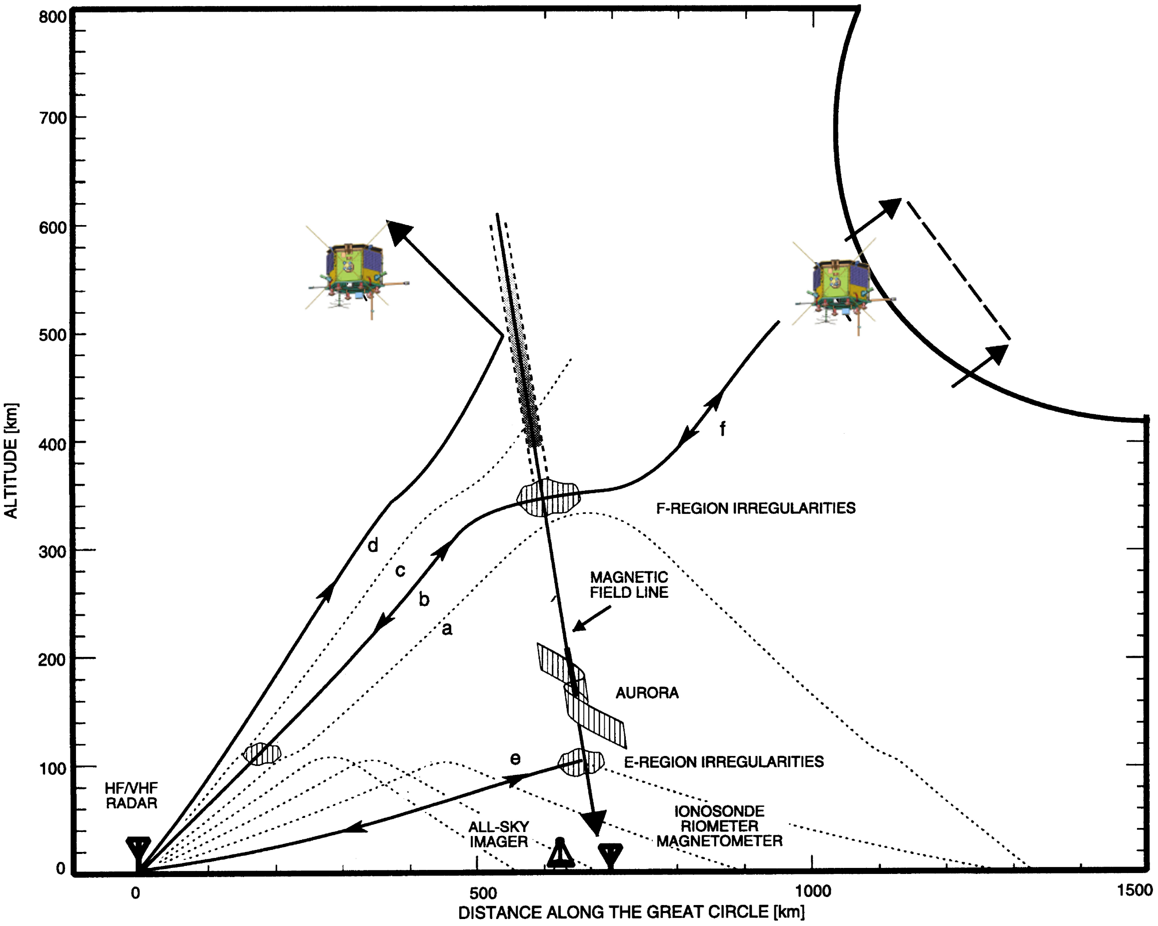

Figure 2.4: Depiction of coordinated measurements between ePOP and SuperDARN (Yau et al., 2006). Raypaths "a" through "d" are raypaths that propagate through the E-region and interact with the F-region. Raypaths "b" through "d" are raypaths that further propagate through the F-region and are record by RRI. Raypath "e" and surrounding similarly shaped lower angle raypaths do not propagate through the E-region and instead get reflected back towards the Earth.

along raypaths "a" through "d") from the ionosphere at different ranges and Doppler shifts caused by the plasma motions in the F-region. One of the many SuperDARN data products is to combine these measurements from the network of SuperDARN radars to produce electric field contour plots (voltage potential plots) of the ionosphere covering the polar cap and high latitude regimes (Virgina Tech SuperDARN, 2019).

Figure 2.4 depicts many other potential raypaths. Such as low angle raypath "e" and surrounding similarly shaped raypaths in dotted lines, which depict E-region echos that can occur more prominently in very high frequency (VHF) radars. However, for the RRI-SuperDARN experiment the raypaths of "b", "c" and "d" in Figure 2.4 are the focus. Unlike raypath "a" which reflects back to the Earth, these radar waves pass through both the E-region and the F-region thus becoming the transionospheric waves that are recorded by RRI. Raypath "d" is a postulated raypath that reflects backwards on the other side of the F-region. This raypath is not yet shown to occur in RRI results and is not considered in this thesis. Raypath "c" is a transionospheric signal that does not get observed by RRI, while raypath "b" does get measured by RRI along the line "f" (the incoming EM wave propagation vector).

The pulsed nature of SuperDARN means there are significant sections of RRI data where there is no radio wave being sourced. This effect is accounted for in the data analysis. For the ePOP-RRI flybys over the Saskatoon SuperDARN radar (52.2°N, 106.5°W), two different pulse code sequences are interlaced to provide a marker for timing; although, this timing aspect is not needed directly for this study. A great benefit this experiment gains from using a SuperDARN radar is its large power output of 10 kW. With this high power output, it does not matter if ePOP is precisely within the boresight of the currently active SuperDARN beam because the side lobes of the radar radiation pattern are still significantly intense for RRI detection. This effective wide radiation pattern from SuperDARN and a 23.1° boresight heading (North-Eastern pointing) of Saskatoon SuperDARN radar means that virtually any ePOP flyby over northern Saskatchewan and its surrounding area will obtain RRI measurements (Yau et al., 2006).

While SuperDARN measurements make use of the backscattered radio waves, the RRI experiment focuses on the reception of the “forward scattered” radio waves as they propagate through the ionosphere (for transionospheric propagation studies).

Chapter 3

Magnetoionic Theory

My research is an experimental observational study of propagating electomagnetic (EM) waves through the ionosphere, and requires using the theory that describes the physics to interpret the results. Magnetoionic theory describes how the polarization state of an EM wave is affected by a magnetized plasma medium, such as the ionosphere. This chapter will present and discuss general polarization theory, along with magnetoionic theory, and particularly, the important phenomena that are described by magnetoionic theory, especially Faraday rotation and the Voigt effect.

3.1 General Polarization Theory

One of the unique characteristics of the RRI is that it was designed to observe the polarization information of incoming radio waves. For the wave propagation direction in the z-direction, the polarization state of an EM wave can be described as a general ellipse in the xy-plane (the plane perpendicular to the propagation direction) (Budden, 1988), as seen in Figure 3.1. The polarization ellipse is the shape that is traced by the wave electric field vector endpoint in the xy-plane, with respect to time. Having polarization state information available provides three important variables for consideration when monitoring RRI mea-

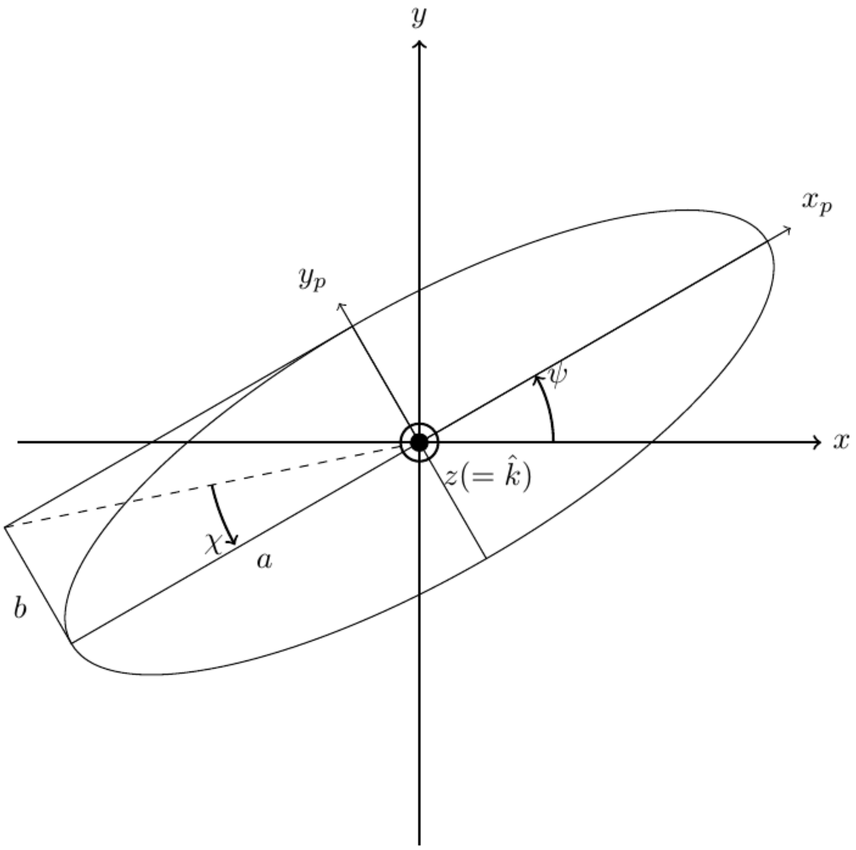

Figure 3.1: General elliptical polarization of radio waves as the radio wave propagation direction, $\hat{k}$ points out of the page (parallel to the z-axis).

surements: the orientation angle ψ, and the semi-major (a) and semi-minor (b) axes of the polarization ellipse. The orientation angle is defined as the angle between the x-axis and the semi-major axis of the ellipse. The ellipticity angle is the angle created by the semi-major and semi-minor axes of the polarization ellipse, namely:

$$\chi = \pm \arctan\left(\frac{b}{a}\right), \tag{3.1}$$

where a and b are the semi-major and semi-minor axes of the polarization ellipse respectively. In the case of RRI measurements, the orientation angle ψ and the ellipticity angle χ can be solved using the dipole voltages (Hecht and Zajac, 1974),

$$\sin 2\chi = \frac{2V_x V_y \sin\epsilon}{{V_x}^2 + {V_y}^2}, \tag{3.2}$$

$$\tan 2\psi = \frac{2V_x V_y \cos\epsilon}{{V_x}^2 - {V_y}^2}, \tag{3.3}$$

where ϵ is the phase difference between the dipoles (calculated by taking the difference in complex phase angle from I/Q data) and, V_x and V_y are the voltage magnitude along each dipole. In order to fully describe the polarization ellipse, the orientation angle must range from 0° to 180°, and the ellipticity angle from −45° to +45°. The ellipticity angle of an ideally circularly polarized wave is either $\chi = +45°$ (right hand circular) or $\chi = -45°$ (left hand circular), while the orientation angle ψ in this idealized case has no meaning and is therefore undefined. Alternatively, the ellipticity angle χ of a linearly polarized wave is ideally $\chi = 0°$ such that the orientation angle (from 0° to 180°) fully describes the polarization state.

In practice, the interpretation of the polarization information will always need to take into account the orientation of RRI in this experiment. The cross-dipole configuration of RRI means that the polarization ellipse is most accurately measured when the incident EM wave is exactly along the cross-dipole normal direction (the direction which is perpendicular to both orthogonal dipoles). As will be shown in Section 3.2, HF radio waves propagating through the ionosphere at a radar frequency slightly larger than the plasma frequency are subject to refraction, or raypath bending. The amount of refraction is dependent on the exact ratio between the radar frequency and the local plasma frequency. Raypath bending alters the radio wave propagation angle from some initial line-of-sight (LOS) direction between the radar and ePOP. Since the amount of bending is dependent on the exact ionospheric conditions at the time of experiment, it is in practice impossible to ensure perfect alignment of the RRI normal direction and incident radio wave propagation direction for the entirety of the ePOP flyby. Raypath bending will typically only alter the angle of incidence by $\sim 5°$ (at most up to ∼ 10°) (Gillies, 2010), which is an amount that will only create a small amount of systematic experimental error (further discussed in Section 4.3). This concern has also been significantly reduced as relatively high radio frequencies (14.5 MHz) were used for the analysis, and they exhibit even less bending.

3.2 Appleton-Hartree Equation

The goal of this research is the study of transionospheric propagation of radio waves through the use of polarization techniques. Understanding the polarization techniques begins with understanding how a transionospheric EM wave interacts with the ionosphere. The Appleton-Hartree equation describes how an EM wave interacts with a magnetized plasma, such as in the ionosphere. Derivation of the Appleton-Hartree equations starts with Maxwell's equations and the Langevin equations (Tanenbaum, 1967) to develop

$$\nabla \times (\nabla \times \boldsymbol{E}) - \frac{\omega_r^2}{c^2}\boldsymbol{E} = -i\omega_r \mu_0 N_e e \boldsymbol{u} \tag{3.4}$$

and

$$\boldsymbol{u}\left(\omega_r^2 + i\omega_r \nu\right) = -\frac{ie\omega_r}{m_e}\left(\boldsymbol{E} + \boldsymbol{u} \times \boldsymbol{B}\right), \tag{3.5}$$

where $\boldsymbol{E}$ is the electric field vector, $\omega_r = 2\pi f$ is the EM wave frequency (rad/s), N_e is the electron density in the plasma, $\boldsymbol{u}$ is a vector of the average particle velocity, $\boldsymbol{B}$ is the external magnetic field, and ν is the momentum transfer collision frequency (Tanenbaum, 1967). In the F-region of the ionosphere, ν is significantly small enough that $\omega_r^2 >> i\omega_r\nu$, which means the expression $\omega_r^2 + i\omega_r\nu$ is simplified to ω_r^2. Since the polarization state of a transionospheric HF radio wave is mostly impacted by the F-region (Gillies, 2010), then EM wave absorption from collisions is not considered for this thesis as all observations are during relatively undisturbed ionospheric conditions. The constants used are the speed of light c, the vacuum permeability μ_0, the elementary charge e, and the mass of an electron m_e.

These equations (Equations 3.4 and 3.5) are then combined algebraically and separated into Cartesian coordinate directions. Standard practice is to assume that the z-direction is the wave propagation direction $\hat{k}$ as shown in Figure 3.1 and $\boldsymbol{B}$ lies in the xz-plane with an angle θ from the wave propagation direction. Thus, the following matrix equation is formed involving the plasma frequency ω_p, the cyclotron frequency ω_c, the wave number (or k-vector) $k = \boldsymbol{k}/\hat{k}$, and the index of refraction n,

$$\boldsymbol{A}\boldsymbol{u} = 0, \tag{3.6}$$

$$\boldsymbol{A} = \begin{bmatrix} 0 & 1-\Phi & iY_L \\ iY_T & -iY_L & 1-\Phi \\ 1-X & 0 & -iY_T \end{bmatrix}, \tag{3.7}$$

$$\omega_p^2 = \frac{N_e e^2}{m\epsilon_0}, \quad \omega_c = \frac{eB}{m}, \quad n^2 = \frac{k^2c^2}{\omega_r^2}, \quad X = \frac{\omega_p^2}{\omega_r^2},$$
$$Y_T = \frac{\omega_c}{\omega_r}\sin\theta, \quad Y_L = \frac{\omega_c}{\omega_r}\cos\theta, \quad \Phi = \frac{X}{1-n^2}. \tag{3.8}$$

Since $\boldsymbol{u} = 0$ is a trivial solution to Equation 3.6, it must be that $\det(\boldsymbol{A}) = 0$ instead. Setting the determinant of $\boldsymbol{A}$ to be zero gives a quadratic equation in Φ, which can be related to the index of refraction as $n^2 = 1 - X/\Phi$ (Equation 3.8). This then gives the dispersion relation

$$n^2 = 1 - \frac{X}{1 - \frac{{Y_T}^2}{2(1-X)} \pm \sqrt{\frac{{Y_T}^4}{4(1-X)^2} + {Y_L}^2}}. \tag{3.9}$$

Since there is a plus-minus sign in Equation 3.9, an incident EM wave can have two independent or orthogonal modes of propagation. These propagation modes are referred to as the ordinary mode or "O-mode" (plus sign) and the extraordinary mode or "X-mode" (minus sign). Each mode has a different index of refraction and different polarization (discussed further in Section 3.3). Figure 3.2 provides a depiction of how the indices of refraction change, for both O- and X-modes, as the electron density changes. The O- and X-modes also experience different amounts of EM wave absorption by the plasma (X-mode propagation experiences greater absorption than O-mode). However, these are have been shown that little absorption occurs in quiet ionospheric conditions (Gillies, 2010). And all of the flybys from the RRI-SuperDARN experiment presented in this thesis are from relatively quiet ionospheric conditions. Also shown in Figure 3.2 are the points of reflection and resonance at $n = 0$ and $n \to \pm\infty$ respectively. These occur when the radio wave frequency is comparable and almost equal to the plasma frequency, which is presented in Figure 3.2 when $X = \frac{\omega_p^2}{\omega_r^2} \approx 1$.

The Appleton-Hartree equation gives a complete 3D representation of how a radio wave interacts with a medium of magnetized plasma it is traveling through it. For various radio frequencies, properties of the Appleton-Hartree equation can have substantial effects on the radar signal (for example, around $X = 1$ as shown in Figure 3.2). The transionospheric waves measured by the RRI have a constant radio wave frequency which, for this experiment, is chosen to be greater than the peak plasma frequency which is typically around 10 MHz. There have been two radar frequencies used in RRI-SuperDARN flybys, which are 14.5 MHz ($X = 0.476$ when plasma frequency is 10 MHz) and 11.2 MHz ($X = 0.797$ when plasma frequency is 10 MHz). When using a radar frequency of 14.5 MHz, behaviour is described

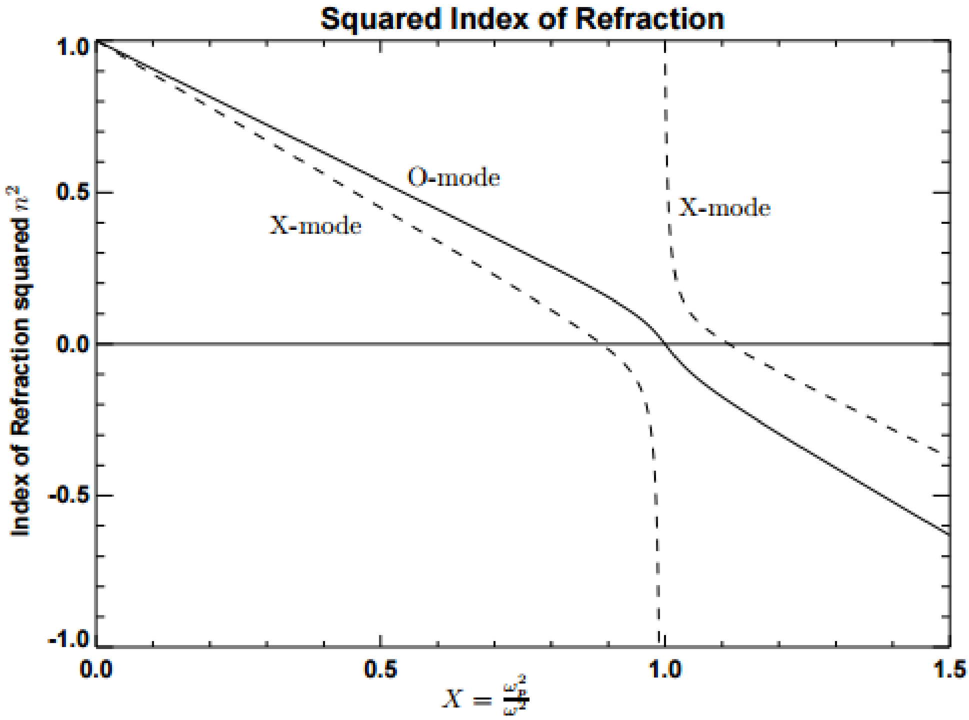

Figure 3.2: The squared index of refraction, n^2, for both O- and X-modes as a function of $X - \omega_p^2/\omega_r^2$. This is calculated using constant aspect angle ($\theta = 40°$), magnetic field strength ($B = 0.60$ G), radio wave frequency ($f_r = 15.0$ MHz). (Gillies, 2010)

by the upper-left portion of Figure 3.2. However, using 11.2 MHz was evidently too low of a frequency and produced inconsistent RRI measurements. This was most probably caused by large amounts of beam bending or absorption in the ionosphere even though there were still no points of reflection or resonance along the path of the transionospheric signal.

3.3 QL and QT Approximation

In an effort to gain physical understanding of the Appleton-Hartree equation, traditionally the equation is simplified into two different propagation conditions in the ionosphere (Budden, 1988). These two propagation conditions are divided by whether the given EM wave is propagating along the external magnetic field (B-field) or perpendicular to it. In these two extreme conditions, the orthogonal O- and X-modes of propagation have very particular propagation characteristics. For an EM wave that is propagating longitudinally anti-parallel to the B-field, two polarization states are allowed to propagate: right-hand-circular and left-hand-circular, which are the O- and X-modes of propagation respectively. A measured EM wave along the B-field at any point will be the sum of these two circularly polarized propagation modes at that point, and therefore any polarization state is able to propagate. Similarly, an EM wave that is propagating perpendicular (transverse) to the B-field will be separated into two orthogonal linear polarization states: a linear polarization state along the B-field, the O-mode, and linear polarization state perpendicular to the B-field, the X-mode. Again, at any point along the transverse propagating EM wave in the ionosphere, the measured EM wave polarization is the sum of these two linear polarization states.

The above description is for O- and X-modes of EM waves that are either propagating exactly along the B-field or exactly perpendicular to the B-field. In practice, the EM wave propagation direction in the RRI-SuperDARN experiment are never perfectly longitudinal or transverse to the B-field. However, it is typical to refer to these regimes of propagation even when not perfectly aligned. These would be the quasi-longitudinal (QL) and quasi-transverse (QT) approximation regimes. The QL and QT approximations categorize the angle of a propagating EM wave with respect to the B-field, the aspect angle θ, to either the exactly longitudinal case, $\theta = 0°$, or exactly transverse case, $\theta = 90°$. The QL approximation applies when

$$ {Y_L}^2 > \frac{{Y_T}^4}{4\left(1 - X\right)^2}. $$

With this approximation, Equation 3.9 can be simplified to

$$ {n_{QL}}^2 = 1 - \frac{X}{1 \pm |Y_L|}, \tag{3.10} $$

where n_{QL} is the index of refraction in the QL regime, and the O- and X-modes are attributed to the plus and minus signs respectively in these equations. Likewise, the QT approximation applies when

$$ {Y_L}^2 < \frac{{Y_T}^4}{4\left(1 - X\right)^2}. $$

And similarly, Equation 3.9 simplifies to, after (Hussey, 1994),

$$ {n_{QT}}^2 = \begin{cases} 1 - \frac{X}{1+(1-X)\cot^2\theta} & \text{(plus sign, “O-Mode”)} \\ 1 - \frac{X}{1-{Y_T}^2/(1-X)} & \text{(minus sign, “X-Mode”)}, \end{cases} \tag{3.11} $$

where n_{QT} is the index of refraction in the QT regime. It has been traditionally postulated that for a typical HF radio wave frequency ($\sim$ 15 MHz), the QL approximation remains valid for an aspect angle up to approximately 60° off parallel, ($\theta \leq 60°$) (Gillies, 2006). Whereas, the QT approximation remains valid for up to a few degrees off perpendicularity. However, it has been concluded from previous RRI results (and will be shown in Chapter 5) that both QL and QT effects are observed throughout an entire RRI flyby regardless of which regime the EM wave propagation is in at the time. The QL and QT approximation are used primary for interpretation and understanding purposes since they can be used to simplify the Appleton-Hartree equation.

When measuring the polarization state of transionospheric radar signal, the typical QL regime phenomenon observed is the Faraday rotation effect, and for the QT regime the Voigt effect. Both of these phenomena are described in the following two subsections. Again, these phenomena are attributed to the QL and QT approximations respectively, but both effects are observed, simultaneously, throughout any aspect angle, $0° < \theta < 90°$, rather than only within the range of aspect angles valid for each approximation regime. Faraday rotation and the Voigt effect will be simplified to their most extreme conditions, when the EM wave propagation is respectively anti-parallel or perpendicular to external magnetic field.

3.3.1 Faraday Rotation

Faraday rotation is the QL regime process in which the linear portion of a polarization state of an EM wave rotates as the wave propagates through a plasma medium. As shown above, for a radio wave propagating exactly anti-parallel to the external magnetic field, two orthogonal polarization states are allowed to propagate: right-hand circular and left-hand circular polarization, the O- and X-modes respectively. The linearly polarized radio wave sourced from a SuperDARN radar will then split into two equal but oppositely-handed circularly polarized waves (Stix, 1992). As can be assessed by inspecting Equation 3.10, the different modes of propagation have small differences in refractive indices in the ionosphere (see also the top-left of Figure 3.2).

Since the O-mode will have a slightly smaller wavelength than the X-mode, it will gradually gain phase with respect to the X-mode and the combined linear wave will appear to rotate in the right-handed sense. Nominally, Faraday rotation is half of the phase difference between the O- and X-modes (Hussey, 1994) and in the exactly longitudinal case may be written as

$$\phi_F = \frac{\delta_O - \delta_X}{2} = \frac{1}{2}\int (k_O - k_X)\, d\ell, \tag{3.12}$$

where the subscripts "O" and "X" refer to O- and X-mode propagation respectively and ϕ_F is the total resultant Faraday rotation observed at any one given point. The absolute value of the Faraday rotation is not directly measured by RRI, but the relative value or the rate of the change of Faraday rotation over the course of a flyby is observed. Using substitutions from the expressions given in Equation 3.8, the Faraday rotation in the QL regime can then be related to the magnetic field B, the aspect angle θ, and the electron density N_e, through the expression

$$\phi_F = \frac{e^3 \mu_0 c}{2{m_e}^2 \omega^2} \int B \cos\theta N_e d\ell, \tag{3.13}$$

where the integral is calculated along the raypath. Faraday rotation caused by the magnetized plasma medium is a measurement of the integrated electron density along the propagation path. However, the aspect angle θ will change along the wave path as the magnetic field lines of the Earth are not straight, nor is the raypath straight since it is affected by the geometry of the raypath with respect to local B and the changing location of the satellite during a pass (Gillies, 2006). As this equation will be used extensively to contextualize RRI data, it is important to note that there are effectively two groupings of terms with the integral of Equation 3.13. There is the set of terms that relate to the geometric shape of the magnetic field of the Earth at a given point, $B \cos\theta$, and a set of terms that relate to the total electron content (TEC) along the radar signal raypath, $N_e d\ell$.

The Faraday rotation effect measured by RRI was shown by Danskin et al. (2018) using a high-frequency CW (continuous wave) transmitter located in Ottawa as the radio source. Unique phenomena with Faraday rotation were observed at this lower latitude (45.4°N, 75.6°W) transmitter including routine Faraday rotation reversal events. One of the motivations of this research is to compare and contrast the Saskatoon SuperDARN conjunctions to the sub-auroral conjunctions with this Ottawa CW transmitter presented in Danskin et al. (2018).

3.3.2 Voigt Effect

The Voigt effect is the QT regime analogue to Faraday rotation from the QL regime for transionospheric radio wave propagation, typically demonstrated as oscillations in the ellipticity angle χ. In a liquid, the Voigt effect is often referred to as the Cotton-Mouton effect (Zvezdin and Kotov, 1997). This phenomenon is rarely, if ever, reported among recent ionospheric research and has therefore taken some considerable effort on my part to explain it and apply it to this research. Even though the QT approximation regime is more dominant for a smaller range of aspect angles, this research and Danskin et al. (2018) have shown that the Voigt effect is observed at all aspect angles. Just as Faraday rotation presents itself as a change in the orientation angle, the Voigt effect presents itself primarily as a change in the ellipticity angle. As explained above, an EM wave that is propagating transverse to the B-field will propagate as the superposition of two orthogonal linear polarization states. Since the O-mode of propagation experiences a higher index of refraction than the X-mode, it will change in phase with respect to the X-mode. As these two orthogonal linear modes of propagation are changing phase with respect to each other, the resultant measured polarization state will change. For example, a linearly polarized wave will become more elliptically polarized as the ellipticity angle increases. When χ reaches 45°, the wave is circularly polarized and then acquires the opposite elliptically polarized sense, then comes back to a linear polarization, then to the opposite circular polarization, and so on.

Again, the Voigt effect is not described in classic ionospheric literature, therefore we must look to the closest available description which can be found in a the Magnetooptics text Zvezdin and Kotov (1997). In order to get an idea of how to predict the Voigt effect, one can formulate equations that describe the extreme case of EM wave propagation exactly perpendicular to the B-field, $\theta = 90^\circ$ (Zvezdin and Kotov, 1997). To begin, we must use the dielectric displacement D of the electric field E of the EM waves since in this case the longitudinal component of the electric field may be non-zero. However, the dielectric displacement D of the wave will only have the two components which lie in the polarization plane of the ellipse. The D-vector is related to the E-vector of an EM wave by $D = \epsilon_0 E + P$, where ϵ_0 is the permittivity of free space and P is the polarization field. Now, using the D-vector a solution for a small uniform magnetized plasma medium of thickness ℓ is given as,

$$D = D_0 \begin{pmatrix} \cos\psi_0 \\ \sin\psi_0 \exp i\delta \end{pmatrix} \exp\left(-i\omega t + k_x \ell\right), \tag{3.14}$$

where D_0 and ψ_0 are the incident D-vector magnitude and orientation angle respectively, and δ is defined as $\delta = (k_0 - k_x)\,\ell$ (Zvezdin and Kotov, 1997). This is then solved for the explicit equations which relate orientation angle ψ and ellipticity angle χ to this value δ,

$$\tan 2\psi = \tan 2\psi_0 \cos\delta, \tag{3.15}$$

$$\sin 2\chi = -\sin 2\psi_0 \sin\delta. \tag{3.16}$$

These equations do not so succinctly describe the Voigt effect, compared to how Equation 3.13 describes Faraday rotation. Further deriving a simple expression for Voigt effect in transionospheric propagation was not done in Zvezdin and Kotov (1997), and proved to be too complex when attempted. However, characteristic information of the Voigt effect may be obtained from this equation. Firstly, as opposed to Faraday rotation which only affects the orientation angle, the Voigt effect will create a change in both the ellipticity angle and the orientation angle. However, for a typical RRI flyby the effect on orientation angle is unobserved since the orientation angle results are dominated by the Faraday rotation. If we were to consider the thickness ℓ as the stepsize in a piecewise integration, at around the F2 peak in the ionosphere, the gradient in plasma density is so large that $\delta = (k_0 - k_x)\,\ell$ becomes a very small number ($\delta < 0.2$ rad). Especially when applied to the general case, the change in orientation angle from the Voigt effect is therefore insignificant since the $\cos\delta$ term in Equation 3.15 remains approximately 1. In Equation 3.16, the term $\sin\delta$ remains significant since a small value of δ means that $\sin\delta \approx \delta$. For a value of $\delta = 0.2$ rad, a typical variation in χ of $\pm 45^\circ$ (as ψ varies $\pm 90^\circ$) is bound by the the scale factor and we observe an oscillation of about $\pm 5.7^\circ$ (this is observed in the results shown in Section 5.2). Secondly from Equation 3.16, the resultant ellipticity angle is dependent on the incident orientation angle. In the exactly transverse case, this detail amounts to providing a variable initial magnitude for each mode of propagation (which acts similar to a typical birefringent material). However, as soon as we apply the contextual understanding from these equations to a situation that is QT, the incident orientation angle is no longer constant. A wave propagating in the QT regime will still undergo Faraday rotation. In the general case, the Voigt effect is observed as an oscillating magnitude depending on the Faraday rotation state. This will be further demonstrated in the experimental results in Chapter 5 when the Voigt effect oscillation rate is found to coincide with the Faraday rotation rate.

CHAPTER 4

DATA HANDLING AND ANALYSIS TECHNIQUES

This chapter will cover the ways in which data was collected and analyzed. Here, data collection refers to both how an individual or set of ePOP flybys over the Saskatoon SuperDARN are planned and executed, and also to how the RRI data is received from ePOP and made available for the analysis. Data analysis refers to both how the RRI data is used to calculate results, but also to supplementary software and data sets which are used to further support understanding and interpreting the RRI data for an individual pass. These supplementary resources include models such as IRI (Bilitza, 2012) and Kp-index (The Helmholtz Centre Potsdam, 2019) along with a ray tracing modelling software provided by Rob Gillies (Gillies et al., 2012).

4.1 Planning an RRI-SuperDARN Conjunction

Typical RRI-SuperDARN flybys must be planned a couple weeks ahead of time for many reasons. First, ePOP operations works on a "store-and-forward" data system which means there is a limited amount of data ePOP can produce in a single day (Yau et al., 2006). The "store-and-forward" data system refers to how ePOP will record data from any of its instruments, store the data on board until it has a chance to pass over a ground station to transmit downlink telemetry data. Though ePOP has a data storage of 1 terabit (Tb) (125 gigabytes (GB)), over a single ground station flyby ePOP can only transmit a total of about 15 GB of data using its 300 megabits-per-second (Mbps) Ka-band downlink telemetry system. Through most of its lifetime so far, ePOP only had the Calgary ground station to transmit the data to, which would mean typically only a single downlink flyby per day. The current cooperation between some ePOP instruments and the European Space Agency (ESA) Swarm mission provides more opportunities for downlink flybys by using European ground stations (ESA, 2018). Even with the increased number of downlink opportunities RRI cannot be recording all the time, so any flyby must be planned ahead of time.

Secondly, the experiment is about the planned conjunction of two devices. When data is collected by RRI, ePOP needs to be passing in the field of view of the Saskatoon SuperDARN radar in order for the conjunction to occur. This requires planning using ephemeris data and the predicted ePOP trajectory to ensure RRI is “over top” of Saskatoon or northern Saskatchewan. During my research, I was assisted heavily by Gareth Perry, Andrew Howarth and the rest of the University of Calgary ePOP team in planning and executing all of the RRI conjunctions with the Saskatoon SuperDARN radar. They would find suitable flybys which fit my requested specifications and scientific goals. The start and end times of the upcoming RRI flybys would then be sent to the SuperDARN team here at the University of Saskatchewan to request a specific RRI operating mode for SuperDARN during the flyby. The SuperDARN operating mode called “epopsound” is the specially planned mode to use in conjunction with RRI measurements: we specify which beams we want to be transmitting on over the course of the flyby and what frequency we want the radar transmitting at.

This operation mode uses a 7 pulse code sequence with an interspersed 8 pulse code marker which can be used to determine precise timing information between ePOP and SuperDARN (Greenwald et al., 1995). However, the experiment is fully dependent on the position of the satellite from ephemeris data rather than being concerned about the time at which the SuperDARN pulses are transmitted.

4.1.1 Choosing Experimental Parameters

As flybys were continually planned, the parameters used and scenarios focused on were iterated upon as lessons were learned from previous RRI flyby results. Specifically, what changes could produce data sets with more accurate or more consistent observations (i.e. signal to noise ratio (SNR) high enough for observations). At the beginning of the ePOP mission, a potential objective of RRI data involved O- and X-mode separation which requires a radar frequency that is close to, but still greater than, the plasma frequency of the foF2 peak in the ionosphere (Kelley, 2009). However, the phenomenon was too unreliably observed because of an optimal radar frequency window which was too narrow and too variable to achieve consistently. If the radar frequency was too much higher than the foF2 peak, the O- and X-mode separation effect would be too minimal to be observed. And as mentioned, if the radar frequency was too low, the SNR in the RRI data could often be at unobservable levels for the flyby. A more immediate experimental system, one which does not require a planned pass weeks prior to the recording date, might be able to more suitably record this phenomenon. The variance in the plasma frequency of the foF2 peak was enough to cause observing this phenomenon with considerable inconsistency and unreliability. Therefore, the O- and X-mode separation phenomenon was eventually dismissed as a science objective for my research in favour of more consistent observations with a higher radar frequency. O- and X-mode separation can occasionally be observed with the higher radar frequency, but to a lesser extent and remains inconsistently observed.

Over the course of the research, and especially within the last two years, experimental parameters were commonly chosen to simplify data handling and to make observations of the physics more intuitive. Firstly, the radar frequency typically used at the beginning of the RRI observations was ∼11.2 MHz, in order to try and observe the O- and X-mode separation. But since the data was too often unclear or simply not observed at this frequency, the radar frequency was changed to be ∼14.5 MHz. This change made for considerably more consistent RRI observations which then could be interpreted. In Table 4.1, both the number of total RRI-SuperDARN Saskatoon conjunctions and the number of these flybys with usable RRI data are shown, and as can be seen the ratio of usable RRI data sets at 14.5 MHz radar frequency is much higher. A change was also made to the number of SuperDARN beams used in conjunctions. During conjunction flybys in the first year of the ePOP mission, SuperDARN was switching between as many as 13 beams once per second in planned conjunctions. This meant that during a flyby, ePOP would be rapidly switching in and out of the field of view of the currently transmitting SuperDARN. Though the radar signal could still be measured by RRI while a SuperDARN was transmitting on a beam pointed away from ePOP, the decision was made to significantly reduce the number of beams used to 7 beams, then to 3 beams, and eventually to only 1 beam transmitting in order to maintain a consistent signal to noise ratio during a flyby. This also eliminated synchronization of the SuperDARN beams with the RRI observations, which unnecessarily complicated the analysis. With the help of the

University of Calgary ePOP team, the single selected SuperDARN beam used during a flyby was the beam that most aligned with the groundtrack of ePOP.

To further maintain consistent radar signal during a flyby, ascending node flybys (ePOP traveling northeastward over Saskatoon) were also prioritized since this is also roughly the boresight direction of the Saskatoon SuperDARN radar. Descending node flybys in the field of view of SuperDARN Saskatoon instead cross over SuperDARN beams, which limits how long ePOP remains within a given field of view. The number of ascending and descending flybys are also listed in Table 4.1. The data analysis in Chapter 5 only uses flybys with a transmitted radio wave frequency of 14.5 MHz from the Saskatoon SuperDARN radar for consistency purposes. These 14.5 MHz flybys started being planned and collected starting in January 2018. As such, 19 flybys were planned over the next 10 months, prioritizing ascending, slewing, daytime flybys since these parameters most often presented usable data. However, slewing flybys were not always available, either due to other ePOP observing constraints or complications associated with flybys at low altitudes. Of the 16 usable flybys from this period only 6 flybys were slewing with altitudes $>$ 800 km. The other 10 flybys were in nadir orientation at low altitudes.

Finally, the most recent experimental priority comes from a direct comparison of my auroral research to the sub-auroral work of Danskin et al. (2018), which was singularly focused on a run of 5 sequential flybys within 5 days. By the nature of the nodal displacement of the orbit of ePOP with respect to the groundtrack (movement eastward over the same point on the ground in successive flybys), a sequence of flybys over a ground target is commonly found. Although planning flybys had often been for a sequence of successive flybys, to try

Table 4.1: RRI-SuperDARN Saskatoon Conjunctions

	Radar 11.2 MHz	**Radar 14.5 MHz**
Total flybys	69	19
Flybys with usable data	33	16
Ascending flybys	47	17
Descending flybys	22	2

and replicate the favourable sub-auroral results from the Danskin et al. (2018) paper, this proved to be problematic, even though planning for successive flybys was a high priority for this research.

4.2 Data Format

Once an RRI-SuperDARN Saskatoon conjunction took place, the RRI data would be available for download from the ePOP database (ePOP Database, 2019) typically within a few days to a couple weeks after the flyby. The HDF5 RRI data file would then be downloaded for the analysis. Hierarchical Data Format (HDF) is a file format designed to store and organize large amounts of data. These files are often on the order of 1 GB in size and are created by the ePOP ground station team in Calgary after receiving the transmitted downlink data from ePOP. The HDF5 file type simplifies the file structure to include only two major types of objects: “data sets”, which are multidimensional arrays of a homogeneous type and “groups”, which are container structures which can hold data sets and other groups (HDF Group, 2018). In the case of RRI, the HDF5 file format is filled with not only the dipole voltage data recorded by the RRI in its cross-dipole format, but also contains all the ephemeris and timestamped data recorded on board ePOP during the flyby. The HDF5 format of each flyby is read by the "read_rri_lv1_struct.pro" IDL code (code I modified by Gareth Perry), which unpacks the file into arrays for my analysis and plotting.

RRI data is best handled in I/Q data (in-phase and quadrature) format, which is common practice in RF (radio frequency) communications, including telemetry data transmissions, in order to make more efficient use of typical hardware circuitry. This means that both the magnitude and phase of the RRI voltage data is presented simultaneously in complex number format. Since calculation of the polarization ellipse is dependent on the orthogonal components of the EM wave, the RRI voltage data must also be presented in orthogonal components; this means the four monopoles of RRI must be configured into orthogonal dipoles. Both I/Q data and dipole voltage calculations are done on board the spacecraft in real-time through RRI hardware James (2006). As presented in Figure 2.2, a component labeled Differential Comparison is switched on for RRI data sets recorded in "Analog Dipole Mode" (the recording mode that all RRI-SuperDARN conjunctions are operated in). This simple differencing component immediately contrasts the voltages of two monopoles across from each other as they are being measured, creating the total dipole voltage. The dipole voltage is then mixed with a local oscillator (LO) of programmable frequency (chosen to be close, to but not exactly the radar frequency). The LO is a complex-number device of two sine waves with a 90° phase difference and mixes the dipole voltage into the desired I/Q signals.

4.3 Experimental Formula for Analyzing RRI Data

The complex voltage data for both RRI dipoles then needs to be used to calculate the polarization angles in order to compare with theory. The measured voltages on the dipoles are each directly related to the incoming electric field of the SuperDARN radar signal (Gillies et al., 2010). The electric field $\mathbf{E}$ of an EM wave may be described in Cartesian coordinates as $\mathbf{E} = E_x \exp(i\,(\omega t - kz + \phi_x))\hat{\mathbf{x}} + E_y \exp(i\,(\omega t - kz + \phi_y))\hat{\mathbf{y}}$, where E_x and E_y are the amplitudes of the electric field in each direction, ϕ_x and ϕ_y are the phase of the electric field in each direction (Hussey, 1994). From Hecht and Zajac (1974), the ellipticity and orientation angles (χ and ψ) are calculated using the equations,

$$\sin 2\chi = \frac{2E_x E_y \sin\epsilon}{{E_x}^2 + {E_y}^2}, \tag{4.1}$$

$$\tan 2\psi = \frac{2E_x E_y \cos\epsilon}{{E_x}^2 - {E_y}^2}, \tag{4.2}$$

where ϵ is the phase difference between each dipole ($\epsilon = \phi_x - \phi_y$). The exact relationship between the magnitudes of voltage V and electric field E is not required as long as it is assumed that both dipoles are both related directly by some unknown constants c_1 and c_2 to their respectively measured voltages magnitude ($V_x = c_1 * E_x, V_y = c_2 * E_y$). In place of electric field, the measured voltage is used to solve for the ellipticity and orientation angles. Each dipole magnitude and phase are simply calculated by taking the magnitude and phase of the combined complex voltage data arrays. The values of the constants c_1 and c_2 are dependent on both the attitude of the spacecraft (which can be off by $\sim 10^\circ$ even while slewing) and the amount of beam bending on the radar signal (which can be up to $\sim 10^\circ$,

Table 4.2: Percentage Error from a 15° Misalignment of RRI

	Error in χ	**Error in ψ**
For Circularly Polarized	2.2%	Unaffected
For Linearly Polarized	Unaffected	$< 3.5\%$
For a General Ellipse	$< 3.5\%$	$< 5.4\%$

but typically $\sim 5°$ (Gillies, 2010)). Table 4.2 demonstrates the percent error in the calculated orientation angle ψ and ellipticity angle χ from a 15° difference between RRI normal and the k-vector in the direction of one of the dipoles. The amount of error in a linearly polarized wave is dependent on the orientation angle of the incoming wave, therefore a peak value of 3.5% is presented in Table 4.2. Similarly, the peak values for a general ellipse that is mostly linear is presented in Table 4.2. However, as the polarization becomes more circular the orientation angle becomes less significant to describing the polarization ellipse and the percent error in the orientation angle begins to rapidly increase. The error in orientation angle exceeds 5.4% once ellipticity angle exceeds $\sim 33°$ and approaches 100% uncertainty when the wave is close to circular. This is expected since the orientation angle of a circularly polarized wave is arbitrary.

4.4 RRI-SuperDARN Data Analysis Software

The "pulse_seeker.pro" program is the software used to produce data plots and analyze RRI data. Originally written by Gareth Perry and modified for my analysis, this is an IDL program which reads in the HDF5 file of RRI data and then creates and saves a number of different plot formats in order to display and interpret the RRI data. For my research, I modified the program in a number of different ways: improved shorter analysis times through code optimizations, including speed improvements associated with HDF5; creation of a number of different geometric plots of key parameters such as boresight orientation, magnetic field orientation (**B**) radio wave orientation (**k**), etc., from the ePOP ephemeris data needed for my analysis and RRI analysis in general; plus improving the abilities, accuracy and functionality of the analysis plotting algorithms.

The first thing the program does is call the "read_rri_lv1_struct.pro" IDL program in order to unpack the HDF5 file into ephemeris data and voltage data. The complex dipole voltage data is then used to produce the ellipticity and orientation angles using the equations detailed in Section 4.3.

The ephemeris data was used to calculate numerous geometric vectors which were then used to produce geometric line plots. These plots show how a given relevant geometric parameter of an ePOP flyby changes during the conjunction. The LOS vector from SuperDARN to ePOP was used to define the radio wave k-vector. Technically there could be some refraction of the k-vector in the plasma medium of the ionosphere, but this has been shown to be small by Gillies (2006) as discussed in Section 3.1, and therefore a straight line was used for simplicity in the calculation. Such geometric calculations include:

- the aspect angle θ (the angle between the radio wave k-vector and magnetic field, B, local to ePOP)
- the angle Δ between the k-vector and the RRI normal direction

- the angle Φ between between the k-vector and ePOP ram direction (the direction of the motion of the satellite).

One of the prime data visualization plots created by the program are strip plots of the dipole voltages (both dipoles 1 and 2), ellipticity angle and orientation angle. These plots have the goal of only viewing the relevant data during a SuperDARN pulse from a flyby in a single plot (or two) while leaving out the plethora of insignificant interpulse data. The strip plots are colour contour plots of RRI data sets, with UT (universal time) along the x-axis (along with ephemeris data including geographic longitude and latitude, magnetic longitude and latitude, magnetic local time and altitude of the spacecraft) and pulse time in microseconds (μs) along the y-axis. To make these plots, the analysis algorithm first creates matrices from the dipole voltage data and polarization angles, picking out individual SuperDARN pulses by searching for peaks in intensity in one of the voltage arrays and placing an array of 200 data points (which in total is a 3.2 ms window) around that peak as a column in the matrix. This is then repeated for each SuperDARN pulse in the RRI data. Using the voltage peaks as reference for alignment, the other arrays of ellipticity angle, orientation angle and ephemeris data are similarly formed into matrices. An example of a strip plot from an ePOP SuperDARN conjunction on 16 June 2018 is shown in Figure 4.1. It shows the higher intensity of the SuperDARN pulse data in the center of each column surrounded by some interpulse data, coloured in blue.

The strip plots sometimes do not portray enough detailed information about phenomena such as the Voigt effect. To account for this, a number of line plots are made from the above matrices. These line plots isolate the data of the SuperDARN pulses, take an average data

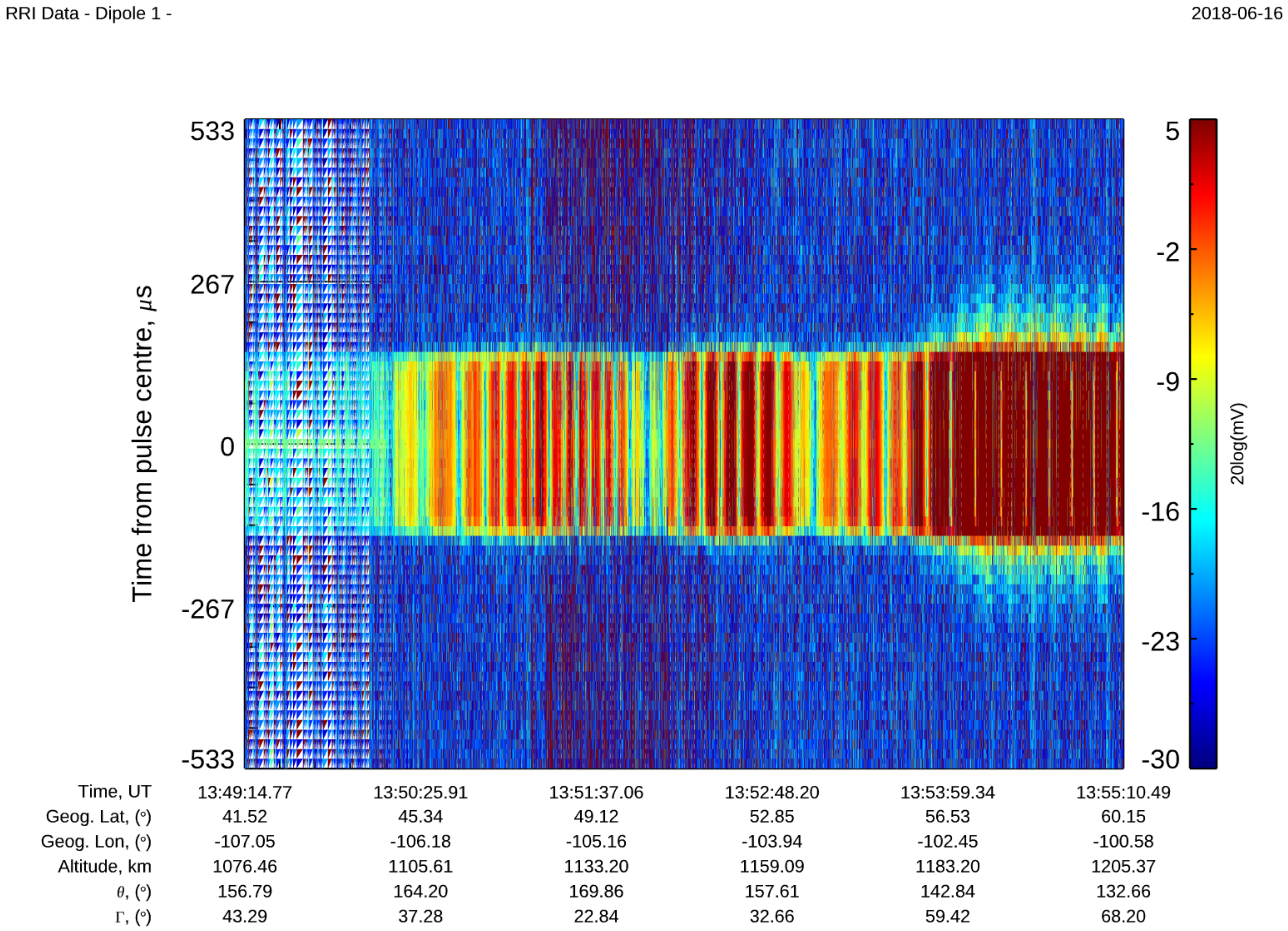

Figure 4.1: Example Strip Plot of RRI Dipole 1 voltage magnitude from the slewing RRI-SuperDARN Saskatoon flyby on 16 June 2018

result of each pulse and record the result in a new array. Since a SuperDARN pulse is 300 μs and RRI samples at a rate of 62500 samples per second, RRI records about 18 samples per pulse in RRI data. The way pulses are centred in the strip plot matrices can cause the pulses to be off center by a few data points. Additionally, even though O- and X-mode separation is not focused on, it can still happen. Since current research goals are focused on data relying on the interaction between both modes of propagation, 5 points from the center of the column are averaged to calculate values from the pulse. This was the highest number of data points that gave the most consistent calculation results.

4.5 Supplementary Analysis Tools

Along with the primary data set from recorded RRI data, supplementary analysis tools and data sets are used to interpret the RRI observations. Firstly, using the equations from the magnetoionic theory, especially the Appleton-Hartree equation, IRI electron density profiles were used to calculate example plots and figures (Bilitza, 2012). An example using an IRI modelled ionosphere is shown in Figure 4.2. Figure 4.2 shows the percentage of Faraday rotation throughout the ionosphere. Here it can be seen that ∼80% of the total observed Faraday rotation takes place within 100 km of 325 km altitude. This was a single calculation out of many to give insight to physics and for comparisons to observations made by Gillies (2010), which showed a similar observation of Faraday rotation and scattering altitudes mostly impacted by the region of the ionosphere immediately surrounding the F2 peak. Also using IRI data, the ray-tracing model presented in Gillies et al. (2012) was used to simulate a given ePOP flyby over the Saskatoon SuperDARN radar. It output expected measured polariza-

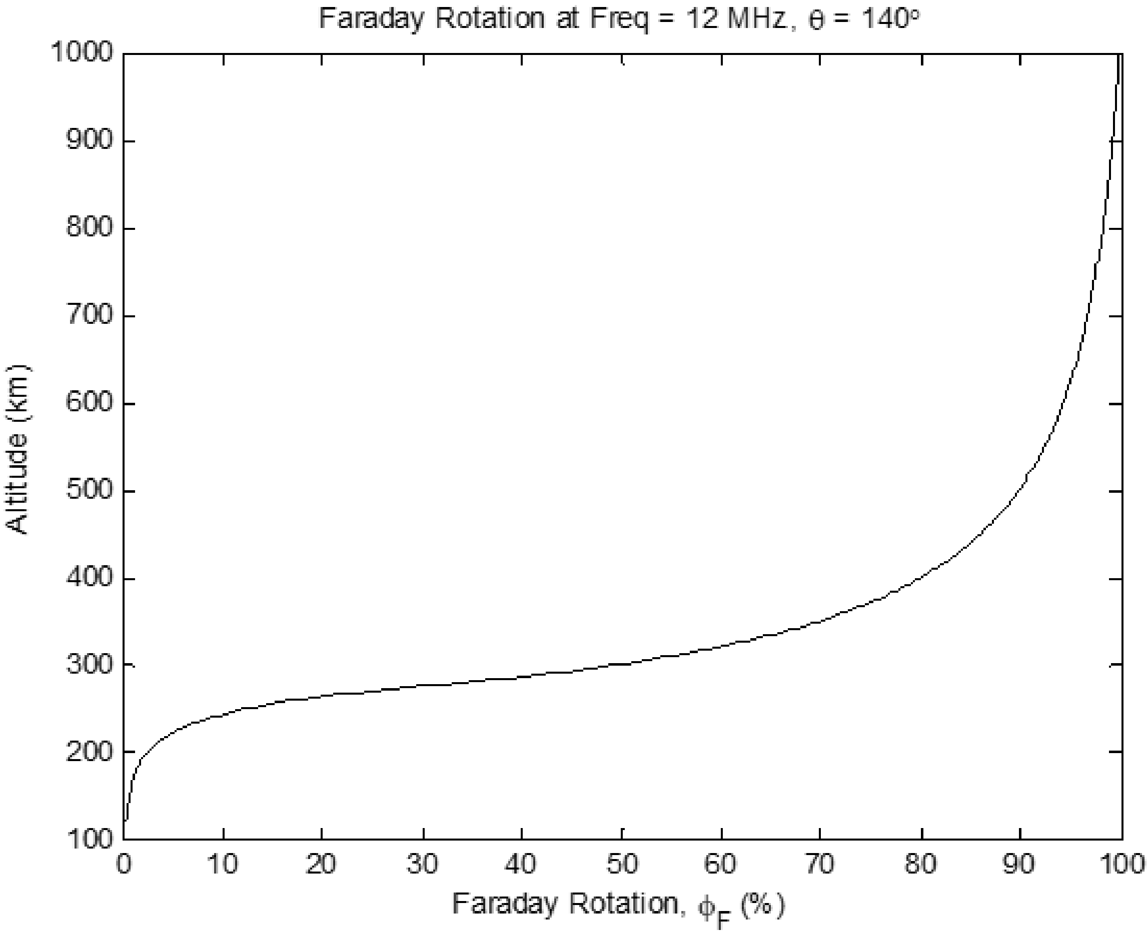

Figure 4.2: Calculation of percentage of Faraday rotation rate along altitude using the IRI model, with a radar signal of 12 MHz and an aspect angle of 140°.

tion data based on the Appleton-Hartree equation and ephemeris data from the flyby. An example is presented in the next chapter.

In order to understand the state of the ionosphere on a given flyby, two different external data resources were used: the Kp-index (The Helmholtz Centre Potsdam, 2019) and ionospheric parameters determined using CHAIN Ionosondes (CHAIN, 2019). The Kp-index quantifies disturbances in the horizontal component of the magnetic field of the Earth with an integer in the range 0-9, 1 being calm and ≥ 5 or more indicating a geomagnetic storm.

It is derived from the maximum fluctuations of horizontal components observed on a magnetometer during a three-hour interval. The planetary 3-hour-range Kp-index is the mean standardized Kp-index from 13 geomagnetic observatories between 44° and 60° degrees (north or south) geomagnetic latitude (The Helmholtz Centre Potsdam, 2019). As will be reported next chapter when discussing a flyby, the Kp-index will be used to interpret the state of ionosphere and whether it is in a quiet time or not.

Ionograms from nearby ionosondes can make a direct measurement of the state of the ionosphere. Data from some Canadian Advanced Digital Ionosondes (CADI), which are part of the Canadian High Arctic Ionospheric Network (CHAIN) were also used to interpret the RRI observations. These ionosondes view directly upwards, sweeping from 0.1 to 30 MHz, recording the time delay before receiving the reflected signal back of each frequency (CHAIN, 2019). Such measurements give a clear picture of the bottom-side ionosphere at the time and place of the measurement. From an ionogram, two important details can be determined which are the observed altitude and plasma frequency of the F2 peak in the ionosphere (hmF2 and foF2 respectively). Though these values can be reported automatically by some ionosondes, they are not reported directly by the CADI ionosondes in CHAIN and required some analysis on my part. Also, the nearest operational ionosonde to Saskatoon is at Cambridge Bay, Nunavut (69.10°N, 105.11°W). This is sufficiently distant from Saskatoon that it does not give clear information on the immediate Saskatoon ionospheric condition. Although, the large geographical extent of RRI flybys would require multiple ionosondes to fully characterize the path the sparse distribution of ionosonde stations means only a few could be used. Cambridge Bay often lies on the path of an ePOP ascending conjunction, northeast of Saskatoon, which is why it was chosen as the most suitable ionosonde to contextualize RRI data. In the event that the Cambridge Bay ionosonde did not record data or the ionogram does not give usable data, the ionosonde at Resolute Bay, Nunavut (74.75°N, 95.00°W) was used as a secondary source for hmF2 and foF2. This ionosonde is further away from a typical RRI Saskatoon SuperDARN conjunction, but was able to give some information about the state of the ionosphere.

CHAPTER 5

RRI-SUPERDARN DATA AND ANALYSIS

This Chapter presents and analyzes the polarization patterns that were observed in the RRI data from the RRI-SuperDARN Saskatoon conjunction experiments. These phenomena include the Faraday rotation rate, Faraday rotation reversal events and the many types of Voigt effect patterns. The chapter begins by covering the data and observations by Danskin et al. (2018) about sub-auroral Faraday rotation and the Voigt effect with RRI. Comparisons and contrasts are made between Danskin et al. (2018) and the aurora zone observations in the thesis. One typical flyby will be completely detailed, with figures such as: aerial view of the groundtrack of the flyby, strip plots of dipole voltage, orientation angle and ellipticity angle; line plots of orientation angle, ellipticity angle and four geometric angles; the relevant ionogram from Resolute Bay; and the simulation results of the Gillies et al. (2012) ray-tracing model. When discussing other RRI flybys in the remainder of the chapter, not all of these plots will be shown, but rather only the most relevant ones. Each significant feature or phenomenon will then be further discussed and detailed in individual sections. All of the RRI-SuperDARN Saskatoon flybys shown in this chapter are ascending flybys performed with a fixed 14.5 MHz transmission from the SuperDARN Saskatoon radar. This is both because the consistency helps to relate flybys to each other, and because the 14.5 MHz observations are typically the most usable data sets.

5.1 Previous study results

The observations made by Danskin et al. (2018) follow a sequence of 5 flybys over an HF transmitter connected to an End Fed Inverted-V antenna in Ottawa from 18 April to 22 April, 2016 with a radio wave transmission frequency of 10.422 MHz. These flybys highlighted a certain set of observations that were critical in forming my research objectives. These include the Faraday rotation reversal point along an ascending flyby and some initial inquiries into the Voigt effect. Figures 5.1 and 5.2 show the RRI data from the 18 April 2016 flyby over Ottawa (where Figure 5.1 is a 10 s period of data and Figure 5.2 is a 4 min period of data), specifically plots of the the observed power on RRI, the polarization ratio p, the orientation angle ψ, and the ellipticity angle χ. The polarization ratio is defined as the ratio of the incoming polarized intensity to total incoming intensity; the total intensity being the sum of the polarized and unpolarized (randomly polarized) components. The observed power on RRI is representative of the transmitting sequence of the Ottawa transmitter as ePOP passes over, shown in the sharp spikes which are features from the transmitter and its operations as it alternates between a continuous wave (CW) sequence and a Binary Phase Shift Keyed (BPSK) sequence (Danskin et al., 2018). What is also observed in Figure 5.2(a), for the much longer 4 min duration of the pass, is the varying intensity that is measured by RRI and how the transmitter gradually begins to be observed as ePOP flies closer to Ottawa and then gradually fades out as ePOP flies away from Ottawa. For reference, the point in this flyby that is closest to Ottawa is at the 22:30:00 UT mark. The polarization ratio plot shows evidence that for as long as significant transmitted power is reaching ePOP, the polarization ratio is essentially unity, i.e. the signal is effectively completely polarized and/or

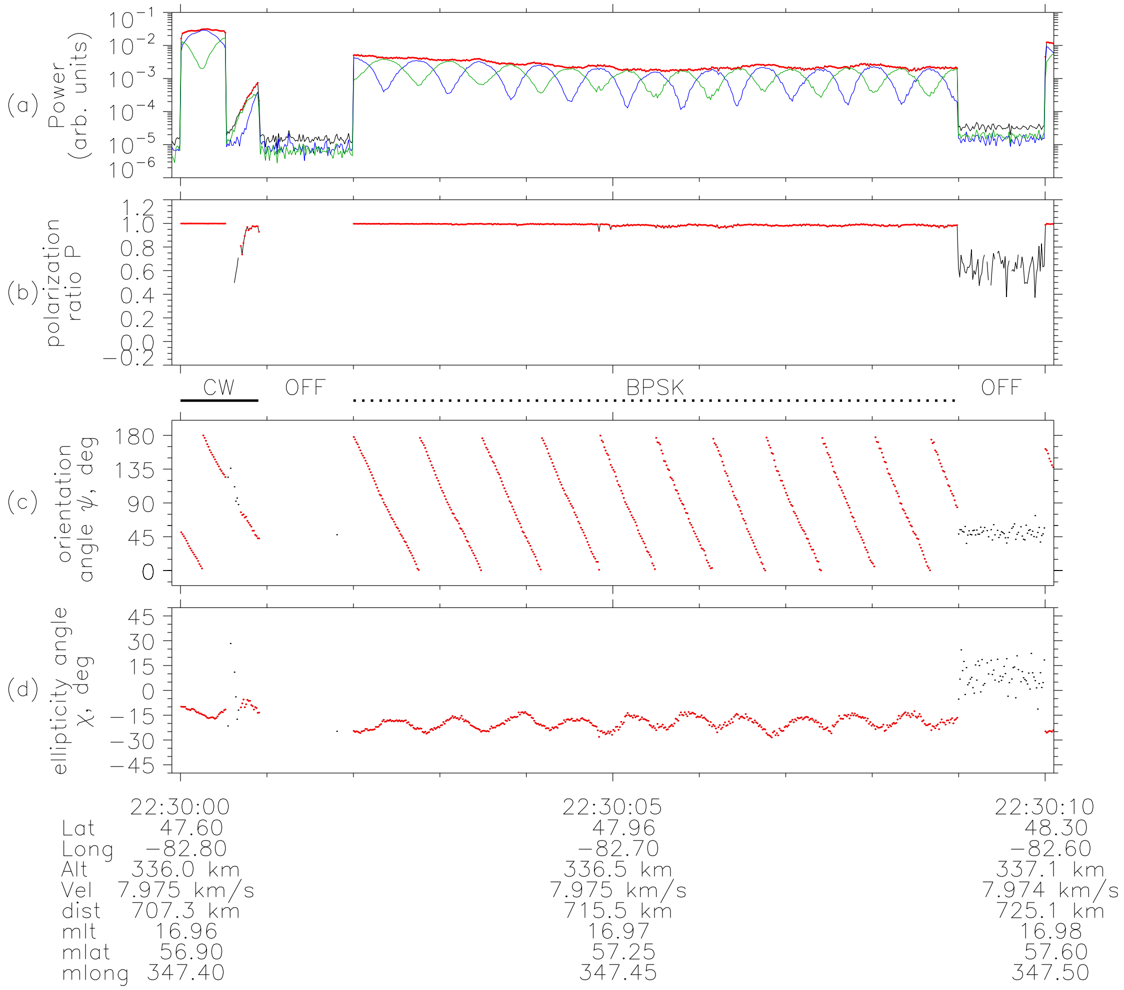

Figure 5.1: Power and polarization parameters for a 10 s period of the RRI flyby on 18 April 2016 over the Ottawa HF transmitter. Plotted are (a) the total power (b) the polarization ratio P, (c) the orientation angle ψ and (d) the ellipticity angle χ of the received radio wave.

measurement error is very small.

Finally, the two bottom plots of orientation angle and the ellipticity angle relate the physical phenomena of interest in this thesis. The first observation that can be made about the orientation angle is its rate of change, more distinctly shown in Figure 5.1(c). To clarify the effects that are being observed here, the continually rotating orientation angle depicted in this figure is not the explicit measurement of Faraday rotation. Faraday rotation is the

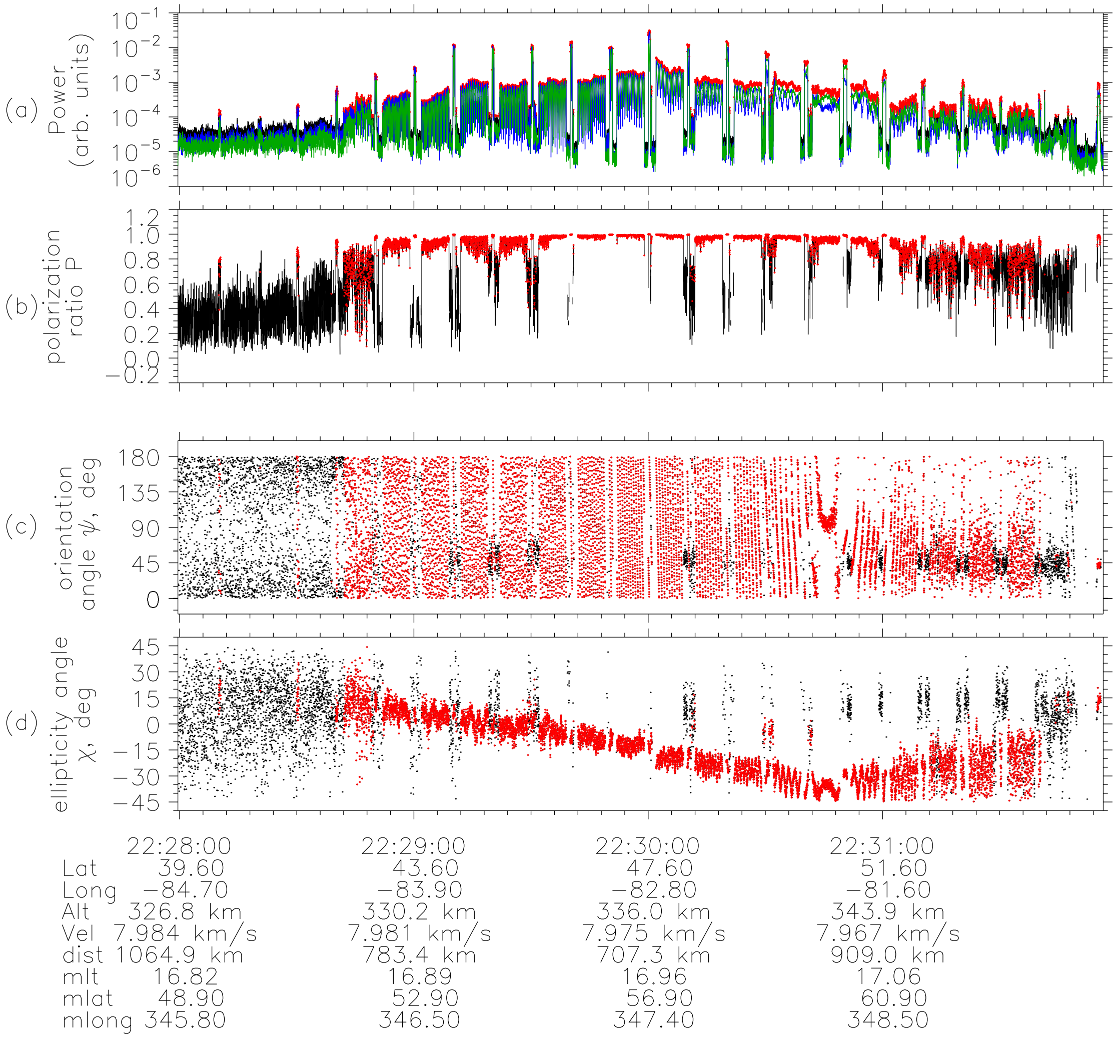

Figure 5.2: Power and polarization parameters for a the full 4 min period of the RRI flyby on 18 April 2016 over Ottawa HF transmitter. Plotted in the same layout as Figure 5.1.

continual rotation of the orientation angle as the wave is traveling. What is observed in the orientation angle measured by RRI is the received Faraday rotation of the wave at the particular point in space of ePOP, given by the aforementioned Equation 3.13, repeated here,

$$\phi_F = \frac{e^3 \mu_0 c}{2{m_e}^2 \omega^2} \int B \cos\theta N_e d\ell.$$

As ePOP moves in its orbit, the total resultant Faraday rotation changes which also gives a similar rotating pattern, which is why the gradually changing pattern of the total resultant

Faraday rotation will commonly be referred to as simply Faraday rotation from here on.

Observed in the longer period of Figure 5.2 at 22:30:45 UT, is a feature referred to as the Faraday rotation reversal point (Danskin et al., 2018). This is seen in how the Faraday rotation rate observed by the slope in the orientation angle gradually slows down (slope becomes less vertical and lines separate more) over the flyby, until finally at a reversal point in which the Faraday rotation rate further slows down and then reverses (slope changes direction from negative to positive). As mentioned before, this does not mean that the real Faraday rotation is reversed after this point, but that the total resultant Faraday rotation has changed from gradually decreasing to gradually increasing. To contextualize this, we can look at Equation 3.13 again. If the equation for Faraday rotation was purely dependent on the TEC term $N_e d\ell$ then the observed Faraday rotation on RRI would be symmetric about the closest point on the flyby to Ottawa (the 22:30:00 UT mark). However, since this reversal point is shown to be at a point further north than this, there is considerable contribution from the magnetic field term $B\cos\theta$. The paper by Danskin et al. (2018) demonstrates that the Faraday rotation reversal point remained relatively stable among its 5 flybys. The observed Faraday rotation reversal points in the Danskin et al. (2018) paper also all remain in the sub-auroral region. Comparing the Saskatoon experiment to this paper helps achieve the research goal of studying transionospheric radio wave propagation and structure in the ionosphere. All of the observed Faraday rotation reversal points in the 2018 Saskatoon SuperDARN conjunctions were observed within or very close to the auroral oval. A difference in observations between the sub-auroral and auroral regions can lead to conclusions made about difference in structure in the ionosphere.

Another observation that is demonstrated in the data from Danskin et al. (2018), is an analogous type of reversal in the ellipticity angle. This phenomenon is not observed in the auroral region Saskatoon flybys and is also not demonstrated in modelled ray-tracing calculations. The paper shows that this apparent reversal point does not always coincide with the Faraday rotation reversal point, but also does not have as clear an explanation as the Faraday rotation. This could be an instance of significant X-mode absorption since it is not considered in the modelling. However, these observations are during undisturbed ionospheric conditions and therefore very little absorption is occurring. The beam pattern of the Ottawa transmitter antenna is more complicated and could also be the cause. Further investigation into this reversal in the ellipticity angle is needed. It also shows an example of both QT (dominated by the Voigt effect) and QL (dominated by the Faraday rotation) effects occurring simultaneously. The flybys presented in Danskin et al. (2018) had significant consistency, occurred in the sub-auroral region, and occurred during relatively undisturbed magnetic conditions with small Kp-index values (≤ 1). For the RRI flybys in conjunction with the Saskatoon SuperDARN radar, the observations were in the auroral zone and occurred during more disturbed conditions with Kp-index values between 1- and 3+. Comparing the Voigt effect observations between the Saskatoon and Ottawa flybys could lead to a more general understanding of effects of magnetic disturbances upon this phenomenon.

5.2 Typical Flyby Results

The following section presents in detail a flyby from 16 June 2018. This gives a basis for what type of data is available and needs to be recorded from a single flyby, and what features or phenomena can be observed and interpreted. This will be the only flyby that is fully elaborated in this way. Only the most relevant figures will be shown for subsequent flybys presented in this chapter.

The flyby that takes place on 16 June 2018 at 13:51:14 UT (7:51:14 local time) is an ascending flyby with a Kp-index of 0+. This is a slewing flyby which means that over the course of the flyby ePOP attitude is continually adjusted such that the normal direction of RRI will be pointed towards the Saskatoon SuperDARN radar. First, the groundtrack of the flyby is presented in Figure 5.3 and shows ePOP passing by east of the Saskatoon SuperDARN radar. The flyby is an ascending flyby, therefore the motion of the spacecraft is northward (upwards in Figure 5.3). The next set of plots to be shown for this flyby are the 4 strip plots of Dipole 1 voltage (Figure 5.4), Dipole 2 voltage (Figure 5.5), orientation angle (Figure 5.6), and ellipticity angle (Figure 5.7). As was discussed in the previous chapter, strip plots are laid out such that each incoming SuperDARN pulse is centred and presented along the vertical axis in units of microseconds (μs), while the horizontal axis follows the ground track of the ePOP flyby. The data for dipole voltage is then presented as a colour contour in decibels (dB) for each dipole. We can see the intense signal from SuperDARN centred vertically in the middle for the entirety of the flyby and the surrounding low power background interpulse data. Similarly, the corresponding calculations for orientation angle (Figure 5.6) and ellipticity angle (Figure 5.7) are presented in the exact same format with respect to the axes. The colour contours for these plots have scales of $-90°$ to $+90°$ for the orientation angle and $-45°$ to $+45°$ for the ellipticity angle. In the orientation angle strip plot (Figure 5.6), the Faraday rotation effect can already be observed from the rapid colour

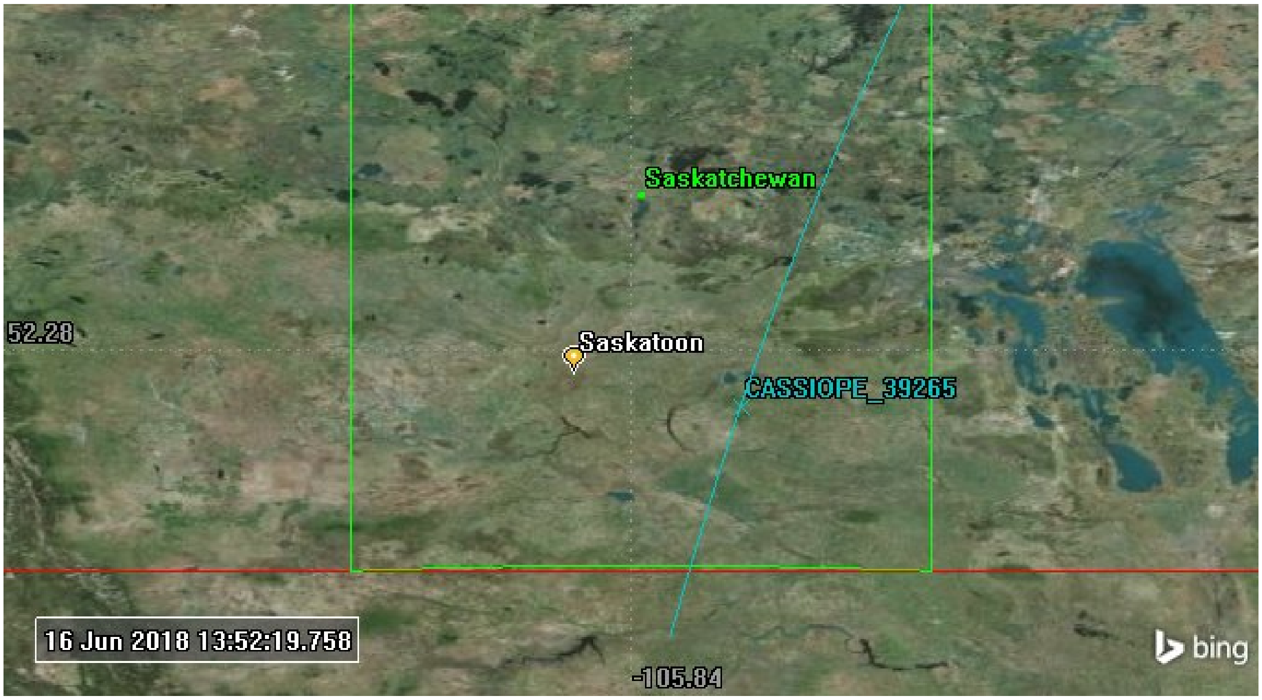

Figure 5.3: STK groundtrack view of the RRI-SuperDARN Saskatoon flyby on 16 June 2018. [Courtesy: University of Calgary ePOP team]

transitions as the orientation angle is constantly rotating creating the rapid rainbow effect. The ellipticity angle in contrast is essentially linear ($\chi = 0°$) over the course of the flyby with a few short deviations, but still without much detail. There is a small amount of O- and X-mode separation that can be observed in the pulses. It can be seen in Figure 5.7 as a strip of isolated O-mode is observed first (along the bottom of each pulse), followed by the mix of the two modes of propagation, and then a strip of isolated X-mode (along the top) (Gillies, 2006). This effect is to such a small extent (because of the radar frequency) and is inconsistently observed across various flybys. Therefore, the phenomenon is not considered in this thesis.

To view more details about both the orientation angle and the ellipticity angle, line plots are presented in Figures 5.8 and 5.9 respectively. Figure 5.8 shows a continually rotating

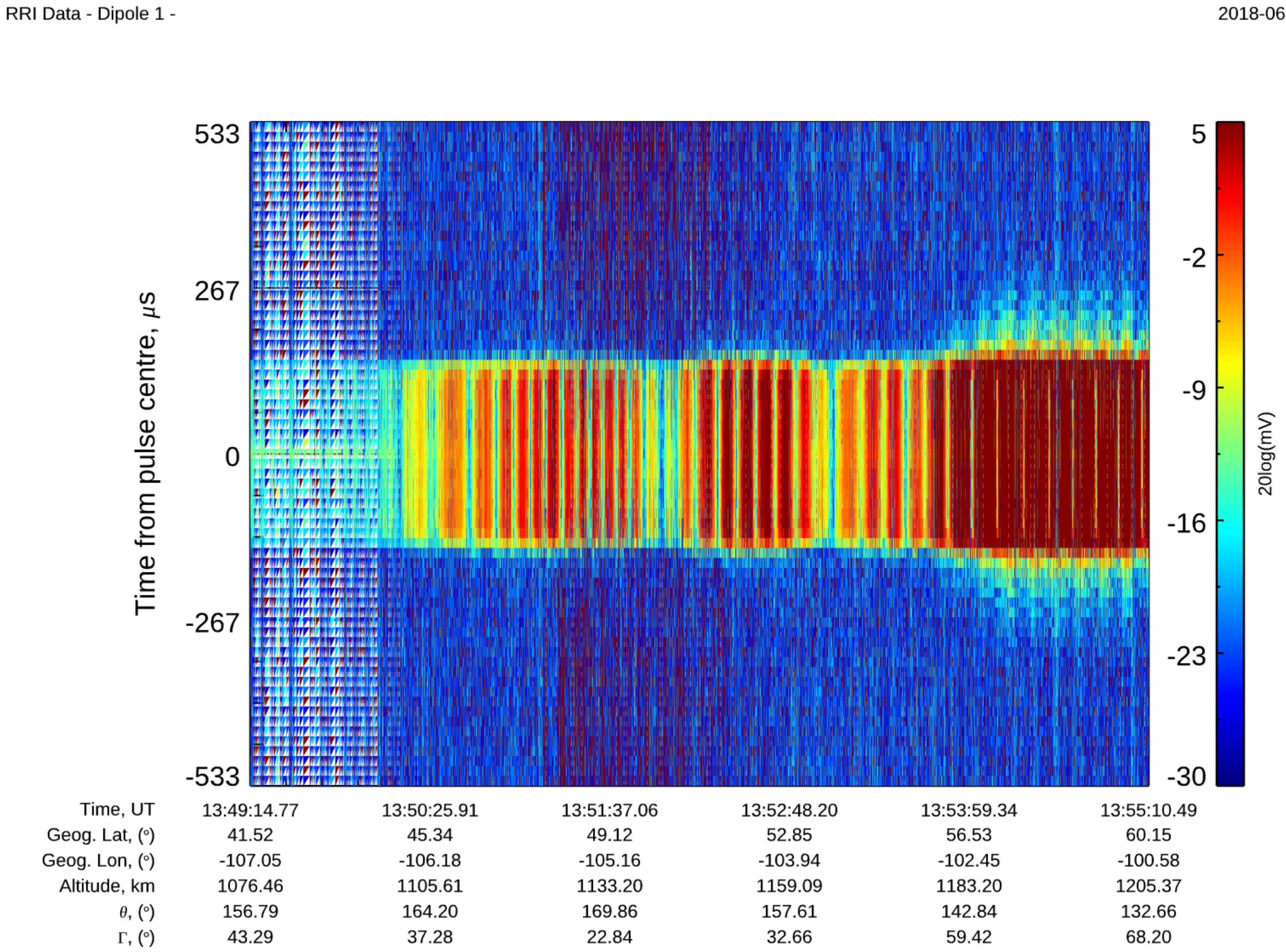

Figure 5.4: Strip plot of RRI Dipole 1 voltage magnitude from the slewing RRI-SuperDARN Saskatoon flyby on 16 June 2018.

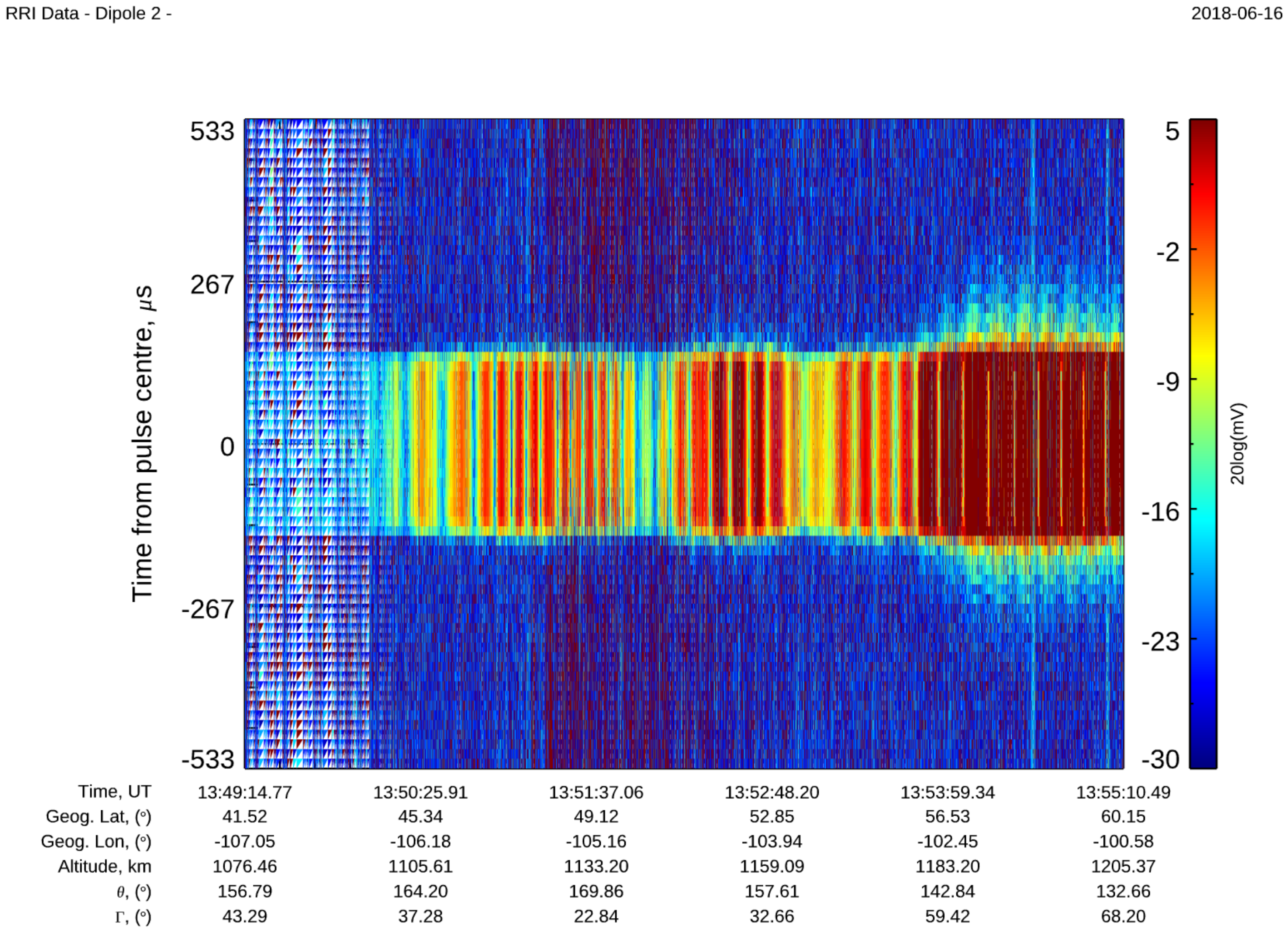

Figure 5.5: Strip plot of RRI Dipole 2 voltage magnitude from the slewing RRI-SuperDARN Saskatoon flyby on 16 June 2018.

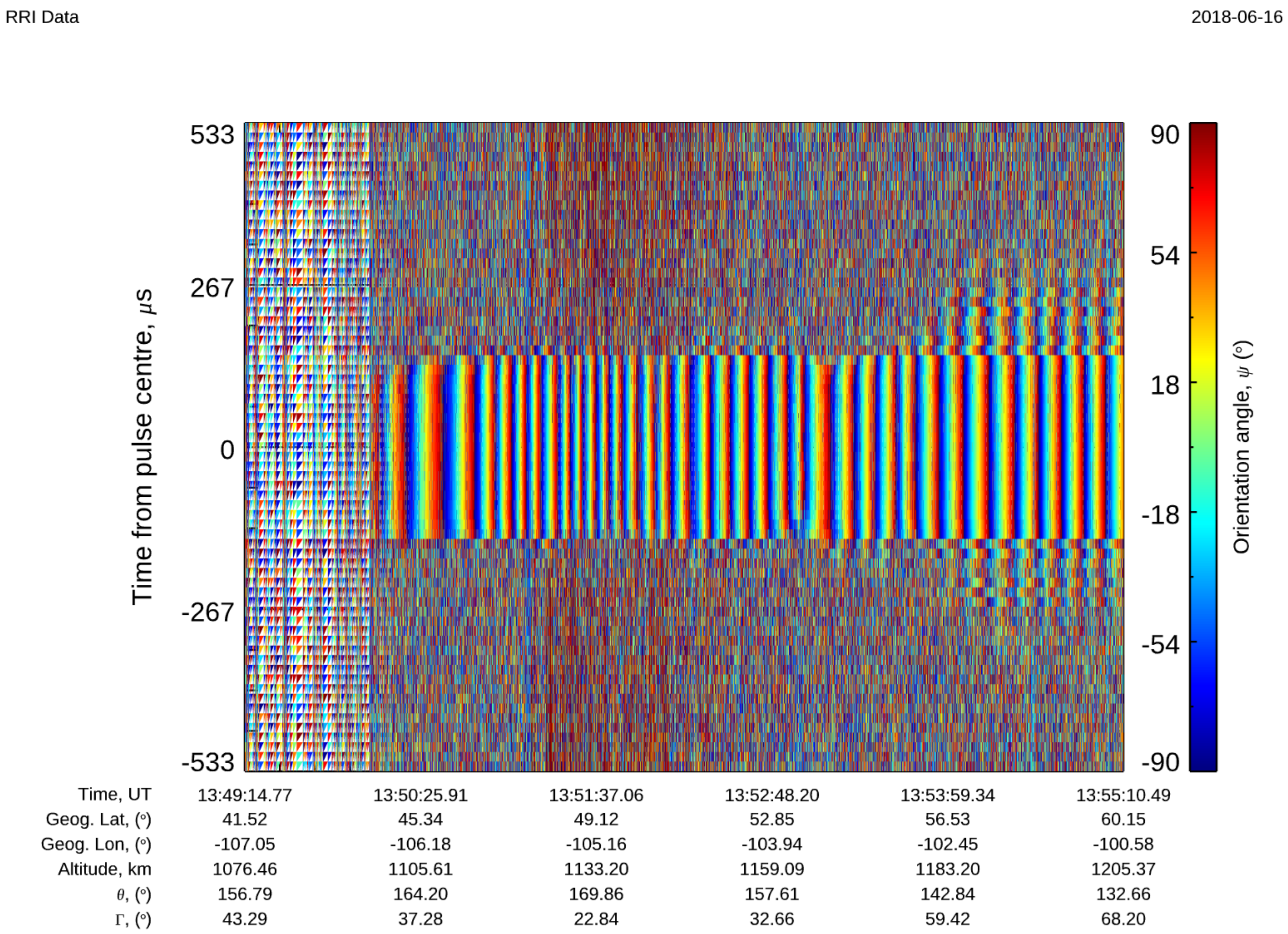

Figure 5.6: Strip plot of orientation angle ψ from the slewing RRI-SuperDARN Saskatoon flyby on 16 June 2018.

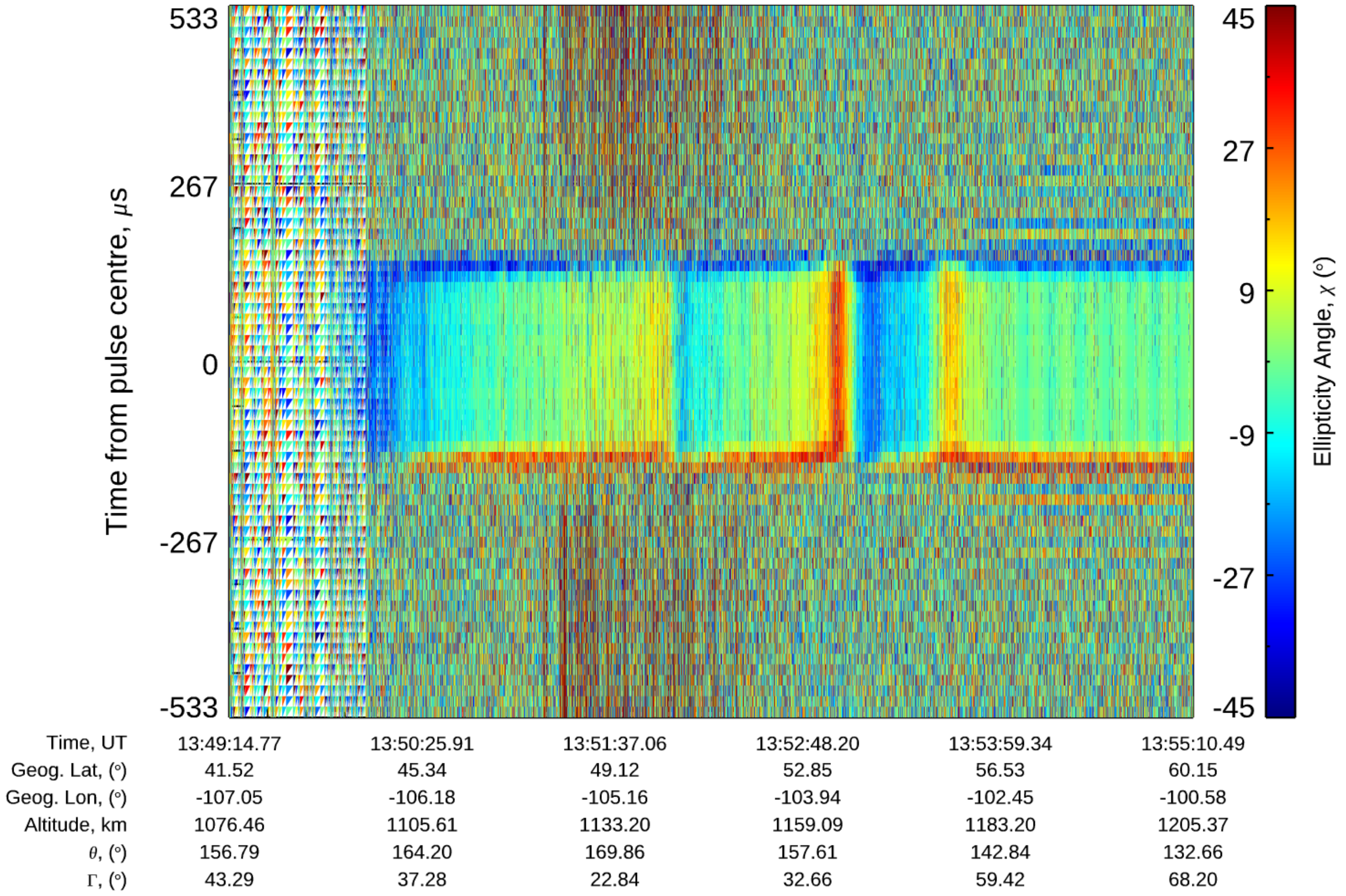

Figure 5.7: Strip plot of ellipticity angle χ from the slewing RRI-SuperDARN Saskatoon flyby on 16 June 2018.

orientation angle demonstrating the Faraday rotation effect. What is particularly advantageous of this line plot presentation over the strip plot format is how much more clearly it is seen that the rate of Faraday rotation at the end of the flyby is slower (as it is approaching a Faraday rotation reversal point) than the rate of Faraday rotation at the beginning. It also has the advantage of much more simply identifying a Faraday rotation reversal event if one were to occur. Figure 5.9 similarly shows the line plot of the ellipticity angle over the flyby and we can see the data is a lot more intricate and patterned than what could be determined from the strip plot of the same data. There is a constant small oscillation in the ellipticity angle, but this oscillation has a superposition-type behaviour with respect to a signature with distinct and particular peaks or spikes. Also observed in the northward part of the flyby is that the Voigt effect oscillations occur about a slightly right-handed bias (average $\chi < 0^\circ$ when RRI normal is anti-parallel to the k-vector). This could be caused from the X-mode propagation experiencing a greater amount of absorption than the O-mode (Gillies, 2010) and absorption is not considered in the theory. However, the observations presented in this thesis are all in undisturbed conditions so only a very small amount of absorption would occur. Additionally, preliminary modelling has shown that the biasing can even occur in calculations that do not consider absorption. The oscillation in the ellipticity angle of about $\pm 5.7^\circ$ is expected from the theory of the Voigt effect (Section 3.3.2). However, the multiple large peaks over the flyby have not been reported before, including the flybys reported from the Ottawa-RRI observations by Danskin et al. (2018), and have to be explored (further discussed in Section 5.5).

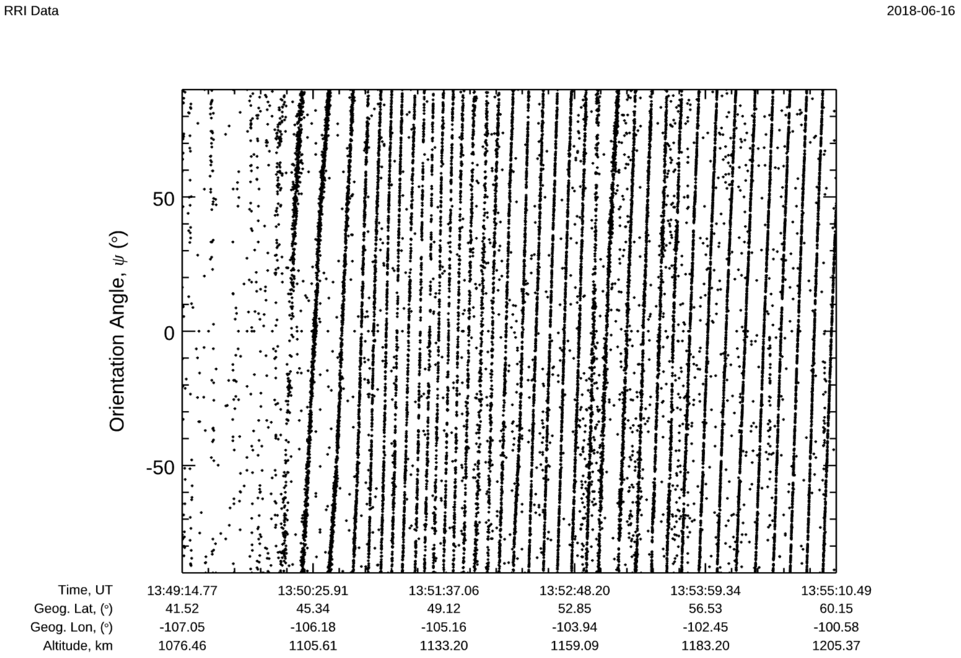

Figure 5.8: Line plot of orientation angle ψ from the slewing RRI-SuperDARN Saskatoon flyby on 16 June 2018.

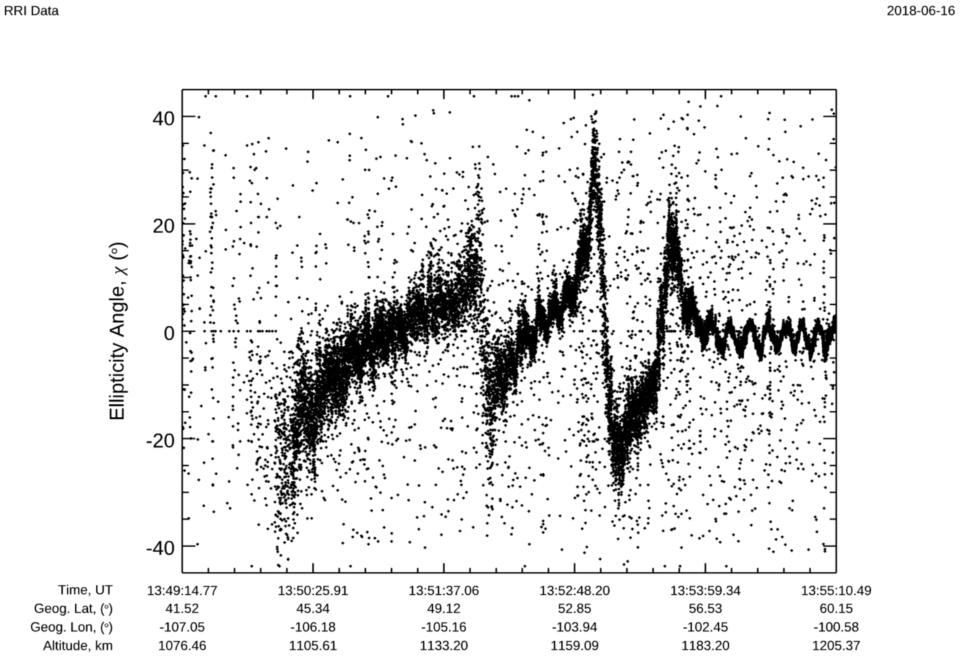

Figure 5.9: Line plot of ellipticity angle χ from the slewing RRI-SuperDARN Saskatoon flyby on 16 June 2018.

Finally, from the ephemeris data of the ePOP flyby, a selection of geometry based line plots were calculated to give context into the conditions of the flyby. Figure 5.10 presents a line plot of the angle between the LOS k-vector and the ePOP ram direction (the direction of the motion of the satellite), arbitrarily called Δ. This plot has the main advantage of determining the point of closest approach between the ePOP flyby and the Saskatoon SuperDARN radar. Geometrically this point must occur when the angle reaches perpendicularity ($\Delta = 90^\circ$). In Figure 5.10, the point of closest approach (where $\Delta = 90^\circ$) is shown to be at the 13:52:26 UT mark. In Figure 5.11 a line plot is presented of the angle between the LOS k-vector and the local B field, or the aspect angle θ. This is a quantity that is referenced frequently in the theory and is particularly relevant with the QL and QT approximations and the Faraday rotation equation. In Figure 5.11, the aspect angle at the very beginning of the flyby is very near anti-parallel and so within the QL approximation, but does not exactly reach 180°. In fact, for all the ePOP flybys over Saskatoon, the aspect angle has never reached exactly parallel or exactly perpendicular through the entire pass and will reverse before reaching the extremes, just as shown in Figure 5.11. From the many RRI flybys analyzed, this was always the case and it is expected that it is not possible for the aspect angle to even reach these extremes while passing over Saskatoon. Although not in the scope of this thesis, this could be determined through modelling.

The final geometric plot calculated from the ePOP ephemeris data is the angle ϕ, which is the angle between the LOS k-vector and the RRI normal. This is one of the most important plots needed for interpreting the RRI observation, since it is used to determine if a flyby is slewing or not. As mentioned previously, slewing ePOP so that the RRI normal is always

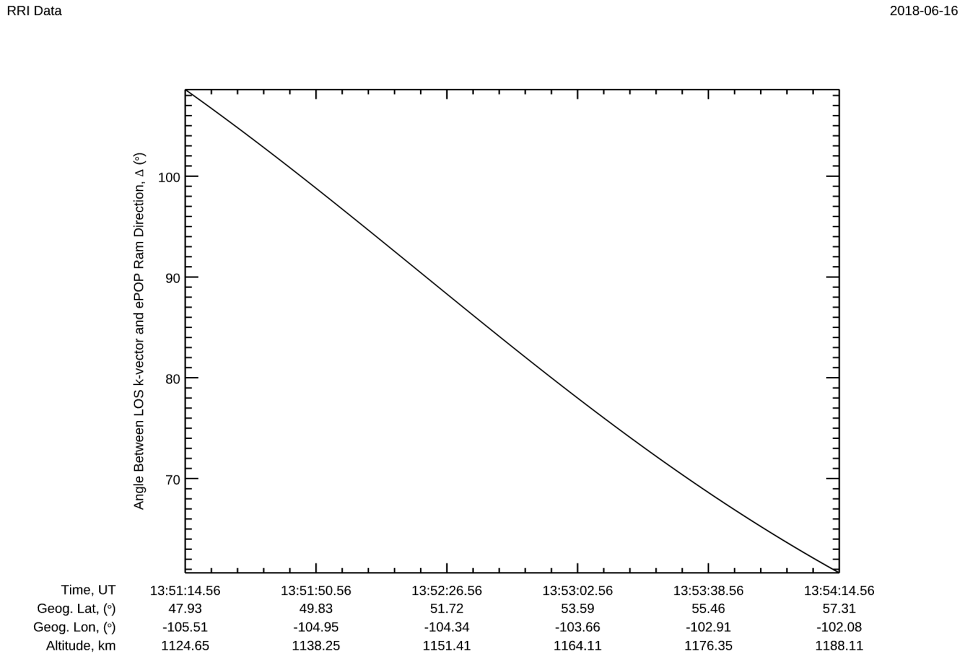

Figure 5.10: Line plot of angle Δ between the LOS k-vector and the ePOP ram direction from the slewing RRI-SuperDARN Saskatoon flyby on 16 June 2018.

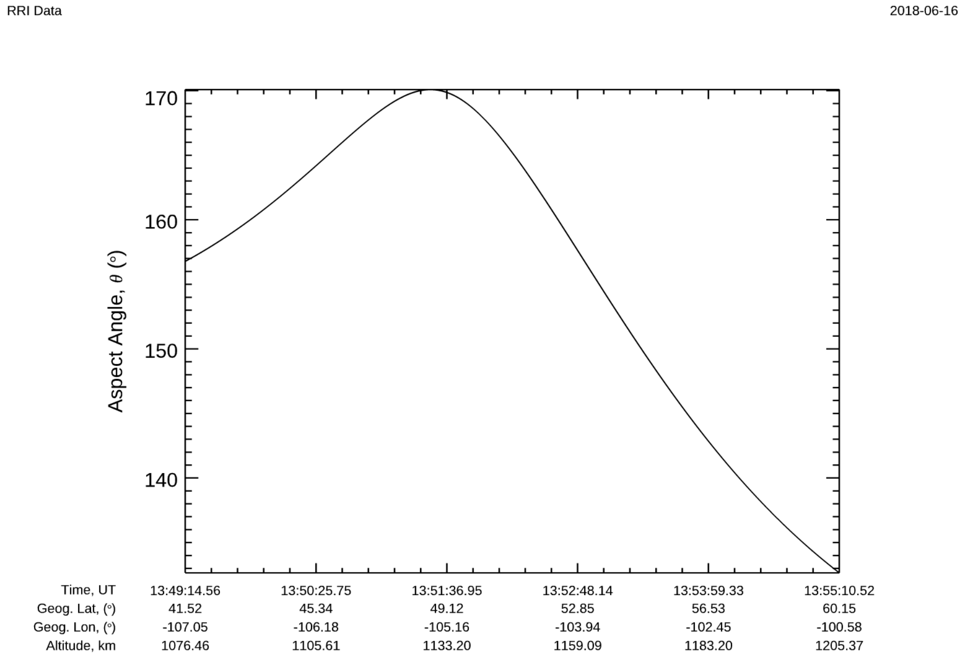

Figure 5.11: Line plot of aspect angle θ from the slewing RRI-SuperDARN Saskatoon flyby on 16 June 2018.

pointing towards Saskatoon would be most the optimal observational requirement, but this is not an orientation that works favourably for other ePOP instruments, which have their own preferred optimal pointing direction. For instance, if the FAI camera is running it needs to be pointed directly down towards the Earth in a nadir orientation. When the spacecraft is in an orientation such that FAI is pointed in the nadir direction, this often means the RRI is pointed roughly in the same direction as the ePOP ram direction (and therefore not slewing to the Saskatoon SuperDARN radar). Another instance which can sometimes cause a slewing flyby to not occur is if the satellite is at too low an altitude during the flyby. At a lower altitude the spacecraft would require a greater rotation rate than is possible from the ACS. This means that lower altitude flybys are typically never slewing. This configuration will be referred to as simply nadir flybys from here on. Fortunately, a nadir orientation on an ascending flyby can still yield usable data, which will be demonstrated in the next section. In Figure 5.12, since the angle ϕ remains within 25° of the anti-parallel direction, the RRI was roughly pointed towards the Saskatoon SuperDARN radar over the course of the flyby, so it was a slewing flyby.

As mentioned, the Kp-index at the time of this flyby on 16 June 2018 was at 0+. This is one of the factors used to determine the condition of the ionosphere at the time of the flyby. The other is ionosonde data and values of hmF2 and foF2 can be determined from this data. Figure 5.13 shows the CADI ionogram plots over a 2-hour period from Resolute Bay at the time of the above flyby. From these plots an estimate of F2 parameters can be formed giving hmF2 = 225 km and foF2 = 4 MHz. Since there are no operational ionosondes at or even close to Saskatoon during the ePOP flybys, these distant ionosondes are the only available options. Therefore, precise measurements of these values are not necessary since they only portray the general state of the ionosphere.

Finally, the last plot (Figure 5.14) that will be presented for this 16 June 2018 flyby is a ray tracing model produced by R. Gillies (Gillies et al., 2012). Figure 5.14 shows three line plots versus latitude for the Faraday rotation, the orientation angle and the ellipticity angle. From the top plot, one can see a Faraday rotation that is gradually slowing down with increasing latitude. This agrees with what is observed in the data for this flyby. Note that the rotation is in the opposite direction in the model from the observed result; this is caused by a change in reference frame (the model calculates the perspective of the radar and the RRI measures from the perspective anti-parallel to the k-vector). However, when comparing the ellipticity angle between the observations and modelled results, the latter shows very little Voigt effect oscillation (observed occasionally in some calculations but still nowhere near the same magnitude), and certainly does not exhibit the signature spikes seen in the observations. There is a small amount of biasing that can be observed in the ellipticity angle (i.e. not centred on $\chi = 0°$) from some of the modelled results. This is interesting because the typical cause for this would be collisions and absorption, but these factors were not considered for the calculations in the model. Meaning that some other beam bending effect would likely be the cause of biasing in the ellipticity angle.

5.3 Features of Non-Slewing Flybys

Although not ideal for my research, sometimes a slewing flyby is not available and instead one must to work out as much detail as possible from a non-ideal ePOP attitude orientation. For example, some usable data can be attained from nadir flybys, however there are some

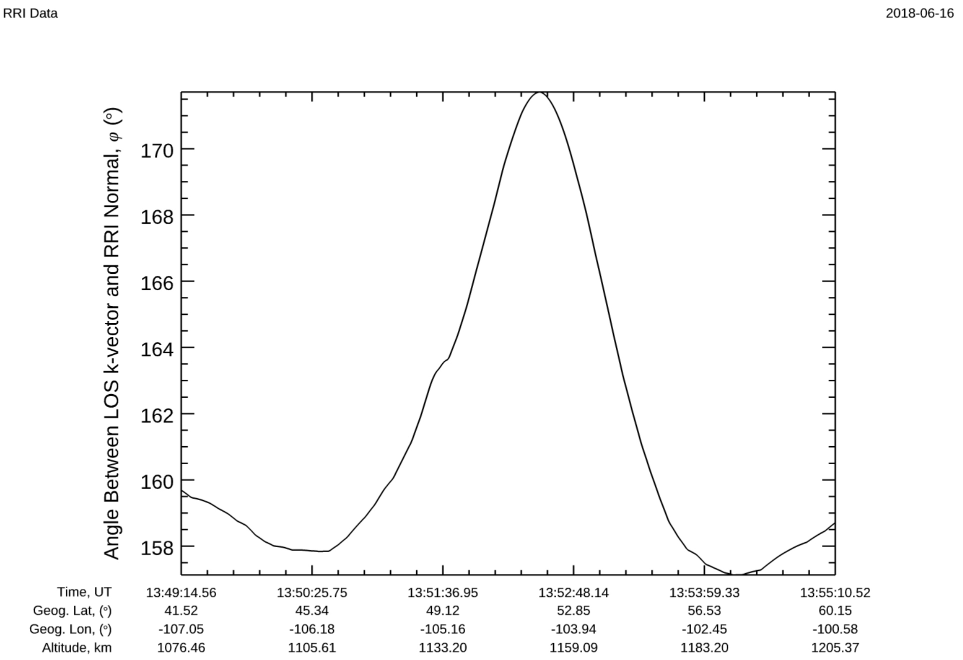

Figure 5.12: Line plot of angle ϕ between the LOS k-vector and RRI normal from the slewing RRI-SuperDARN Saskatoon flyby on 16 June 2018.

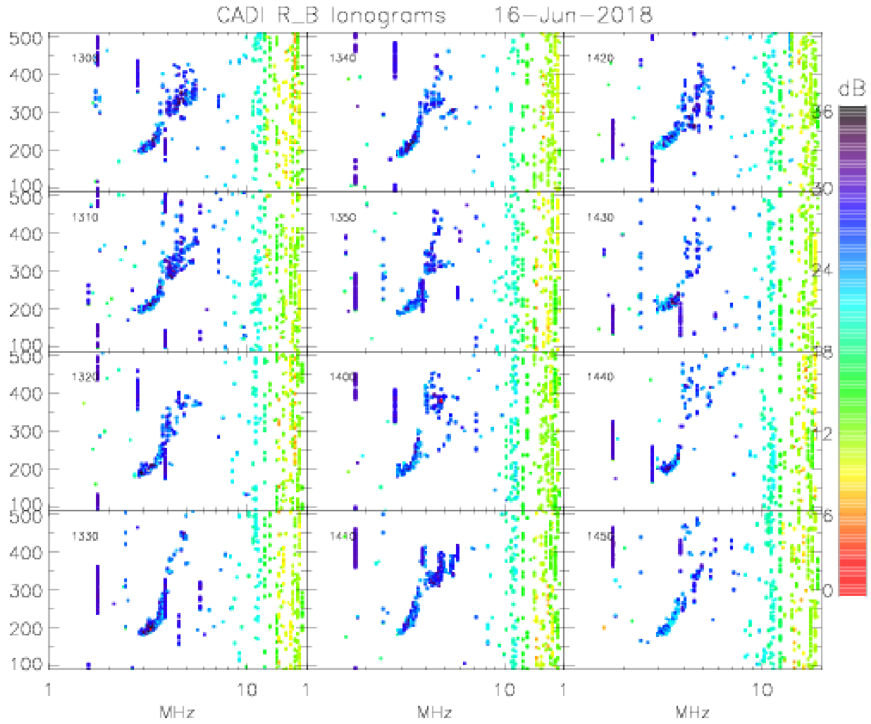

Figure 5.13: Ionogram from Resolute Bay on 16 June 2018 at the same time as the ePOP Saskatoon flyby.

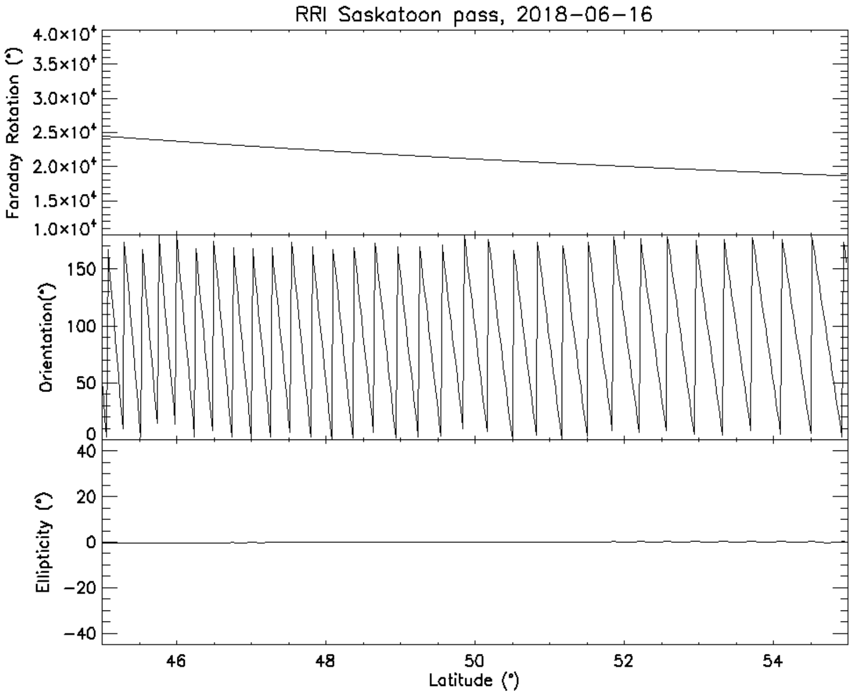

Figure 5.14: Simulation using the model of Gillies et al., 2012 for 16 June 2018 [Courtesy: Rob Gillies].

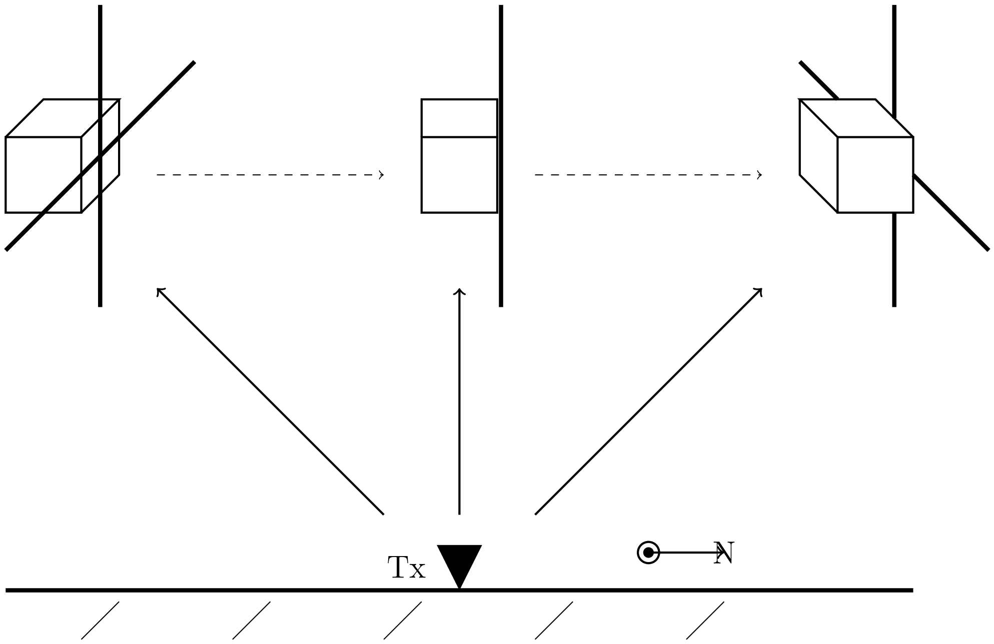

Figure 5.15: An exaggerated depiction of an ascending RRI flyby while in a "nadir" orientation, viewed from the eastward direction.

distinct features due to the non-ideal geometry from these flybys that limit how much can be observed. In a nadir flyby, the RRI normal direction is along the ram direction of the ePOP satellite. An exaggerated depiction of a nadir flyby conjunction with the Saskatoon SuperDARN radar is presented in Figure 5.15. In this figure, the radar is represented by "Tx" and the satellite is traveling northward (to the right). Therefore, it is known that the ram direction of ePOP will be $\sim 90°$ at the point of closest approach with respect to the Saskatoon SuperDARN radar; then also at this point $\phi = 90°$. When the angle is between the LOS k-vector and RRI normal 90°, RRI is no longer acting as a cross dipole layout and is instead acting as only a single dipole (the middle position in Figure 5.15). The RRI data loses significant polarization information in this case and the calculated results can no longer be considered physical. This orientation effectively means that the observed polarization ellipse is warped by the orientation of RRI to be significantly narrower in one direction and eventually one-dimensional at the point where the RRI normal direction and k-vector are perpendicular ($\phi = 90°$). The following lines plots of ϕ (Figure 5.16), orientation angle (Figure 5.17) and ellipticity angle (Figure 5.18) of a nadir flyby on 23 September 2018 demonstrate the loss of physical information. What is presented in Figure 5.16 is that the angle ϕ passes through 90° exactly as it passes closest to the Saskatoon SuperDARN radar (at ~00:51:32 UT). So, at this point of closest approach, we need to look at the effects on the orientation angle and ellipticity angle of the flyby. In Figure 5.17, the orientation angle clearly shows a Faraday rotation reversal event at the 00:53:38 UT mark. However, as we look at the orientation angle data to the left of this, the data is noise-like at closest approach to the Saskatoon SuperDARN radar at the 00:51:32 UT mark; however, we would expect Faraday rotation to still be continually changing at this point. Since the ellipticity angle is much more reliant on the orientation of RRI, this data is even noisier than the orientation angle data. Again at the 00:51:32 UT mark over the Saskatoon SuperDARN radar (Figure 5.18) the attitude of RRI in the nadir mode is such that the ellipticity angle is purely linear and the observations around this point appear noise-like due to the sensitivity to the geometry in this configuration.

For another example of a nadir flyby we look to the flyby on 24 September 2018 shown in Figures 5.19 and 5.20. Here ePOP passes by the point of closest approach just before the 00:25:49 UT mark. In Figure 5.19, as ePOP passes by the Saskatoon SuperDARN radar at this point, the orientation angle plot shows what may look like a Faraday rotation reversal event. However, this is merely an artifact of the angle of the incoming k-vector switching from one side of RRI to the other. This is an example of a normal looking data set, in the non-ideal nadir orientation, where the Faraday rotation can be observed, but the Faraday rotation reversal event is purely geometric. Continuing with Figure 5.19, for observation significantly northward of the Saskatoon SuperDARN radar, past about 56° latitude, the Faraday rotation behaviour returns to a regular format, including even a Faraday rotation reversal event at the 00:29:39 UT mark. Now looking at Figure 5.20, as we again look at the point of closest approach (00:25:49 UT mark), the ellipticity angle no longer demonstrates an oscillation associated with the Voigt effect but instead separates into individual vertical curves. Remember that the ellipticity angle and the Voigt effect are the most affected by this non-ideal RRI orientation and that these features shown here are non-physical and are artifacts of RRI pointed approximately perpendicular to the incoming k-vector.

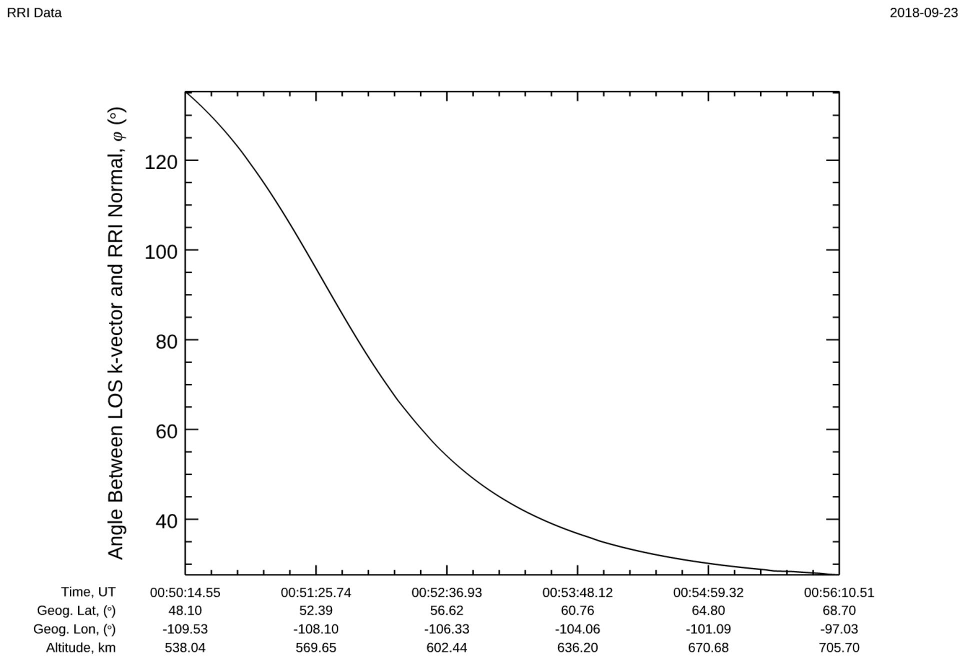

Figure 5.16: Line plot of angle between the LOS k-vector and RRI normal from the nadir RRI-SuperDARN Saskatoon flyby on 23 September 2018.

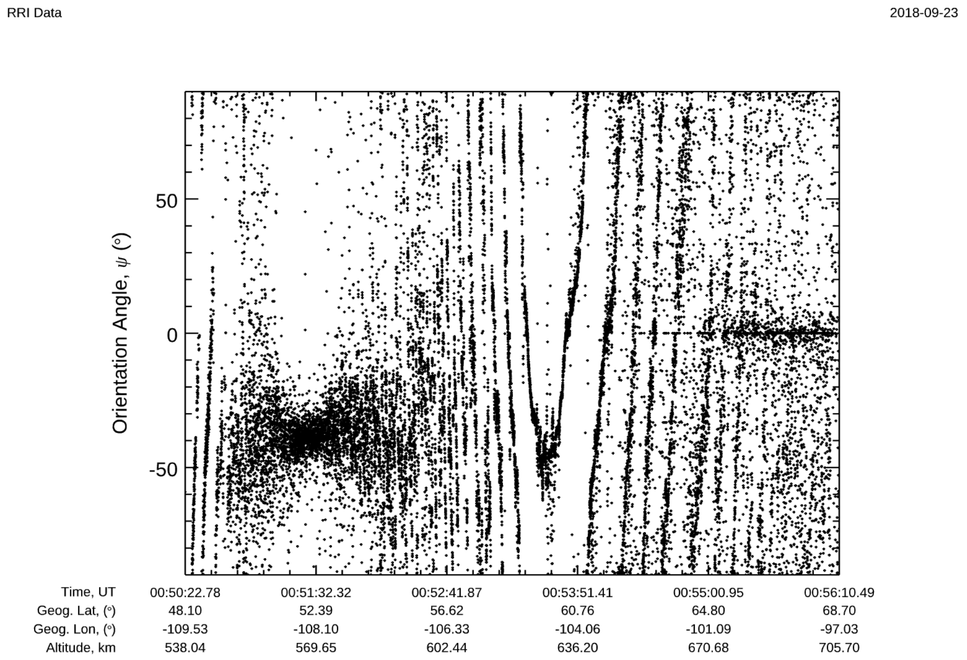

Figure 5.17: Line plot of orientation angle ψ from the nadir RRI-SuperDARN Saskatoon flyby on 23 September 2018.

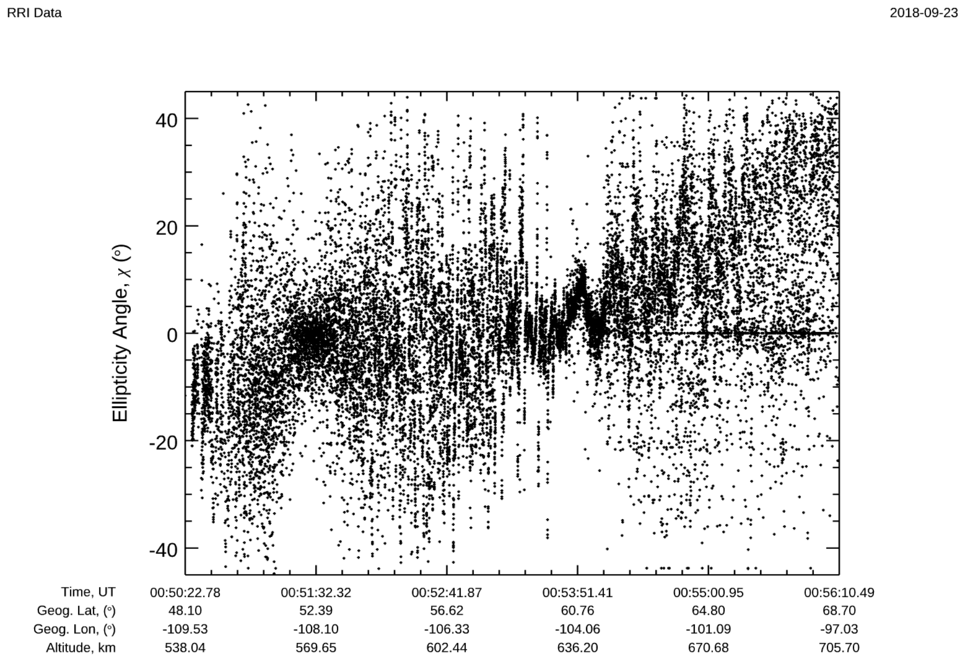

Figure 5.18: Line plot of ellipticity angle χ from the nadir RRI-SuperDARN Saskatoon flyby on 23 September 2018.

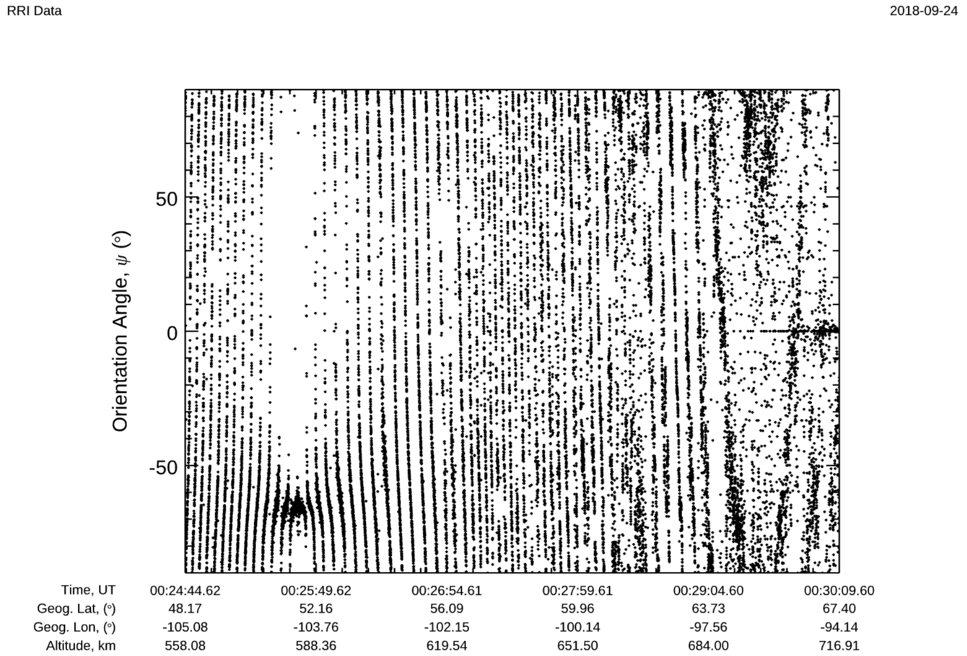

Figure 5.19: Line plot of orientation angle ψ from the nadir RRI-SuperDARN Saskatoon flyby on 24 September 2018.

Nadir flybys put RRI in an orientation that is non-ideal for polarization information, since the RRI normal direction is pointed essentially perpendicular to the k-vector at the point of closest approach. This means that polarization data in the vicinity of the Saskatoon SuperDARN radar is usually unusable ("artificial") data for a nadir flyby. However, the data further away will eventually demonstrate usable observations as the angle ϕ between the LOS k-vector and RRI normal moves significantly away from perpendicularity. In practice, for Saskatoon SuperDARN radar observations, this typically means that data north of about 56° latitude is usable, while observations closer to Saskatoon is typically unusable.

5.4 Faraday Rotation observations

The Faraday rotation effect is the most consistently observed phenomenon in the RRI-SuperDARN experiment. In a flyby, even if the data from the ellipticity angle does not show any considerable Voigt effect, the Faraday rotation effect will still be clearly identifiable. In general, as long as there is no significant O- and X-mode separation and SNR is high enough, then Faraday rotation will be observed. To cover what can be observed by Faraday rotation, two particular phenomena that are observed by RRI from the Saskatoon SuperDARN radar via Faraday rotation will be discussed: 1) a case study of a unique change in the rate of Faraday rotation, and 2) the Faraday rotation reversal event that was first reported by Danskin et al. (2018).

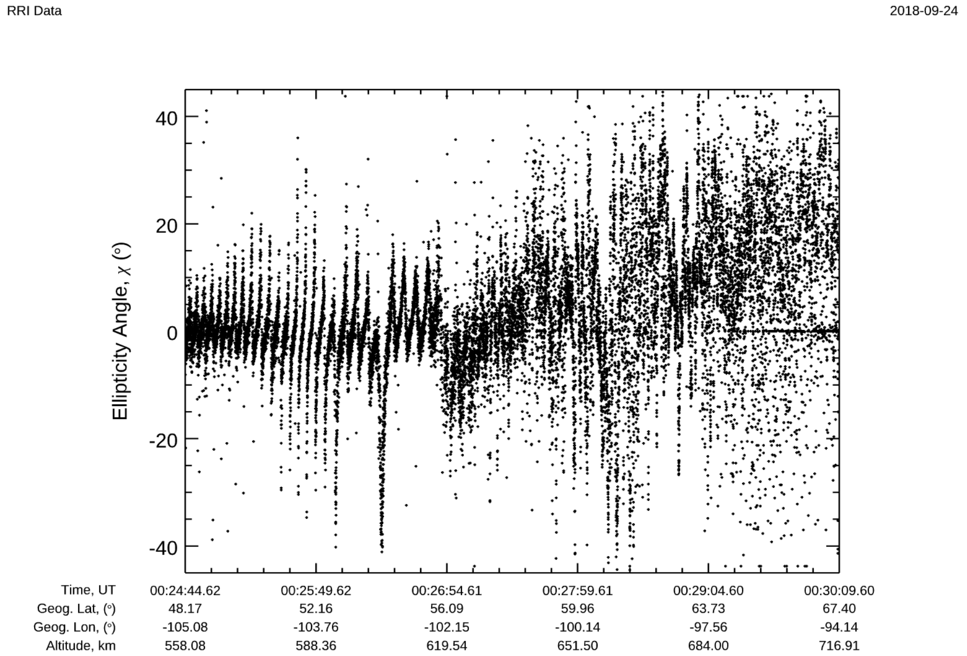

Figure 5.20: Line plot of ellipticity angle χ from the nadir RRI-SuperDARN Saskatoon flyby on 24 September 2018.

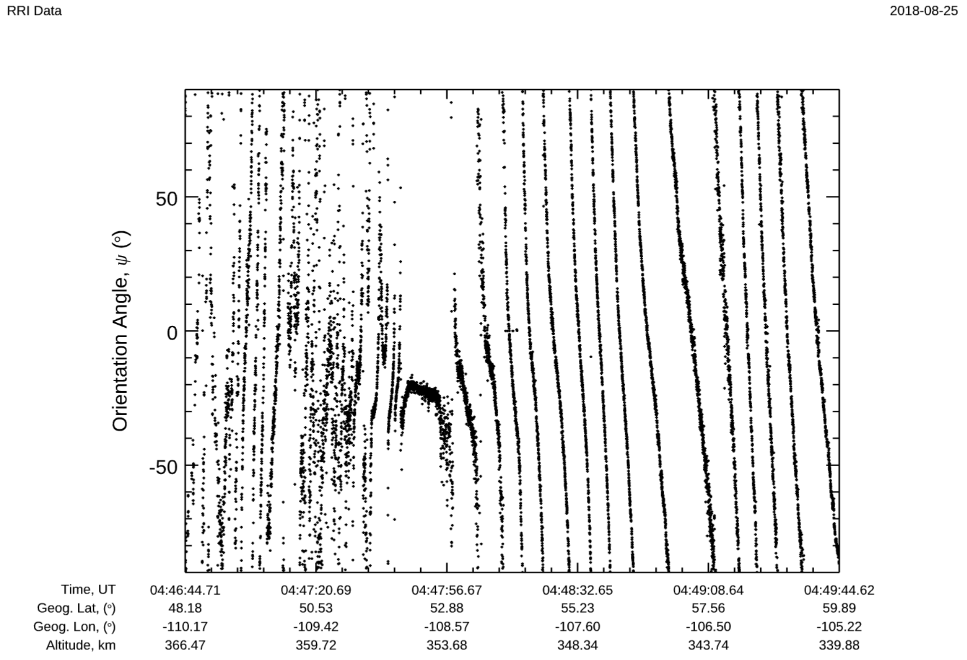

Figure 5.21: Line plot of orientation angle ψ from the nadir RRI-SuperDARN Saskatoon flyby on 25 August 2018.

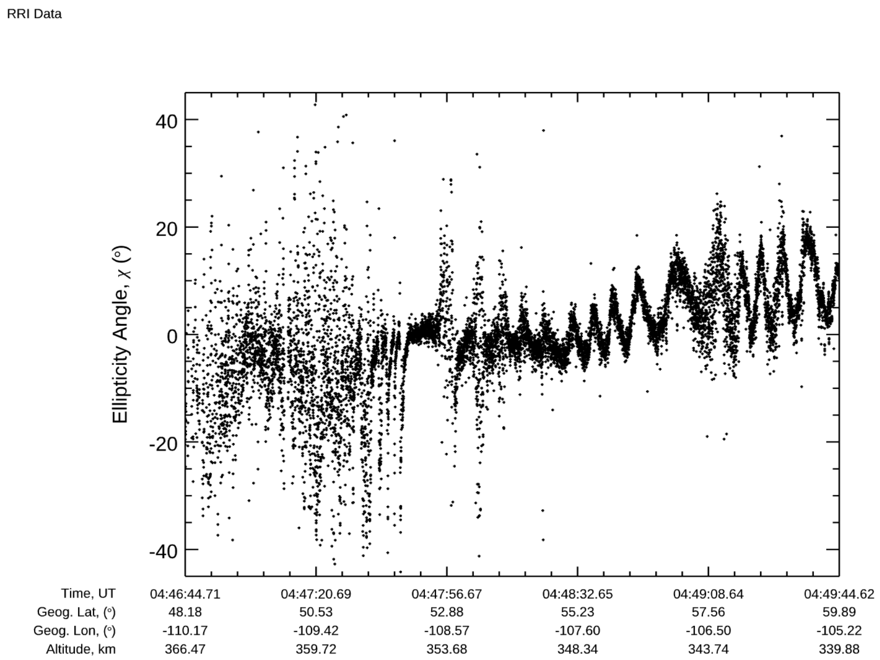

Figure 5.22: Line plot of ellipticity angle χ from the nadir RRI-SuperDARN Saskatoon flyby on 25 August 2018.

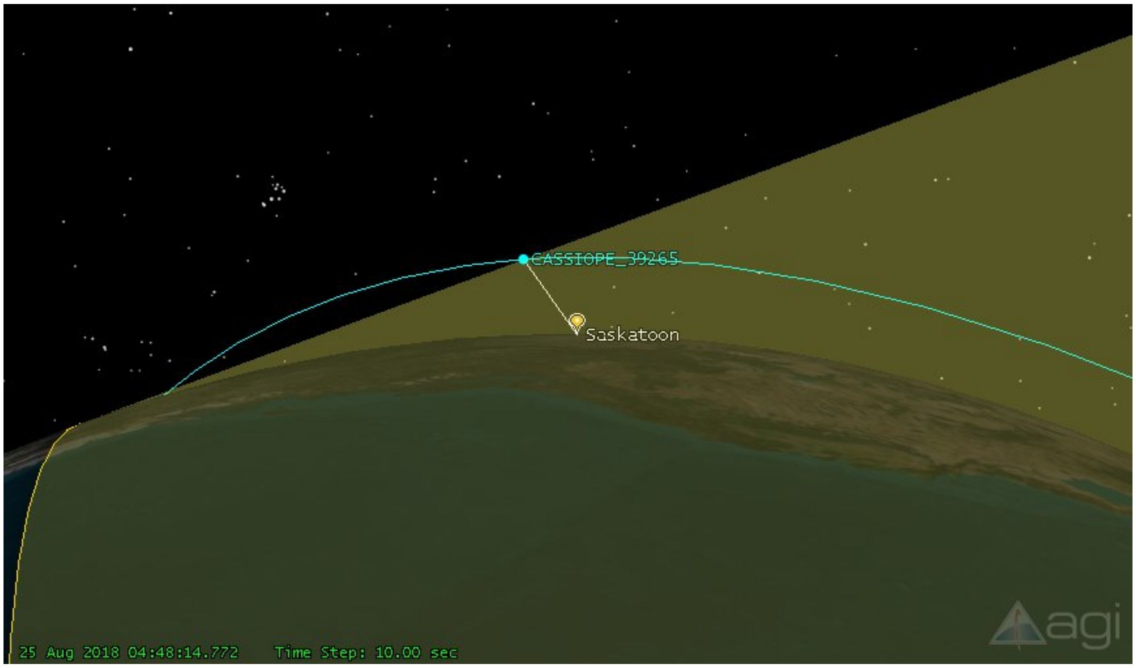

Figure 5.23: STK view of the RRI-SuperDARN Saskatoon flyby on 25 August 2018 as seen from a point in space west of the flyby. [Courtesy: University of Calgary ePOP team]

5.4.1 Special Case Study of Unique Change in Rate of Faraday Rotation

Figures 5.21 and 5.22 are the orientation angle and ellipticity angle from a 90 second period of a flyby from 25 August 2018. This is a nadir flyby as can be identified by the distortion in orientation angle at the 4:47:44 UT mark, which causes an artificial reversal event. There is a real reversal event that takes place at about the 4:50:08 UT mark (just past the plotted data in Figures 5.21 and 5.22). However, the part of this flyby to focus on is the point centred at about the 4:49:08 UT mark. What is seen in the orientation angle is that there is some rate of change in Faraday rotation before this point, then at this point the Faraday rotation slows down considerably, but soon after the Faraday rotation speeds up again to a rate similar to before. Remember that the observed apparent rotation of the orientation angle is really the rate of change of total resultant Faraday rotation. In this short period of slower Faraday rotation, the rate of change of a dependent variable was momentarily different. If we take a look a the Faraday rotation Equation 3.13, repeated again here,

$$\phi_F = \frac{e^3 \mu_0 c}{2{m_e}^2 \omega^2} \int B \cos\theta N_e d\ell,$$

there are really only 2 variable terms in the equation, the magnetic field term $B\cos\theta$ and the TEC term $N_e d\ell$. Of these two terms, only one could have an irregularly shifted rate of change since the magnetic field of the Earth must remain essentially consistent. This means that during this flyby the TEC term had some steady rate of change, then suddenly shifted to another rate of change, and finally returned back to the original rate of change. Using Systems Tool Kit (STK) it was determined that this sudden slow down in Faraday rotation rate of change point coincides with the moment that ePOP travels through the terminator from nighttime to daytime. A pictorial representation of this is presented in Figure 5.23 as seen from a point in space west of the RRI-ePOP spacecraft, with the trajectory of ePOP in blue and a yellow projection of the terminator. The flyby is an ascending flyby, therefore ePOP travels from the right side of this image (south) to the left side (north). The point at which ePOP is located is the exact time (4:49:08 UT) at which the change in Faraday rotation rate occurs. And as presented in the figure, it is also the time at which ePOP is transitioning from nighttime to daytime. For this short period in the flyby there is a significant increasing rate of change of electron density N_e as opposed to the typical slow decrease as ePOP travels northward under constant sunlight (or darkness) conditions.

5.4.2 Faraday Rotation Reversal Event

As was reported by Danskin et al. (2018), the Faraday reversal event is a regular occurrence in RRI flybys explained by variations in TEC and the magnetic field of the Earth along the propagation direction. As presented in the paper, the Faraday reversal event appears in a similar location from flyby to flyby and gradually moves depending on the groundtrack of the flyby.

Unfortunately, this appears not to be the case for Saskatoon RRI-SuperDARN flybys. This is very likely due to the fact that the Ottawa flybys were well southward of the auroral zone, where conditions of the ionosphere are more predictable and less variable. As opposed to Saskatoon flybys which are at least half in the much more variable auroral zone. The usable flybys over Saskatoon were almost never able to produce consistent results similar to the

Ottawa flybys, even when sequential flybys as were attempted. Most attempts to replicate the Ottawa sequence of flybys were compromised by half the flybys returning unusable data, or sometimes inconsistent Faraday rotation reversal event locations. For instance, Figure 5.24 is the orientation angle line plot from the entire flyby on 4 October 2018. As ePOP flies further north in the flyby, it can be seen that the Faraday rotation rate is slowing down considerably and approaching a Faraday rotation reversal event. However, the flyby data collection stops just before a reversal event was about to occur. This means that even though we see an event about to take place, since it is not directly observed the data cannot be used as the reversal event takes place north of the end point of the flyby. The Faraday rotation reversal event from this flyby on 4 October 2018 is also one of the most northward reaching flybys ever (almost) recorded. If there are occasions where a flyby such as this cannot observe the Faraday rotation reversal event, then one could see how there are many other flybys which also do not observe the Faraday rotation reversal event for the same reason. The Faraday rotation reversal event can take place as far north 68° latitude, as shown in Figure 5.24, but can also occur as far south as 56° latitude.

Even though flybys will show evidence that a Faraday rotation reversal event would take place, there are a few factors that mean the event is not always directly observed in usable flybys. This combined with the ratio of usable flybys recorded to attempted conjunctions means a relatively low occurrence of observed Faraday rotation reversal event for the RRI-Saskatoon SuperDARN. In 2018, out of the 16 usable recorded flybys, only 6 flybys observed the Faraday rotation reversal event. It should be noted that even within these recorded events there is some uncertainty. For instance, the orientation angle line plot of the flyby

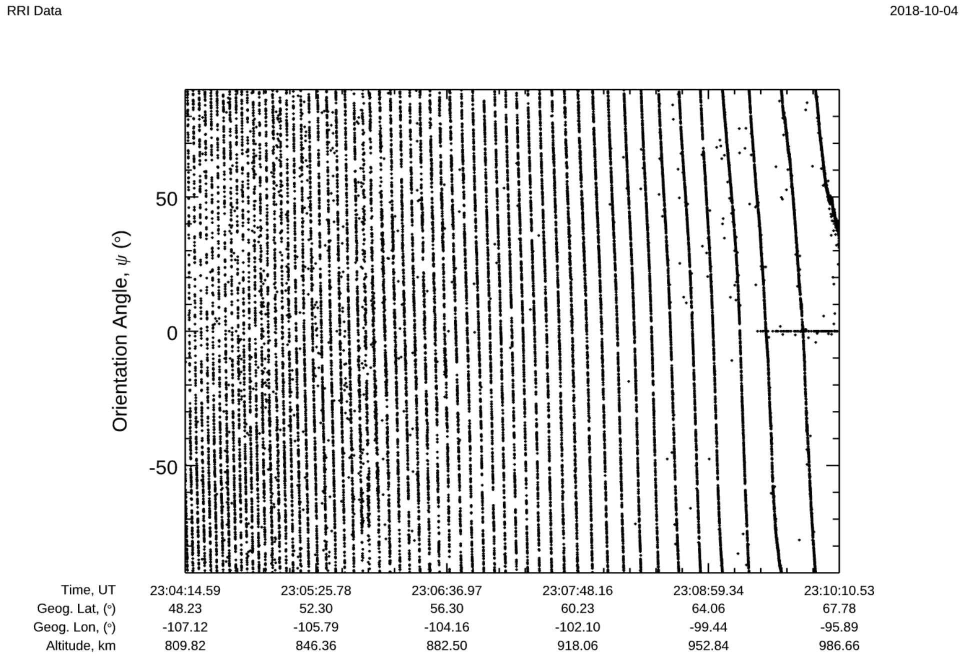

Figure 5.24: Line plot of orientation angle ψ from the slewing RRI-SuperDARN Saskatoon flyby on 4 October 2018.

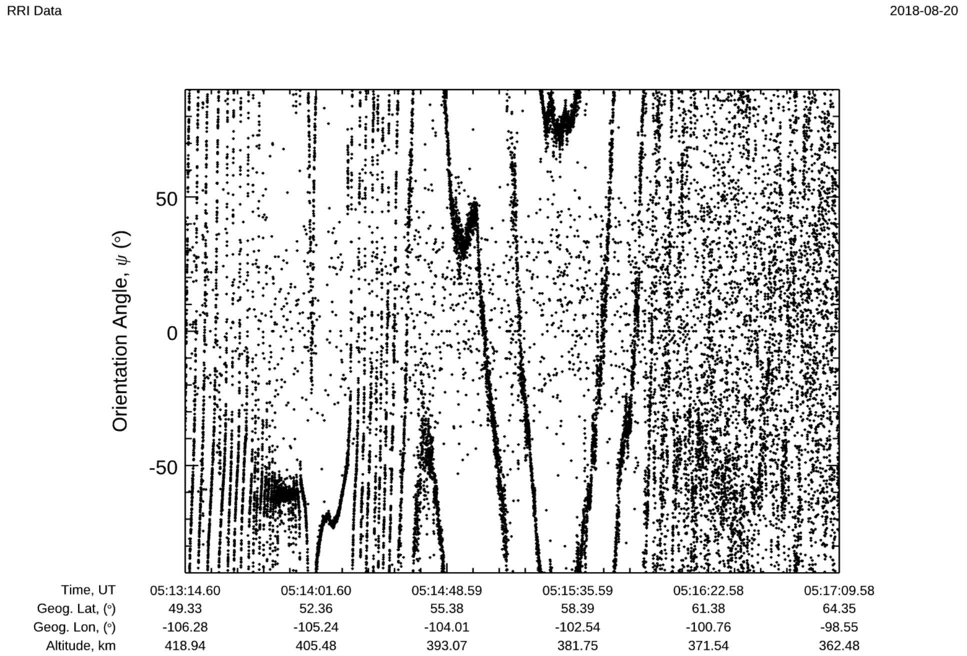

Figure 5.25: Line plot of orientation angle ψ from the nadir RRI-SuperDARN Saskatoon flyby on 20 August 2018.

on 20 August 2018 is shown in Figure 5.25. There is an observed Faraday rotation reversal event at the 05:15:30 UT mark. The ionospheric conditions at the time were Kp-index = 3+, and from the Cambridge Bay ionosonde hmF2 = 400 km and foF2 = 2 MHz. At the time of the observed Faraday rotation reversal event, ePOP ephemeris indicated an altitude of about 380 km. In this case, the altitude of the spacecraft is lower than the measured hmF2 value from the Cambridge Bay ionosonde. Taking the Cambridge Bay ionosonde as a reasonable representation of the ionosphere at the time and place of the Faraday rotation reversal event (hmF2 will slightly increase for decreasing altitude (Qian et al., 2013)), that would mean that a part of this flyby was below the F2 peak in the ionosphere (or at least at the same altitude the F2 peak). Since a majority of the Faraday rotation takes place near the F2 peak, this gives unknown discrepancies, if any, for an observation that is made while ePOP is below the F2 peak. Observed in Figure 5.25 is a much longer region of significantly slowed down Faraday rotation rate compared to other Saskatoon flybys. However, it is difficult to draw conclusions from this since we do not know the exact point RRI moves into or out of the F2 peak.

Regarding the rest of the usable flybys, there are some particular instances that do compare to observations made by the Danskin et al. (2018) paper. There is a set of two sequential flybys which both observe Faraday rotation reversal events. The flybys on 23 and 24 September 2018 each observe a Faraday rotation reversal event at coordinates 59.93°N, −104.51°E and 65.44°N, −95.94°E respectively. Each flyby is under comparable ionospheric conditions (Kp-index = 3+, hmF2 = 325 km, and foF2 = 2 MHz for 23 September 2018; Kp-index = 2+, hmF2 = 350 km, and foF2 = 2 MHz for 24 September 2018) and take place at the same time of day (around 00:45 UT). Danskin et al. (2018) observed that as the ground track of the flyby moves eastward, the point of Faraday rotation reversal moved northward when under similar ionospheric conditions. This is exactly the same condition observed in the flybys on 23 and 24 September 2018; the point of Faraday rotation reversal on the 24 September flyby is northeast of the 23 September point of reversal. On this, the data from the Saskatoon flybys and the Ottawa flybys agree.

Another observation made by Danskin et al. (2018) was about an outlier flyby on 20 April 2016. The Faraday rotation reversal event observed in this flyby was more northward than expected and did not line up with the smooth curve of reversal points made by the 4 other flybys. Looking at recorded ionospheric conditions, the main discrepancy on this flyby was a moderately lower foF2 value (5.381 Mhz compared to the average of 6.202 MHz from the other flybys). However, in the Saskatoon flybys, it is typically observed that a flyby with a lower foF2 value is more southward than higher foF2 values, an opposite observation compared to the Ottawa flybys. For instance, a flyby on 17 September 2018 recorded a Faraday reversal event at 64.46°N, −103.34°E under ionospheric conditions Kp-index = 3+, hmF2 = 300 km, and foF2 = 3 MHz (higher than the 2 MHz of 23 and 24 September flybys). However, when this flyby is compared to the 23 and 24 September flybys just a week later, the point of Faraday rotation reversal is more northward than expected. This is also observed with nighttime flybys, that they will typically have lower TEC and will also typically have more southward reversal points.

Faraday rotation and the observed phenomena from Faraday rotation from the RRI-SuperDARN flybys were presented in this section. A unique case took place on 25 August

2018 flyby when RRI crossed the terminator and observed a significant change in the rate of Faraday rotation. This change in the rate of Faraday rotation was demonstrated to coincide with the corresponding increase in F-region plasma density that would be expected when transitioning from darkness into daylight. When attempting to replicate the Faraday rotation reversal event observations from the Ottawa flybys (reported in Danskin et al. (2018)), Saskatoon flybys did not demonstrate the same consistency. The difference in observations could be because flybys in conjunction with the Saskatoon SuperDARN radar were mostly in the auroral zone (the observed Faraday rotation reversal events were always in the auroral zone) which is a significantly more variable region; the Ottawa flybys were all south of the auroral zone, where the ionosphere is more predictable.

5.5 Voigt Effect and Ellipticity Angle Behaviour

The Voigt effect is a phenomenon that has not been well documented in space physics. In categorizing all observed features associated with the ellipticity angle in ePOP flybys over Saskatoon, one can further understanding of transionospheric radio wave propagation. One immediate issue was encountered with significantly categorizing a set of observed ellipticity angle features, namely that the Voigt effect (oscillations in ellipticity angle) is inconsistently observed. The Voigt effect is not always distinctly observed even in data flybys where Faraday rotation is present. This includes nadir flybys where often times the most interesting major features in ellipticity angle are distorted by the distortions at the point of closest approach. And even with the Voigt effect observed, some of the major features observed are only observed a portion of times. Nonetheless, this section will cover two prevalent features drawn from the ellipticity angle in RRI data over the Saskatoon SuperDARN radar.

To interpret elliptically angle observations, recall the Voigt effect approximation equation. From the theory, the Voigt effect equation for ellipticity angle (Equation 3.16), repeated here is

$$\sin 2\chi = -\sin 2\psi_0 \sin \delta.$$

This equation shows that the ellipticity angle is dependent on the orientation angle. Therefore, if the orientation angle is changing in a particular pattern, then the ellipticity angle would also be exhibiting some similarities to that same pattern. The orientation angle does indeed exhibit a pattern as it rotates due to Faraday rotation, and from the Faraday rotation pattern the ellipticity angle will oscillate as well. This was presented in Figures 5.21 and 5.22. As the rate of Faraday rotation in the 25 August 2018 flyby changes, so too does the rate of Voigt effect oscillations. This orientation angle dependent oscillation is observed in all observations of the Voigt effect including observations made by Danskin et al. (2018). This is clearly observed in the Faraday rotation reversal events as when the rate of change in the Faraday rotation is the lowest, the rate of oscillation in the Voigt effect is also the lowest. The size of oscillations in the ellipticity angle is shown in the data to be about ±5.7°, which is also expected from the theory of the Voigt effect (Section 3.3.2)

A final example of the Voigt effect is presented in Figure 5.26 in the flyby on 4 October 2018. Shown in Figure 5.26 is the ellipticity angle for this slewing flyby. The north part of the flyby shows a smooth Voigt effect oscillation which is gradually slowing down, corresponding to the Faraday rotation also slowing down which is expected. However, there are 3 distinct spikes in the ellipticity angle at the southern part of the flyby. As this flyby is slewing, the

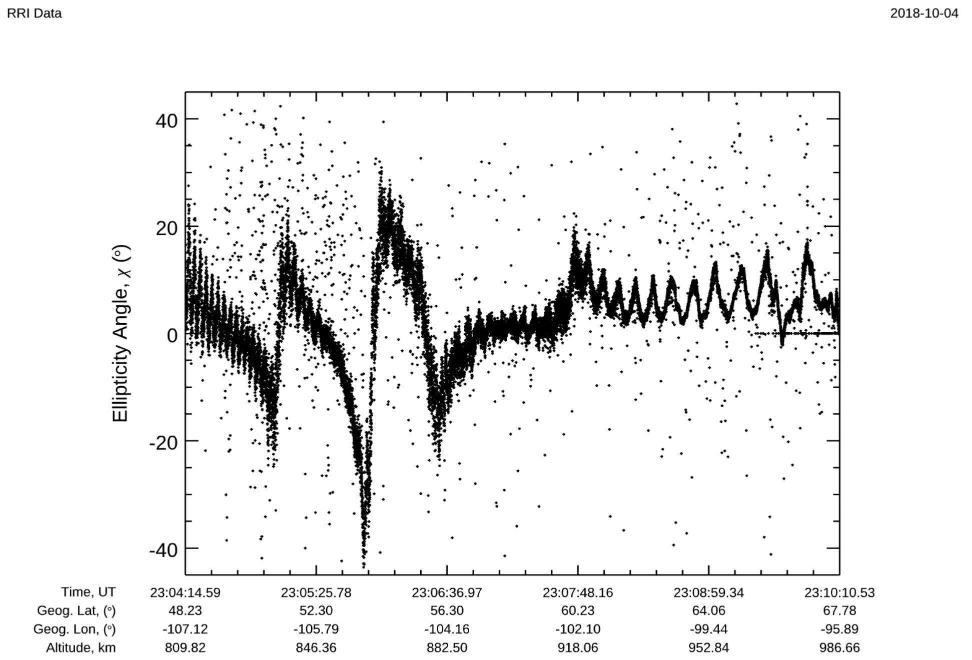

Figure 5.26: Line plot of ellipticity angle χ from the slewing RRI-SuperDARN Saskatoon flyby on 4 October 2018.

spikes in the ellipticity angle are not artificially created by the spacecraft (as for example in a nadir flyby). The 3 spikes centred around Saskatoon are also observed in the 16 June 2018 flyby shown in Figure 5.9. This flyby is also slewing and the distinct spikes are roughly the same positions. There is no similar signature pattern in the orientation angle in which the spikes could be originating from in either the 16 June 2018 flyby or the 4 October 2018 flyby.

In contrast, Figure 5.20 shows the ellipticity angle from the 24 September 2018 flyby (a nadir flyby), which does not show these same 3 spikes in ellipticity angle. The 5 flybys in 2018 that observe these spikes have a few similarities. They are all slewing daytime flybys at times of low Kp-index (< 2) and are orbiting at a higher altitude (>800 km). These flybys do not all take place at the same time of the year, 4 of the flybys are in June (16, 21, 22, 28 June 2018) and 1 is in October (4 October 2018). Three of the flybys pass East of the

Saskatoon SuperDARN radar (16, 22, 28 June 2018), 1 flyby passes west of the Saskatoon SuperDARN radar (21 June 2018), and 1 flyby passes over top of the Saskatoon SuperDARN radar (4 October 2018). Flybys that do not demonstrate these spikes in ellipticity angle are almost all low altitude, nadir flybys, suggesting that the significant loss of polarization information from the attitude of the spacecraft at the point of closest approach is enough to impede observations of the spikes. However, the flyby on 1 February 2018 is an example of a slewing high-altitude flyby which does not demonstrate the spikes in ellipticity angle. The only difference between this flyby and the other 5 flybys which do demonstrate the spikes is that the flyby on 1 February 2018 occurs at nighttime as opposed to daytime, suggesting that this phenomenon could be dependent on the larger TEC values associated with the daytime ionosphere.

The spikes in ellipticity angle have a few repeating physical details. The first 2 spikes are always centred around the point of closest approach in the flyby (if the first spike was $\sim$200 km south of the point of closest approach the second spike was $\sim$200 km north of the point of closest approach). The distance of these 2 spikes are in the range of 200 km to 250 km north/south of the point of closest approach. The first two spikes are sharp and would appear similarly to a discontinuity, while the third most northward spike is less extreme and would appear similarly to a local minimum as in the case of Figure 5.26 at the 23:06:36 UT mark. The third most northward spike is also at a point that is the same distance that each of the first two spikes are from the point of closest approach (if for example the second spike is 200 km north of the point of closest approach the third spike is 400 km north the point of closest approach). All three of these spikes are observed in the sub-auroral region, since the 5 flybys were all at calm ionospheric conditions (Kp-index of < 2) and the spikes appear south of the auroral oval (which has a southern boundary at about 60°N).

The ellipticity angle during the 3 spikes is always progressing from a right-hand circularly polarized wave (with respect to the k-vector) to a left-hand circularly polarized wave, then each of the first 2 spikes returns the right-hand circularly polarized wave. This suggests that the observed radio wave gradually becomes more X-mode dominated, then a spike suddenly demonstrates the radio wave becoming O-mode dominated and then the radio wave gradually becomes more X-mode dominated and so on. This potentially could have been caused by an inconsistent spread of transionospheric radio wave raypaths from an HF source, referred to as "HF fades" by James et al. (2006). Figure 5.27 presents the modelled O-mode rays of a 9.303 MHz sub-auroral radar located at Ottawa. The James et al. (2006) paper does not demonstrate the exact same observations as these 3 spikes, but information from this paper shows a similar type of observation. The ionosphere in the model contains traveling ionospheric disturbances, and each dotted line in the figure is a contour line of 10^5 cm^{-3} electron density. Demonstrated in the figure south of the radar there is a region in the ionosphere of ray focusing and a region of ray defocusing. Stated in James et al. (2006), the X-mode equivalent calculation is a similar ray pattern. However, the exact raypath of the X-mode is not shown.

If the 3 spikes in ellipticity angle are examples of observed HF fades corresponding to the focusing and defocusing regions of O- and X-mode rays presented in Figure 5.27, then the RRI data demonstrates that the raypaths from the Saskatoon SuperDARN radar have multiple regions of raypath focusing and defocusing, both north and south of the radar. Since the modelling performed in the James et al. (2006) paper uses a radio wave frequency of 9.303 MHz of a radar that is sub-auroral, it is difficult to exactly compare the number

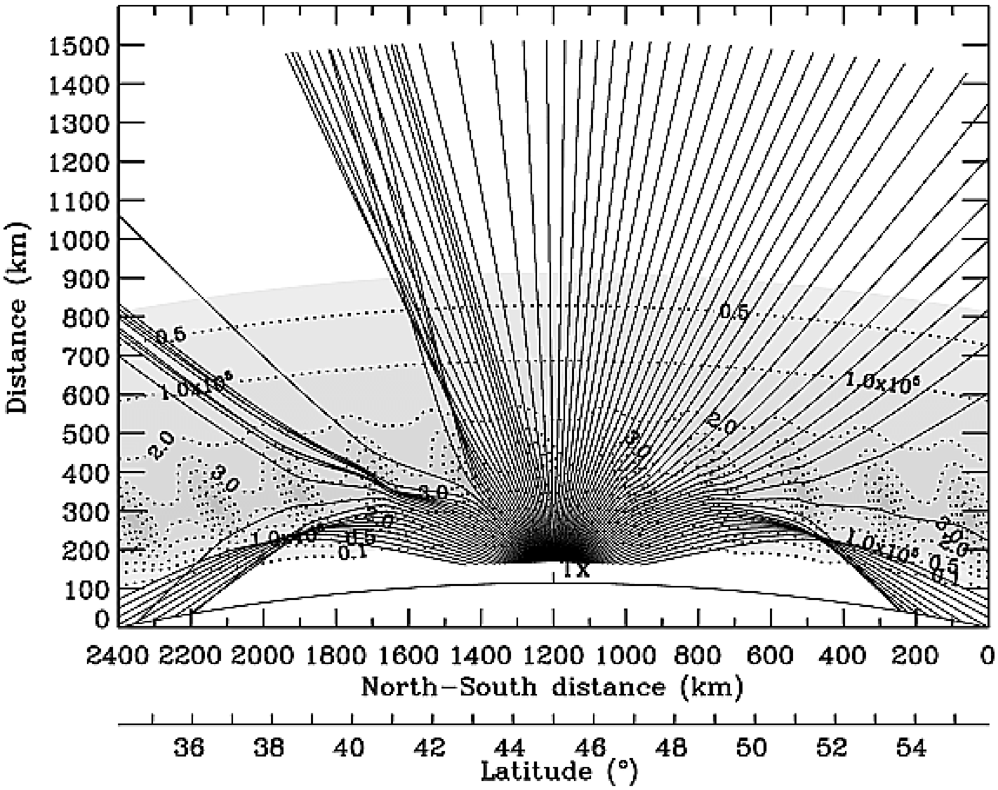

Figure 5.27: Omode rays at 9.303 MHz traced in two dimensions through a model ionosphere with latitudinally periodic density structure. (James et al., 2006)

and location of regions of raypath focusing and defocusing without remodelling the results in auroral conditions with SuperDARN. Additionally, the model ionosphere in Figure 5.27 is only one example of a complicated ionospheric structure and the differences in the structure could lead to drastically different results. The RRI data demonstrates that the O- and X-mode raypaths may be similar, but are not the same (otherwise ray focusing regions of each O- and X-mode rays would coincide) and are instead switching between O-mode focused regions and X-mode focused regions. If the above. From the RRI data, 5 example flybys of this phenomenon may be too few to conclude that this HF fades as described by James et al. (2006). Therefore, more flybys of similar parameters should be planned and the modelling presented in James et al. (2006) should also be repeated but for the Saskatoon SuperDARN radar.

5.6 Summary

This chapter presented all of the phenomena and patterns that was able to be observed in the RRI data from the RRI-SuperDARN Saskatoon conjunction experiments. Presented flybys were exclusively selected from the data set recorded at 14.5 MHz, since the observations from this radar frequency remained the most consistent. Observations from RRI flybys in conjunction with an HF transmitter in Ottawa observations, reported by Danskin et al. (2018) were discussed and compared to Saskatoon flyby observations. The Ottawa flybys presented consistent Faraday rotation reversal events, but the Saskatoon flybys showed much more variability. This chapter also presented the 3 distinct spikes in ellipticity angle observed in slewing, daytime Saskatoon flybys. It was suggested that these 3 spikes were potentially caused by regions of focused and defocused O- and X-mode propagation (or "HF fades"), as suggested by James et al. (2006).

CHAPTER 6

CONCLUSIONS

The goal of my research is to apply polarization techniques to study transionospheric HF radio wave propagation. This was done through characterizing phenomena observed in RRI data in RRI-Saskatoon SuperDARN radar conjunctions. Of the 88 RRI-SuperDARN conjunctions recorded, 49 flybys recorded usable data to interpret transionospheric phenomena (unusable flybys had too low SNR). Transionospheric propagation of the HF radio waves was observed to demonstrate polarization phenomena predicted in the magnetoionic theory. Notably, such phenomena include the Faraday rotation and the Voigt effect. As expected, the Faraday rotation demonstrated a dependence on the physical parameters of both the ionosphere and the geomagnetic field. From the ellipticity angle of Saskatoon flybys, the Voigt effect demonstrated oscillations (which were dependent on the Faraday rotation rate) with a superposition-type behaviour with respect to a varying signature. Both the QL dominant effect, Faraday rotation, and the QT dominant effect, the Voigt effect, were demonstrated to be present throughout a flyby independent of the aspect angle to the geomagnetic field, which was not as clearly demonstrated prior to RRI observations. However, further flybys and modelling would further develop the understanding and categorization of these events.

6.1 Faraday Rotation

As a source of comparison to the RRI-SuperDARN Saskatoon conjunctions, the observations made by Danskin et al. (2018) were discussed. The Danskin et al. (2018) paper presented observations from RRI flybys over an HF transmitter in Ottawa, which showed a consistently occurring Faraday rotation reversal event north of the Ottawa radar (south of the auroral zone). However, the Faraday rotation reversal events as observed in the Saskatoon flybys were not consistent. While also always observed north of the Saskatoon SuperDARN radar, the Faraday rotation reversal events had significantly more variability when RRI was in the Saskatoon SuperDARN radar field of view (which is in the auroral zone when north of Saskatoon). One observation from Danskin et al. (2018) seemed to suggest that a lower foF2 value (less plasma density in the F2 peak) would move the Faraday rotation reversal event north of the expected location. However, the Saskatoon flybys have suggested the opposite case, where flybys with lower foF2 values and nighttime flybys demonstrate Faraday rotation reversal events south of other flybys. However, it should be noted that Faraday rotation reversal events observed with the Saskatoon SuperDARN radar were all located well into the auroral zone, while the reversal events observed with the Ottawa HF transmitter were all sub-auroral.

The Faraday rotation reversal signature demonstrates the dependence of the orientation angle on both the geomagnetic field and ionospheric plasma density. A hypothetical Faraday rotation that is only dependent on the TEC of the the ionosphere would exhibit a reversal at the point of lowest TEC (a little north of the point of closest approach); and since this was not the case in the Saskatoon flybys, the reversal events demonstrated a significant dependence on the geomagnetic field as well. Observed in a Saskatoon flyby on 25 August 2018 was a special case where the trajectory of ePOP passed through the terminator (from darkness into daylight) during the time RRI was observing. The Faraday rotation rate demonstrated a significant slow down since the plasma density would have significantly increased in this transition region, as opposed to the typical slow decrease in plasma density as ePOP travels northward under constant sunlight (or darkness) conditions. The phenomena observed in the orientation angle of the Saskatoon flybys demonstrated good agreement with magnetoionic theory; however, observations of the Faraday rotation reversal signature demonstrated different and more varied effects when compared to the Ottawa flybys reported by Danskin et al. (2018).

6.2 Voigt Effect and Ellipticity Angle Behaviour

The Voigt effect is a physical phenomenon expressed in the ellipticity angle that had been little reported prior to this research. The oscillations in ellipticity angle had been theorized to occur in QT dominated conditions, but the RRI flybys in conjunction with the Saskatoon SuperDARN radar demonstrated that the Voigt effect oscillations occurred even in configurations of the aspect angle that were QL dominated. As predicted by the theory, the Voigt effect oscillation rate was demonstrated to be dependent on the Faraday rotation rate. This is because the O- and X-mode components in QT-like transionospheric propagation are dependent on the orientation angle, which is continually changing due to the always present Faraday rotation.

Unique to these RRI observations were consistent behaviour of 5 daytime, slewing, high-altitude flybys which exhibited 3 distinct spikes or peaks in the regular ellipticity angle oscillations. These spikes in the ellipticity angle data were consistently distributed about the RRI point of closest approach to the Saskatoon SuperDARN radar. These spikes in ellipticity angle have not been reported before and were certainly not demonstrated in the model produced by R. Gillies (Gillies et al., 2012). These spikes demonstrated that as RRI passed by the Saskatoon SuperDARN radar it was moving between alternating regions that were either O-mode dominated (defocusing of X-mode rays) or X-mode dominated (defocusing of O-mode rays). This effect could have been an observation of "HF fades" as described by James et al. (2006), which are regions of focused and defocused O- and X-mode rays caused by an ionosphere with latitudinally periodic density structure. However, an attempt to model the 3 spikes in ellipticity angle should be done in the future in order to prove this conclusion.

6.3 Future Work

As of this writing in June 2019, RRI and ePOP are still operational. In 2018, the ePOP satellite joined in cooperation with the ESA Swarm mission (ESA, 2018), giving increased opportunities for RRI conjunctions with the Saskatoon SuperDARN radar as more RRI data is able to be downloaded. However, in order to more consistently observe transionospheric propagation phenomena demonstrated in this thesis, a more involved flyby planning process will need to be taken. Slewing flybys are ideal, but not always able to be executed due to other payload observational requirements. For flybys that are not slewing (a nadir flyby), the region of the flyby RRI is turn on would have to be centred significantly north of the

Saskatoon SuperDARN radar rather than centred about the point of closest approach. This is because nadir observations at the point of closest approach are unusable for RRI polarization observations. However, the flybys can be used for observations further north to consistently observe the Faraday rotation reversal signature. Similarly, for flybys that are slewing, the flyby would have to be centred on the Saskatoon SuperDARN radar in order to consistently observe phenomena such as the 3 distinct spikes in the ellipticity angle. Additionally, if slewing flybys remain difficult to plan for low-altitude flybys, then a coordination that is not slewing, but oriented such that the RRI normal is pointed towards the Saskatoon SuperDARN radar at the point of closest approach should be attempted.

Finally, supplementary data sets which are used could be improved in the future. The ionosondes used as reference for the local ionosphere were located in the polar cap and significantly more north than most RRI-SuperDARN Saskatoon radar observations. If there was a local Saskatoon (or even anywhere in Saskatchewan) ionosonde that would be operational at the same time as RRI-Saskatoon SuperDARN conjunctions then a greater understanding of the ionosphere could be determined. Additionally, Saskatoon flybys were compared to the modelling software produced by R. Gillies (Gillies et al., 2012), but more rigorous modelling software could be developed. For instance if ray-tracing from a more realistic ionosphere was taken into account during the analysis of RRI data, further detail about observed ray-paths could be demonstrated. The sample ionosphere of the modelling software could also be adjusted in order to simulate certain ionospheric conditions, such as an ionosphere with latitudinally periodic density structure as described in James et al. (2006).

REFERENCES

Bilitza, D. (2012). International Reference Ionosphere. NASA/GSFC, Heliospheric Physics Lab and Space Weather Lab.

Budden, K. G. (1988) The Propagation of Radio Waves: The Theory of Radio Waves of Low Power in the Ionosphere and Magnetosphere. Cambridge University Press.

Canadian Advanced Digital Ionosonde:: CADI. The Canadian High Arctic Ionospheric Network. Retrieved January 2019 from http://chain.physics.unb.ca/chain/pages/cadi/

CSA - Alouette I and II. CSA. Retrieved January 15 2019 from http://www.asc-csa.gc.ca/eng/satellites/alouette.asp.

CSA - ISIS I and II. CSA. Retrieved January 15 2019 from http://www.asc-csa.gc.ca/eng/satellites/isis.asp.

Donald W. Danskin, Glenn C. Hussey, Robert G. Gillies, H. Gordon James, David T. Fairbairn & Andrew W. Yau (2018). Polarization Characteristics Inferred From the Radio Receiver Instrument on the Enhanced Polar Outflow Probe. Space Physics (Vol. 123, No. 2, p. 1648-1662)

ePOP Database. University of Calgary Department of Physics and Astronomy. (2019) https://epop.phys.ucalgary.ca/data/

European Space Agency (ESA). Swarm trio becomes a quartet. Retrieved February 26 2018 from http://www.esa.int/Our_Activities/Observing_the_Earth/Swarm/Swarm_trio_becomes_a_quartet

Gillies, R. G. (2006). Modelling of Transionospheric HF Radio Wave Propagation for the ISIS II and ePOP Satellites, MSC Thesis. University of Saskatchewan, Canada.

Gillies, R. G., Hussey, G. C., James, H. G., Sofko, G. J., & Andr, D. (2007). Modelling and observation of transionospheric propagation results from ISIS II in preparation for ePOP. In Annales Geophysicae (Vol. 25, No. 1, p. 87-97).

Gillies, R. G., Hussey, G. C., Sofko, G. J., Wright, D. M., & Davies, J. A. (2009). Comparison of velocities measured by EISCAT and SuperDARN with consideration of refractive index.

Gillies, R. G., Hussey, G. C., Sofko, G. J., & James, H. G. (2010). Relative O-and X-mode transmitted power from SuperDARN as it relates to the RRI instrument on ePOP. In Annales geophysicae: atmospheres, hydrospheres and space sciences (Vol. 28, No. 3, p. 861).

Gillies, R. G., (2010). Transionospheric Signal Modelling For ePOP and SuperDARN, PHD Dissertation. University of Saskatchewan, Canada.

Gillies, R. G., Hussey, G. C., Sofko, G. J., & James, H. G. (2012). Modeling measurements of ionospheric density structures using the polarization of highfrequency waves detected by the Radio Receiver Instrument on the enhanced Polar Outflow Probe. Journal of Geophysical Research: Space Physics, 117(A4).

Greenwald, R. A., Baker, K. B., Dudeney, J. R., Pinnock, M., Jones, T. B., Thomas, E. C., ... & Hunsucker, R. D. (1995). Darn/Superdarn. Space Science Reviews, 71(1-4), 761-796.

The HDF Group. (2018) Retrieved from https://www.hdfgroup.org/

Hecht, E. and Zajac, A. (1974). Optics. Addison-Wesley Publishing Company.

Kp Index. The Helmholtz-Centre Potsdam - GFZ German Research Centre for Geosciences. (2019) https://www.gfz-potsdam.de/en/kp-index/

The High-Latitude Ionosphere and its Effects on Radio Propagation. Cambridge University Press.

Hussey, G. C. (1994). The Polarization of 50 MHz Auroral Backscatter, PHD Dissertation. University of Saskatchewan, Canada.

James, H. G. (2006). A digital radio receiver for ionospheric research (No. RTO-MP-IST-056). COMMUNICATIONS RESEARCH CENTRE OTTAWA (ONTARIO).

James, H. G., Gillies, R. G., Hussey, G. C., & Prikryl, P. (2006). HF fades caused by multiple wave fronts detected by a dipole antenna in the ionosphere. Radio science, 41(04), 1-13.

Kelley, Michael C.(2009). The Earth's Ionosphere: Plasma Physics & Electrodynamics. Academic Press.

Kivelson, M. G. and Russel, C. T. (1995). Introduction to Space Physics. Cambridge University Press.

CASSIOPE Satellite details 2013-055A NORAD 39265. N2YO. Retrieved January 24, 2019 from https://www.n2yo.com/satellite/?s=39265

Ossakow, S. L., & Chaturvedi, P. K. (1979). Current convective instability in the diffuse aurora. Geophysical Research Letters, 6(4), 332-334.

Qian, L., Burns, A. G., Solomon, S. C., & Wang, W. (2013). Annual/semiannual variation of the ionosphere. Geophysical Research Letters, 40(10), 1928-1933.

Ruohoniemi, J. M., & Baker, K. B. (1998). Largescale imaging of highlatitude convection with Super Dual Auroral Radar Network HF radar observations. Journal of Geophysical Research: Space Physics, 103(A9), 20797-20811.

Stix, T. H. (1992). Waves in Plasma. American Institute of Physics.

Tanenbaum, B. Samuel (1967) Plasma physics. McGraw-Hill.

Conv map overview. Virginia Tech SuperDARN. Retrieved January 2019 from http://vt.superdarn.org/tiki-index.php?page=Conv+map+overview

Wayne, R. P. (2000). Chemistry of Atmospheres. Oxford University Press.

Yamamoto, Manabu and Murayama, Seiichi (1979). Analysis of resonant Voigt effect. J. Opt. Soc. Am. (Vol. 69, No. 5, p. 781-786)

Yau, A. W., James, H. G., & Liu, W. (2006). The Canadian enhanced polar outflow probe (e-POP) mission in ILWS. Advances in Space Research, 38(8), 1870-1877.

Zvezdin, A. K. and Kotov, V. A. (1997). Modern Magnetooptics and Magnetooptical Materials. Taylor & Francis Group, LLC.